Theoretical and experimental studies of molecular motions and reaction mechanisms

Greaves, Stuart Jeffrey

Theoretical and Experimental Studies of Molecular Motions and Reaction Mechanisms

I. Mechanisms in the Hydrogen Exchange Reaction

II. UV Cavity Ring-Down Spectroscopy of 1, 4-bis(phenylethynyl)benzene

Stuart Jeffrey Greaves

Department of Chemistry

University of Durham

A thesis submitted in partial fulfilment

of the requirements for the degree of *Doctor of Philosophy*

2005

Declaration

The material contained within this thesis has not previously been submitted for a degree at the University of Durham or any other university. The research reported within this thesis has been conducted by the author unless indicated otherwise.

Copyright Notice

Acknowledgements

The production of this thesis would not have been possible without the assistance of a large number of people who deserve a great deal of thanks:

My supervisor, E. Wrede for his patience, support, answering of stupid questions, many helpful discussions, and for allowing me to do this PhD.

For the work on the hydrogen exchange reaction I would like to thank D. Murdock for his extremely useful "Potential KEnergy" trajectory visualisation program and fruitful discussions, as well as for thinking of good names for the new reaction mechanisms; S. C. Althorpe (Durham, Exeter, now at Nottingham University) for the use of his quantum snapshots and for helpful discussions.

For the work on the CRDS of BPEB I would like to thank M. N. R. Ashfold, A. J. Orr-Ewing, C. M. Western and the Laser Chemistry, Spectroscopy and Dynamics Group at the University of Bristol for allowing me to visit their laboratory, for lending much needed vacuum equipment, UV cavity-mirrors, and access to the WI2 simulation program, and many helpful discussions about cavity ring-down spectroscopy.

The girls: N. Elliot, V. Whittle, E. Flynn and E. Futcher for their assistance with the CRDS experiment at its various stages of development; and the mechanical and electrical workshops of the Chemistry Department in Durham.

P. Low for suggesting BPEB; A. Beeby for helpful discussions on molecular wires and for the use of lasers at the initial stages of the experiment; S. R. Rutter and D. P. Lydon for BPEB synthesis, particularly D. P. Lydon for the D-BPEB synthesis; K. Findlay for spectra of BPEB in cyclohexane; and J. Simons and L. Snoek (Oxford University) for the oven design.

St. Aidan's College, SCR and boat club, members past and present; Matt and Clare and the rest of Durham's class of 2001.

I would also like to acknowledge the support and patience of my family, without whom none of this would have been possible.

Abstract

Mechanisms in the Hydrogen Exchange Reaction

The time-delayed forwards scattering mechanism recently observed by Althorpe *et al.* [1] for the H + $D_2(v{=}0,\ j{=}0) \rightarrow HD(v'{=}3,\ j'{=}0)$ + D reaction was analysed using the quasi-classical trajectory (QCT) methodology. QCT's were found to reasonably match the quantum snapshots of Althorpe, without the quantum effects. Trajectories were analysed on the fly to investigate the motions of the atoms during the reaction. The dominant reaction mechanism progresses from hard collinear impacts, leading to direct recoil, to glancing impacts. The increased time required for forward scattered trajectories is due to the rotation of the HDD complex. Forwards scattered trajectories display symmetric stretch vibrations of the HDD complex, indicating the presence of a resonance or a quantum bottleneck state.

Reactive scattering in the $HD(v'{=}0,\ j'{=}0)$ product channel was found to be governed by two unexpected and dominant new mechanisms, and not by direct recoil as is generally assumed. The new mechanisms involve strong interaction with the conical intersection, an area of the potential energy surface not previously thought to have much effect upon reactive scattering. Initial investigations indicate up to 56% of reactive scattering could be the result of these mechanisms.

UV Cavity Ring-Down Spectroscopy of 1, 4-bis(phenylethynyl)benzene

The torsional motion of 1, 4-bis(phenylethynyl)benzene (BPEB), a prototype molecular wire, is important for switching in molecular electronics. Cavity ring-down spectroscopy was used to record the torsional spectra of BPEB and 1, 4-bis(phenylethynyl) 2,3,5,6-tetradeuterobenzene in the gas phase. The spectra were modelled using a simple cosine potential. The experimental torsional barrier is very similar to the two ring system, Tolane. It was found that DFT calculations completely overestimate the torsional barrier.

Contents

List of Figures

List of Tables

Chapter 1

Introduction

The initial work on the hydrogen exchange reaction was motivated by the observation of a time-delayed mechanism in the hydrogen exchange reaction by Althorpe *et al.* [1]. With expertise in experimental and quasi-classical trajectory studies of this simplest of chemical reactions within the research group, it was decided to investigate the mechanism behind the time-delayed scattering in the $v' = 3$ product.

The techniques developed for the investigation of the $v' = 3$ products were then applied to other product quantum states, with surprising results. This theoretical study of reaction mechanisms occupied the first 15 months of the research project, and is presented in Part I of this thesis.

Part II of this thesis covers a cavity ring-down spectroscopy (CRDS) experiment to study weak absorptions of cold molecules in molecular beams. This experiment was initially set-up in the laboratory of Dr Beeby, as our group did not have its own laser system at this time.

A grant for the 'experimental study of the reaction of Rydberg atoms' (A* + BC $\rightarrow$ AB + C*) was awarded to the group during the work on CRDS. The experimental equipment for this project consists of a crossed molecular beams apparatus, with an ion imaging detection system. Central to the experiment is the laser system comprising of two Nd:YAG lasers and three dye lasers.

Design work for the Rydberg experiment, including the design of an ion optics detection system, was carried out during the course of the second year of research, after the work on the CRDS experiment was interrupted by a departmental refurbishment. It was intended that testing and calibration of this experiment would

occupy the third year of research.

After several delays, including the departmental refurbishment and construction work in the laser lab, it was realised there would be insufficient time to work on the Rydberg experiment. The laser system for the Rydberg experiment was in place by this time and it was decided that continuing work on the cavity ring-down spectroscopy (CRDS) experiment could yield interesting experimental results, as well as testing the new facilities.

The new set-up, design, and characterisation (by studying the jet cooled spectra of iodine) of the CRDS experiment is described in Part II of this thesis.

At this time the possibility of using molecules as switches and wires was a subject of much scientific interest within the field of molecular electronics, and in this department. The molecules in question were Poly(phenyleneethynylene)s, highly conjugated systems, the conductance of which is thought to be dependent upon the relative twist angles of the phenyl rings. The motion of these rings was being extensively studied by theoretical methods and solution state experiments, but high resolution gas phase studies had not been carried out.

The CRDS set-up was adapted to study the twisting motion of the ground and first excited state of the prototypical molecular wire 1, 4-bis(phenylethynyl)benzene (BPEB) in the UV region. Electronic structure calculations were also used to aid the simulation of the BPEB spectrum to help discern the twisting motion of the rings.

Part I

Mechanisms in the Hydrogen Exchange Reaction

Chapter 2

A Brief History of the Hydrogen Exchange Reaction

2.1 Introduction

$$\text{D-D} \quad \leftarrow \text{H} \qquad \Rightarrow \qquad \leftarrow \text{D–D} \leftarrow \text{H} \qquad \Rightarrow \qquad \leftarrow \text{D} \quad \text{D-H}\rightarrow$$

The hydrogen exchange reaction, the simplest chemical reaction, has been *the* prototype for bimolecular reactions since 1929, when London [2] showed that it could be understood in terms of a potential energy surface (PES) calculated from quantum mechanics.

This section will review both important experimental and theoretical methods of studying the hydrogen exchange reaction.

The presence in hydrogen of only one electron per atom allows the most exact calculations for a reactive system. The H_3 PES is the most accurately known because of this simplicity. It is the H_3 PES that makes the hydrogen exchange reaction so amenable to theoretical study. The system is simplified further because the hydrogen atoms are very light, therefore the resulting reactants and products have low moments of inertia and high vibrational frequencies, therefore few rotational and vibrational quantum states are involved.

The lack of a dipole moment, and the electronic absorption of the hydrogen atoms and molecules being in the vacuum ultraviolet region, presented experimentalists with considerable difficulties. Because of these constraints no *simple* method was

available for state-specific preparation and detection of reactants and products until the development of laser techniques, which allowed a rapid increase in experimental accuracy and resolution.

A number of comprehensive reviews are available on this topic [3, 4, 5, 6, 7], thus this section of the report will only give a brief history of the study of the hydrogen exchange reaction, covering experimental and theoretical methods, with an emphasis on recent experimental and theoretical developments. The controversial topic of resonance will also be briefly discussed.

2.2 Experimental

The ultimate aim of any experiment probing the reaction dynamics of a system is to measure the cross section and angular distribution of the products for a completely specified collision [8]. In practice the aim is for the most detailed observations possible, *i.e.* the rovibrational state-to-state differential cross section (DCS) at a well defined collision energy. The requirements of such an experiment include [6]:

- Single collision conditions within the scattering volume.
- Monochromatic energy distributions of the reactants.
- (v, j) state specific preparation of the reactants.
- Distinction of reactive products from the reactants.
- (v', j') state selective detection of the products.
- Detection of the product angular distribution.

2.2.1 Early Experiments

The first successfully fulfilled condition was the distinction of reactive products from the reactants, when Hund [9] pointed out in 1927 that on the basis of quantum mechanics, the rotational states of H_2 can be divided into two groups (*ortho*-H_2 and *para*-H_2) corresponding to the spin states of the nuclei. The conversion of p-H_2 to

o-H_2 is catalysed by hydrogen atoms and its presence indicates that an exchange reaction has taken place.

Bonhoeffer and Harteek [10] showed that labelling of H_2 in this way can be achieved by absorbing hydrogen on charcoal at liquid hydrogen temperatures. Farkas and Farkas [11] showed that isotopic substitution is another useful tool for product distinction when studying the kinetics of the hydrogen exchange reaction. These early experiments could only measure the thermal rate coefficients by using thermal conversion [12] or flow tube techniques [13].

2.2.2 Bulk Experiments

Bulk experiments are so called because they are carried out in a cell of the bulk reagents.

An early approach used to overcome the reaction barrier in bulk experiments of the D + H_2 reaction was to use stimulated Raman pumping to populate $H_2(v = 1, j = 1)$ selectively in the electronic ground state of molecular hydrogen [14]. The products of the D + $H_2(v = 1) \rightarrow HD(v' = 0, 1)$ + H reaction were monitored by the Coherent Anti-Stokes Raman Spectroscopy (CARS) method [15]. Early experiments measured rate constants for the reaction that were in close agreement with theoretical predictions [16].

An alternative way to overcome the reaction barrier is to use the kinetic energy (KE) of fast moving D atoms. To obtain better control of the translational energy of the D atoms Kupperman and White [17] used DI and DBr photolysis to produce a monochromatic energy distribution of reactants. Using this method they reported the first measurements of the energy threshold for the D + $H_2 \rightarrow$ HD + H reaction.

Direct information on the microscopic dynamics of the hydrogen exchange reaction under single collision conditions can be obtained by combining translationally hot hydrogen atom formation by laser photolysis with time- and state- resolved product detection by pulsed laser spectroscopy.

2.2.3 Molecular Beam Studies

Molecular beam studies, in which the reactants for the reaction are mixed in a reservoir and then expanded through a nozzle, are an improvement on the bulk methods mentioned above.

Detection of molecular product states in hydrogen molecules and their isotopic variants can be achieved by CARS or Resonance Enhanced Multi Photon Ionization (REMPI). Experiments of this type have been carried out by Zare *et al.* [18] and Valentini *et al.* [19]. HI and D_2 are premixed and introduced into a vacuum chamber via a capillary nozzle. The reaction is initiated downstream of the nozzle by laser photolysis of HI. After a delay the HD product is state selectively analysed by (2+1) REMPI spectroscopy. The HD^+ ions produced are mass-selectively detected in a shuttered time-of-flight mass spectrometer. These experiments give a complete rovibrational state distribution of the reaction product.

PHOTOLOC

The PHOTO initiated reaction analysed via the Law Of Cosines (PHOTOLOC) technique was developed by Zare *et al.* [20, 21] to measure the full angular distribution for a single product quantum state. This method is a further refinement of the molecular beam methods mentioned above. The name is derived from the two major elements of the technique: 1) laser photolysis initiates the chemical reaction in a mixture of a photolytic precursor and reagent. 2) the law of cosines relates the product laboratory velocity distribution to the centre-of-mass product angular distribution.

A single molecular beam containing the D_2 and HBr reactants is co-expanded into a vacuum which leads to a relative speed, of D_2 and HBr, of practically zero. A polarized laser beam photolyses the HBr precursor, generating H fragments with well defined speed and spatial anisotropy which subsequently collide with the D_2 reagent to generate HD and D products. (2+1) REMPI and a time-of-flight (TOF) mass spectrometer is used to measure the velocity distribution of the HD product from the reaction along the time-of-flight axis. The REMPI scheme ensures that only one rovibrational state of HD is ionised, and, as the whole scattering angular

range can be analysed, this allows the production of state specific DCSs.

Since its inception photoloc has been used frequently to record differential cross sections for the D + H_2 reaction, at a range of energies from 1.3 to 1.89 eV [1, 21, 22, 23, 24]. The angular resolution of the experiment is dependent upon the collision energy (low energy has lower resolution) and scattering angle, forward scattering has a resolution of $\pm 20°$ [24]. This experiment has recently been modified to measure integral cross sections of the HD(v'=2-3, j') products [24, 25, 26]. The results from these experiments are compared with time-dependent and time-independent quantum scattering calculations, see Section 2.3.3.

2.2.4 Crossed Molecular Beams

The Crossed Molecular Beams (CMB) technique was first widely applied to the reactions of alkali metals, but in the late 1960's the development of universal machines which used mass spectrometry made possible the study of the hydrogen exchange reaction using isotopic variants. CMB experiments can yield rotationally averaged cross sections and differential cross sections if the resolution of the experiment is high enough.

The early experiments were hindered by the lack of monoenergetic sources of reactants. The first experiment to yield a total DCS was conducted in 1972 by Geddes, Krause and Fite [27] at an average energy of 0.48 eV on the D + H_2 system. The D atoms were generated from D_2 in a thermal dissociation source which caused a broad Maxwell-Boltzmann velocity distribution. The HD products were detected using mass spectrometry and found to be backwards scattered in the centre-of-mass system with respect to the incoming D atom.

In 1986 Götting, Mayne and Toennies [28] conducted CMB experiments to provide the first velocity and angular resolved detection of the HD products. The angular and velocity distributions were measured at 1 eV and 1.5 eV using a rotatable time-of-flight (TOF) mass spectrometer. Again the resolution of the results was limited by the broad velocity distribution of the D atoms which were formed in an arc discharge source at about 25,000 K.

In 1987 Buntin *et al.* [29] used the previously mentioned laser photolysis tech-

nique on a D_2S precursor to improve the velocity distribution of the D atoms. This provided the first vibrational state resolved DCS for D + H_2.

This resolution of product states was improved upon by Schnieder *et al.* [30, 31, 32, 33] who in an elegant series of experiments have presented fully rovibrational state resolved DCSs for the H + $D_2(v = 0, j = 0)$ system at a range of collision energies. The HD product quantum state distribution is obtained from the D atom kinetic energy spectra (KES) using H-atom Rydberg TOF spectroscopy [34].

In the experiment a pulsed molecular beam of *ortho*-D_2, adiabatically cooled to the ground rotational state ($j = 0$) in a supersonic expansion from a liquid N_2 cooled reservoir, was crossed with kinematically hot H-atoms, generated by photolysis of HI in a second molecular beam. After reaction the velocity distribution of the nascent D-atoms was measured using the technique of Rydberg atom TOF. This technique is based on the resonant excitation of nascent D-atoms to metastable Rydberg states directly inside the scattering volume. After excitation the D atoms continue to drift at their post collision velocity. They are detected at the end of the drift region by field ionization and subsequent acceleration of the resulting ions onto a suitable particle multiplier. This detector can be rotated around the scattering centre, and can therefore be used to build up an angular dependent product distribution.

An unprecedented energy resolution, $\Delta E/E$, of 0.35% was obtained, good enough to resolve the rovibrational distribution of the products. This coupled, with the reproducibility of the experiments, allowed comparison with quantum mechanical calculations, and even allowed assessment of the accuracy of the different available PESs [35].

More recently Yang *et al.* have used the same experimental methodology to study both the H + $D_2(v = 0, j = 0)$ and H + HD$(v = 0, j = 0)$ reactions [36, 37, 38]. Using a specific LAB detection angle, corresponding to backwards scattering, the HD$(v = 0, j = 2)$ product cross section was measured at nineteen energies between 0.4 and 1 eV. In comparison with quantum scattering theory it was concluded that the oscillations in cross section were due to quantum bottleneck states opening up at different collision energies [38, 39].

2.3 Theoretical

To understand/interpret the mechanisms behind the hydrogen exchange reaction the experimental results are compared with theoretical calculations. The detailed results available from these calculations are convoluted to match the measurables of the experiment, such as state-to-state differential cross sections or rate coefficients. Theoretical determination of these measurables can be divided into three steps which will be discussed in detail below:

1. Construction of the global H_3 surface;
2. Description of the microscopic dynamics of the three atoms on the hypersurface by classical or quantum mechanics;
3. Evaluation of macroscopic quantities.

2.3.1 H_3 Potential Energy Surface

As the study of this exchange reaction involves the motion of both the electrons and nuclei, the Born-Oppenheimer approximation is used to decouple the electronic and nuclear motions. A useful consequence of the Born-Oppenheimer approximation is that isotopic substitution does not change the PES. *i.e.* $H_3 \equiv D_3 \equiv HD_2 \equiv H_2D$.

The potential energy of H_3 is a function of the relative positions of the nuclei. The forces acting upon the hydrogen/deuterium nuclei during the hydrogen exchange reaction are derived from the derivatives of the potential energy surface.

Main Features of the H_3 PES

The H_3 (A+BC) potential energy surface has a minimum energy path (see dashed line in Fig. 2.1) at linear geometry with a barrier of 9.607 kcal/mol (0.4166 eV) [40]. There is a van-der-Waals well between 2 and 4 Å from the linear saddle point. A local maximum occurs at equilateral triangular geometry due to a conical intersection (CI) between the ground and excited state, see Fig. 2.2.

At small internuclear BC separation, q, the CI moves into the region of high repulsive potential surrounding the BC and is therefore less prominent. At large

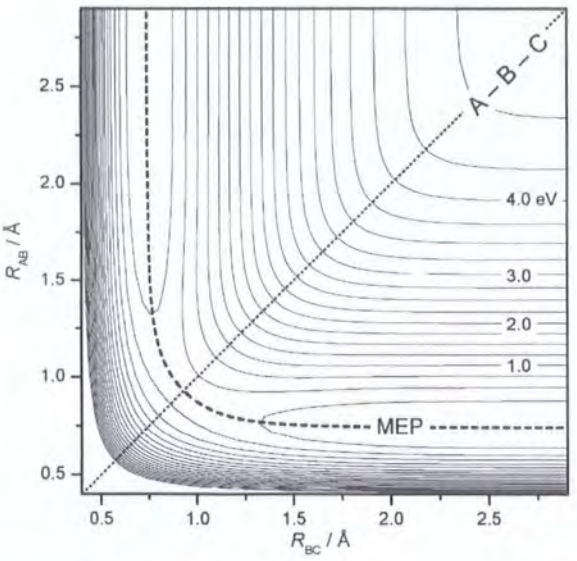

Figure 2.1: The collinear H_3 PES, showing the product and reactant channels. The minimum energy path (MEP) is shown as a dashed line, and the barrier is shown as a dotted line.

q the CI becomes a more prominent feature on the PES, as it is no longer in the region of high potential surrounding the BC.

History of the H_3 PES

In 1929 London [2] proposed that only one PES was required to study a chemical reaction, and that the H_3 surface could be regarded as the superposition of the potentials of three H_2 molecules. The potential energy of H_3 was expressed simply in terms of the three Coulombic interaction integrals, Q_i, and the three exchange or valence integrals, $\mathcal{A}$, $\mathcal{B}$ and $\mathcal{C}$:

$$E = Q_1 + Q_2 + Q_3 \pm \left\{ \frac{1}{2}[(\mathcal{A} - \mathcal{B})^2 + (\mathcal{B} - \mathcal{C})^2 + (\mathcal{A} - \mathcal{C})^2] \right\}^{1/2} \qquad (2.1)$$

Early *ab initio* results were considered unsatisfactory and led to the development of semiempirical surfaces which culminated in the PK surface of Porter and Karplus in 1964 [41].

The improvement in computer technology in the latter part of the century meant that *ab initio* methods became more accurate until in 1973 Liu [42] produced a collinear *ab initio* surface that was to become the 'father' of almost all of the modern chemically accurate potential energy surfaces. Calculations were confined to

collinear geometries where high symmetry made the computations affordable, 137 molecular configurations were studied.

Surface	Year	Number of *ab initio* points	Number of fitting parameters	*rms error* [kcal/mol]
LSTH	1978	267	23	0.17
DMBE	1987	316	38	0.24
BKMP	1991	772	129	0.16
BKMP2	1996	8701	129	0.17
CCI	2002	4067	n/a	6.46×10^{-3}

Table 2.1: Comparison of potential energy surfaces, including the root mean square (***rms***) error of the fit.

Five years later Siegbahn and Liu [43] used a smaller basis set to calculate energies at 156 non-linear configurations. Truhlar and Horowitz [44] used an analytical function to fit 267 *ab initio* points, 135 from Liu's collinear study and 132 non-linear configurations from Siegbahn and Liu, with additional points added to constrain the fit at the saddle point and van-der-Waals region. This is known as the LSTH surface, after Liu, Siegbahn, Truhlar and Horowitz, and was the first H_3 surface to provide a chemical accuracy of 0.2-0.5 kcal/mol for a reactive system.

In 1987 Verandas *et al.* [45] used 316 *ab initio* points at 310 unique configurations, including all the points from the LSTH surface, with additional points for better coverage near the conical intersection. The DMBE surface, see Fig. 2.2, was so called because it was based on a Double-Many-Body-Expansion which was designed to be valid for the van-der-Waals region as well as the high energy conical intersection and the upper sheet of the potential.

1991 brought the Boothroyd, Keogh, Martin and Peterson (BKMP) PES [46] which was fitted to 772 *ab initio* points, including the points used in the DMBE surface. All the points were adjusted to account for basis set incompleteness. An additional 119 points were used to constrain the fit in the van-der-Waals region. In 1996 the same functional form as BKMP, was used to fit 8701 *ab initio* energies, including those used in the LSTH and BKMP surfaces, for the BKMP2 surface [47]. Until recently the BKMP2 was thought to be the most accurate H_3 PES, in part

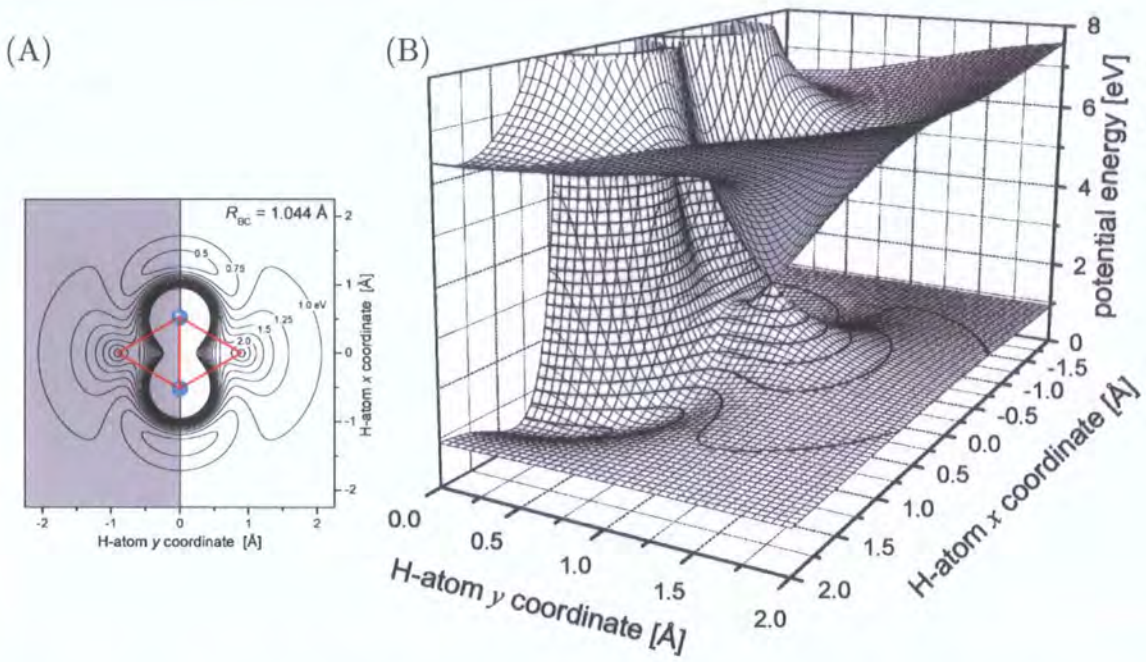

Figure 2.2: The A+BC potential energy surface for hydrogen and its isotopomers. (A): A contour plot of a cut through the plane containing the molecular axis (BC) of the ground state potential, the lower sheet of (B). The BC atoms (blue circles) lie along the x-axis, the potential is shown as a function of the (x,y) position of the A atom relative to the centre of mass of BC (0,0). (B): A 3D representation of the ground and excited (DMBE) potentials of A+BC, only the white side of (A) is shown. The ground and excited state are degenerate at D_{3h} geometry (red equilateral triangle in (A)) forming a conical intersection which is clearly visible in (B).

due to the sheer number of points and the quality of the fit.

A more systematic approach to constructing the H_3 PES has been used by Mielke *et al.* [40, 48] to create a family of analytic Born-Oppenheimer PES's. Energies were calculated at 4067 unique H_3 configurations using three increasingly complex basis sets. Using a basis set extrapolation scheme the complete basis set limit energy was also calculated for each configuration. A new functional form was used to create a PES for each of the basis sets used, including the complete basis set. As the calculations for each of the surfaces used the same basis set, the need to create a special scheme to adjust the disparate data sets so that they could be used together was avoided. The PES created using the complete basis set is called the complete configuration interaction (CCI) PES. The CCI surface is in close agreement with the BKMP2 surface, but shows differences in the van-der-Waals well depth and the height of the conical intersection.

Experimental Comparison

The ultimate accuracy test for a PES should come from a direct comparison with experiment.

> "...reaction dynamics calculations are only as good as the potential energy surface on which they are carried out and any error in the surface will cause errors in the theoretical results" [19].

Prior to the development of the CCI surface an experimental comparison was carried out by Bañares *et al.* [35] for the $H+D_2(v = 0, j = 0) \rightarrow HD(v' = 0, j')$ + D system at 0.52, 0.53 and 0.54 eV. Quantum mechanical calculations on the LSTH, DMBE and BKMP(2) potential energy surfaces were compared with the experimental results of Schnieder and co-workers.

> "... it can be unequivocally concluded that the two versions of the BKMP surface provide the best description of the scattering process for this system at this [collision energy]".

The comparison of experimental and theoretical results revealed distinct differences between the results obtained on the various surfaces. It was concluded that the BKMP2 surface is the best surface to describe the reactive scattering process over the range of collision energies investigated.

The differences between the LSTH and BKMP2 can be attributed to the difference in collinear barrier heights. The stronger orienting character of the DMBE PES with respect to the other PES's explains the deviations of the DMBE relative to the experimental results.

The excellent agreement between experiment and quantum mechanical calculations on BKMP2 was at odds with the situation for thermal rate constants, where quantum mechanical calculations on LSTH and DMBE gave better agreement with experiment at the time. This problem was recently addressed using the new CCI PES which has been used to calculate the $H+H_2$ thermal rate constant, where it matches experimental results 'perfectly', within experimental error [49, 50]. This new surface has not, to our knowledge, been used to evaluate results from scattering experiments.

An important conclusion from the experimental/theoretical comparison was that the topology of the PES had a major effect on processes sensitive to the detailed nature of the surface including scattering resonances and low temperature rate constants [35].

2.3.2 Quasi-Classical Dynamics

An early method used to describe the dynamics of the three atoms on the PES was quasi-classical trajectory (QCT) theory. QCT theory is more simple and computationally cheaper than quantum mechanical (QM) methods but is unable to take into account quantum effects such as tunnelling. The QCT methodology describes the reaction using classical mechanics to govern the motion of a 'ball' passing through the hills and valleys of the PES.

Classical trajectory studies of reaction dynamics began with an unfinished trajectory calculated by Hirshfelder, Eyring and Topley [51]. Further use of the trajectory method had to wait until Wall, Hiller and Mazur [52] applied computers to the problem. Later Karplus, Porter and Sharma [53] made the first trajectory calculations in which the initial collision variables were properly sampled, so reaction cross sections and rate coefficients could be calculated.

In the quasi-classical method the molecules are prepared in discrete internal energy states corresponding to the quantum states of the molecule. Having selected the rovibrational state and the initial collision energy other collision variables are randomly selected from the relevant classical distribution functions. Once the trajectory is begun, this quantum restriction is relaxed so that the time evolution of the system is governed solely by classical mechanics. A similar quantisation is employed in the analysis of the product molecule internal energy states, whereby the continuous range of quasi-quantum numbers is rounded to the nearest integer.

Once a statistically significant number of trajectories has been calculated using pseudo random collision parameters, quantities such as the opacity function (probability of reaction as a function of impact parameter) and various state-to-state cross sections can be calculated for comparison to experimental results.

QCT Results

The QCT method has been used for a wide number of studies of the hydrogen exchange reaction, and has shown good agreement, at least qualitatively, with experimental and quantum mechanical cross sections [32, 54, 55]. An often exploited advantage of QCT is its ability to investigate the individual mechanisms of trajectories. This has been used to investigate short lived collision complexes, in terms of time delay, that may cause resonances [56, 57, 58] and for general investigation of the hydrogen exchange reaction [59, 60].

2.3.3 Quantum Mechanical Scattering Theory

Rigorous Quantum Mechanical (QM) scattering theory provides the most complete description of collision dynamics for a given PES.

Early three dimensional QM scattering calculations were carried out using the Coupled Channel (CC) method which involves solving the Schrödinger equation exactly by expanding the wavefunction in a basis set, propagating the resulting coupled equations in different arrangement channels on appropriate matching surfaces and applying scattering boundary conditions [6].

Currently there are two major methods used for QM reactive scattering calculations, time dependent and time independent, both will be covered briefly here.

Calculations for both methods are simplified by the use of conservation of total angular momentum: calculations are run for each separate value of total angular momentum, J, producing a scattering matrix, S , for each partial wave (*i.e.* J and K value). The S-matrix is the primary result of QM calculation. The square of the elements of the S-matrix gives the reaction probability for a particular $(v, j) \rightarrow (v', j')$ reaction. For the calculation of a scattering cross section the S-matrix is required for all values of J that contribute significantly to the partial wave sum. For the H + D_2 reaction for total collision energy of 2.2 eV partial waves of $J = 41$ are required for convergence of the cross section [32]. Computational cost scales linearly with J, so, QM calculations can be very expensive [61].

Both time dependent and time independent methods suffer from the so called 'coordinate problem'. Jacobi coordinates (q, Q, γ), see Figure 2.3, are the natural

choice for describing the reactants and products because they are easily physically interpreted. Jacobi coordinates for describing the reactants, A + BC, are not appropriate for describing the products, AB + C.

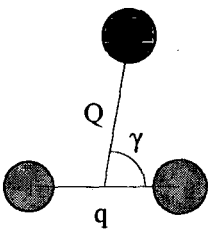

Figure 2.3: The Jacobi coordinate system, where q is the internuclear separation of the diatomic, Q is the distance from the diatomic centre-of-mass to the atom, and γ is the angle between q and Q.

Time Independent Quantum Mechanical Scattering

Time independent QM calculations are carried out at fixed energies and the S-matrix contains elements between all reactant and all product states, allowing any reactant state to product state reaction cross section to be assessed.

Because of the computational cost of time independent QM [61], fully converged state-to-state reaction cross sections have only become possible with the use of super computers in the last 10 years.

When using time independent QM, the coordinate problem is avoided by using hyperspherical coordinates during the calculation, as they provide a good representation of the triatomic at the transition state. Hyperspherical coordinates are also valid in the reactant and product channels [7], but are converted from and to Jacobi coordinates at the start and end of the calculation to set-up and probe the reactant and product states.

These calculations only provide information about the initial and final states, for practical reasons no wave functions are produced or stored. No time related information is available so reaction mechanisms can not be discerned.

Time Dependent Quantum Mechanical Scattering

Time dependent QM calculations are carried out for a single reactant (v, j) state and provide information about the scattering into all (v', j') product states over a wide

range of energies. Time dependent QM calculations also provide a time evolving picture of the reaction which often helps to interpret the reaction dynamics.

Recently, Althorpe has developed a time dependent QM method based on quantum wavepackets [62, 63], where the wavepacket can be followed into the product region. Because it has not been possible to implement the wavepacket methodology efficiently using hyperspherical coordinates the 'coordinate problem' still exists for time dependent wavepacket calculations. It is therefore necessary to switch between different reagent (r) coordinates (A + BC) and product (p) coordinates (AC + B). The switching must take place in the 'strong interaction region' where A,B and C are all close together and represented equally well by r and p coordinates.

Previously, this would have been achieved by stopping the calculation midway, when the wavepacket had reached the strong interaction region, and then transforming the wavepacket from r to p coordinates. This transformation is expensive and unreliable due to the spreading of the wave packet in the strong interaction region.

This coordinate problem is avoided by splitting the (exact) Schrödinger equation for the reaction into reactant and product regions, using the 'reactant-product decoupling' (RPD) equations introduced by Zhang *et al.* [64].

The complete wavefunction produced by the calculation can then be projected onto the desired rovibrational product state of HD giving a product wavefunction which describes when and where the product is formed and how it scatters. The square of the product wavefunction gives a probability density which can be followed over time showing when and where the products form [1, 65]. This gives an insight into the reaction dynamics of the whole system.

Quantum Mechanical Resonances

Resonances are one of the most intriguing and sought after QM effects in reaction dynamics. Resonances in the scattering cross section are caused by H_3 complexes that exist in wells on the potential surface [19, 54, 66, 67]. These wells have discrete energy levels, which correspond to the eigenenergies of the quasi-bound complex [5]. When a collision energy activates one of these levels a long lived complex is formed which leads to an enhanced level of reactive scattering. Thus peaks in energy dependent cross sections are said to be indications of scattering resonances,

these peaks can be broad due to short lifetimes of the complex. Identification of a resonance is considered to be 'spectroscopy of the transition state' [18]. A resonance has been observed in the F + HD → HF + D reaction demonstrating that resonances can cause state-specific forward scattering of product molecules [68].

Many claims of resonances in the hydrogen exchange reaction have been made, but many have also been disproved [5, 7, 18, 19, 54, 57, 61, 67, 69, 70, 71]. Forward scattering has been observed in the H + D_2 → HD + D and attributed to a time delayed mechanism [1], but some authors attribute the forward scattering to the effect of a quantised bottleneck state (QBS) [36].

QBSs are rotational-vibrational quantum states of the collision complex lying near the maxima of effective potential barriers, they can be labelled by the quantum numbers for motion orthogonal to the reaction coordinate [38]. When a transition complex meets the energy of a QBS a new channel to the products is opened, so reaction probability should show a stepwise relationship to collision energy [38, 39]. QBSs also cause time delays in the reaction due to the slow-down of the motion of the complex near the reaction barrier [36, 38, 66].

It is interesting to note that both resonances and QBS agree on the type of motion required for either process: symmetric stretches and bending motions of the H_3 complex [19, 36, 67].

Chapter 3

Recent Developments

Recent experiments have been able to investigate the hydrogen exchange reaction in unprecedented detail [24, 32, 38], and along with quantum mechanical calculations [72] the solution to this 75 year old problem may be in sight. There are still many aspects of the reaction that are the topic of much discussion in the literature, not least the controversial topic of resonances [54] or quantum bottleneck states [36] (see Section 2.3.3).

Much of the controversy is focused on the mechanism(s) required for time delayed forward scattering; Some believe that it is due to resonance states of the H_3 complex [19, 67, 54], whilst others believe that quantum bottleneck states are responsible [36, 38].

A recent experiment, in combination with theoretical calculations, observed a time-delayed scattering region and concluded it was formed by a mechanism other than the dominant recoil mechanism [1]. The recoil mechanism involves a head-on collision with a linear transition state, the bonds break and form concertedly and the products scatter in the backwards direction.

3.1 Time-Delayed Mechanism in the Hydrogen Exchange Reaction

The time delay found by Althorpe *et al.* [1] using time-dependent plane wave packet methods [72, 63], claimed that the HD($v' = 3$, $j' = 0$) product was formed by two

distinct reaction mechanisms, separated by a time delay of 25 fs. The latter one being an indirect forwards scattering mechanism possibly due to scattering resonances associated with a quasibound collision complex. The temporal and spatial separation of the mechanisms was demonstrated using the snapshots (see Fig. 3.1) from Althorpe's quantum wavepacket simulation of the H + $D_2(v = 0, j = 0) \rightarrow$ $HD(v' = 3, j' = 0)$ + D reaction.

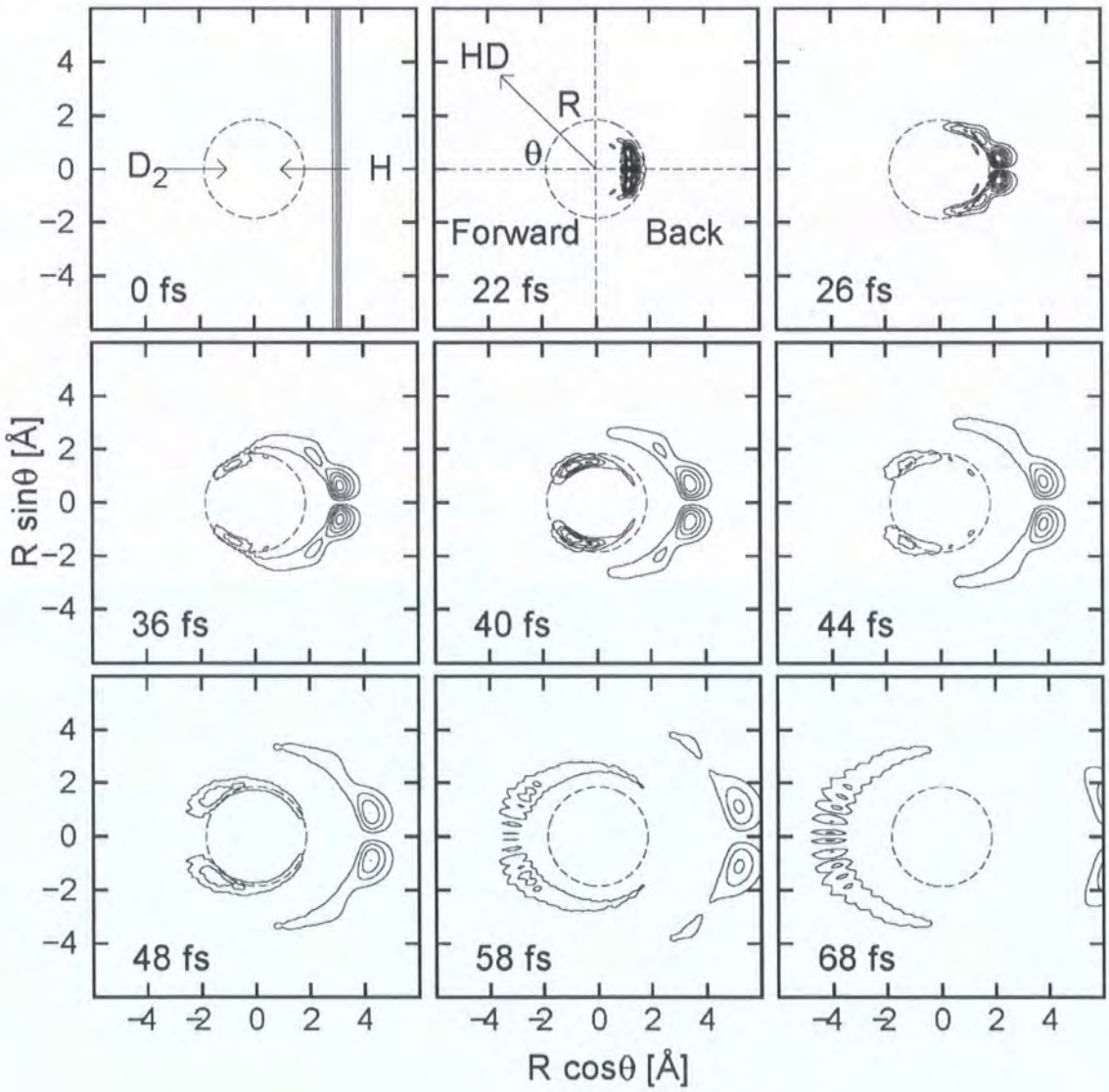

Figure 3.1: Snapshots from the quantum simulation of the H + $D_2(v = 0, j = 0) \rightarrow$ $HD(v' = 3, j' = 0)$ + D reaction [1]. The contours are obtained from the complete wavefunction of the reaction, and show the time evolution of the $HD(v' = 3, j' = 0)$ product, as a function of the centre-of-mass scattering angle θ. The dashed circles are of radius $R = 1.85$ Å and give a rough indication of the extent of the transition state region. Two reaction mechanisms are visible, separated by a time delay of about 25 fs.

The calculations are able to reproduce time-of-flight data from an experiment of Zare and co-workers with good agreement [1], thus it was concluded that the time delay in the calculations is real.

The earlier mechanism that scatters in the backwards direction (as shown in panel 22 fs), is attributed to the direct 'recoil' mechanism.

3.1.1 Elucidation of Forward Scattering Mechanisms

The mechanism that leads to forward scattering is of great interest, and may give indications of a scattering resonance. It has been shown that QCT calculations can be used to define mechanisms which have long time delays [57]. QCT is unable to reproduce quantum effects so it must be demonstrated that QCT results can match the QM picture (Fig. 3.1) sufficiently well to be able to describe any classical mechanisms behind the quantum process. The QCT method was used to study reaction mechanisms on the fly. The backwards scattering mechanism, thought to be caused by direct recoil, was investigated along with the forwards scattering mechanism.

3.2 Using QCT

As described in Section 2.3.2, in the quasi-classical method the D_2 is prepared in a discrete internal energy state corresponding to the initial quantum state of the molecule ($v = 0$, $j = 0$). Having selected the rovibrational state and the initial collision energy other collision variables are randomly selected from the relevant classical distribution functions. Once the trajectory has started, the quantum restriction is relaxed so that the time evolution of the system is governed solely by classical mechanics. A similar quantisation is employed in the analysis of the product molecule internal energy states, whereby the continuous range of quantum numbers is rounded to the nearest integer.

A more thorough treatment of the method is given in Appendix A, and a very detailed description of method can be found in reference [73] whose approach we follow here.

Initial Conditions

Before a collision trajectory can be calculated the initial state of the system must be specified. The values given to the initial coordinates and momenta depend upon the collision parameters chosen. These parameters define the initial geometry of the system, and make one trajectory different from another. For the collision of A (in this case hydrogen) with BC (in this case D_2) in a selected rovibrational (v, j) state, at a fixed relative collision energy, E_{rel}, there are five collision parameters, some of which are shown in Fig. 3.2. To prepare the initial vibrational state of BC ($v = 0$ for the present calculations) the initial BC bond length, q, is defined as the inner (or outer) turning point of the BC vibration for $D_2(v = 0)$.

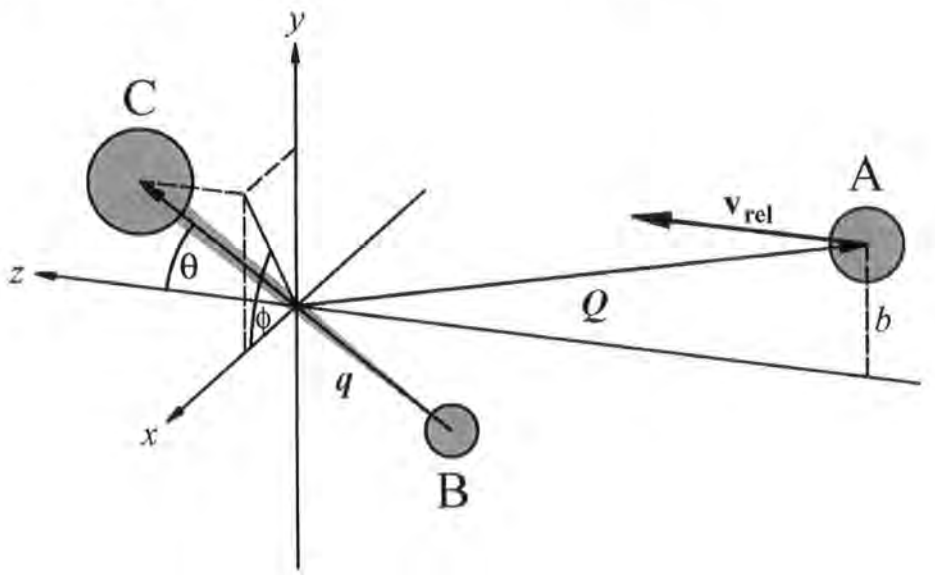

Figure 3.2: The collision parameters (see text) and Jacobi coordinates $(\vec{q}, \vec{Q})$ used to define the initial geometry of a system for QCT calculations.

If we define the centre-of-mass of the BC molecule to lie at the origin and the A atom to lie in the yz-plane, with the initial relative velocity vector, $\mathbf{v}_{\text{rel}}$, of A directed along the $+z$-axis, the initial conditions are:

b The impact parameter, defined as the y distance above the z-axis.

Θ The polar orientation angle of the BC internuclear axis, *i.e.* the angle between q and the $+z$ axis.

ϕ The azimuthal orientation angle of the BC axis, defined as the angle between the projection of q on the xy-plane and the $+x$ axis.

η The orientation of BC angular momentum relative to a reference vector normal to the BC internuclear axis (this is not used as for BC $j' = 0$ in this case).

ξ The phase angle of the BC vibration, as it enters the collision shell (when the atom-diatom distance < 6Å), defined as zero at the inner turning point and π at the outer turning point.

Running a trajectory

The trajectory is calculated by the numerical integration of the equations of motion for the given initial values of the system. The accuracy of the integrations can be checked using conservation of energy and total angular momentum.

The integration in time is continued until the collision products have separated beyond the 'collision shell' distance, ρ_0. Analysis of the collision products can then take place.

The product rotational quantum state, j', is calculated by equating the square of the modulus of the classical rotational angular momentum to $j'(j'+1)\hbar^2$ [60]. With the j' value so obtained the product vibrational quantum state, v', is found by equating the internal energy of the product molecule to a Dunham expansion in $(v' + \frac{1}{2})$ and $j'(j'+1)$ [60]. The non-integer v' and j' can be rounded to the nearest integer, giving the quasi-classical quantum states.

Once a statistically significant number of trajectories has been calculated using pseudo random collision parameters, quantities such as state-to-state cross sections can be calculated and compared to experimental and quantum theory results.

Limitations

It is important to note that the QCT method is not as accurate as QM, but its inaccuracies are known and can be avoided or justified.

1. The QCT method becomes more reliable the larger the masses of the nuclei and the higher the energy in each degree of freedom of the system.

2. When the total energy of reactants is comparable to or below the minimum potential energy barrier separating reactants from products QCT may seri-

ously underestimate reaction probabilities. The use of QCT in such threshold regions where tunnelling is important should be avoided.

3. QCT will, when used to calculate state-to-state reaction probabilities, misestimate probabilities which are 'classically forbidden' in the classical S-matrix sense. The method is not reliable for predicting small transition probabilities.

4. QCT is not appropriate for predicting resonance features or other interference phenomena.

5. QCT yields more reliable results when the desired information is highly averaged.

Having said that, QCT is still a very powerful tool for studying the hydrogen exchange reaction. To populate the HD($v' = 3$) product state (threshold energy 1.4 eV) the calculations were carried out at energies significantly higher than the barrier (0.4166 eV) so point 2 above is irrelevant to the current work. Point 4 is also irrelevant, as the interference phenomena have already been shown in the QM calculation and the present work is an investigation into the classical mechanisms behind the QM effects.

A program to implement QCT as described above and in Refs. [73, 59] was written by E. Wrede, the core of the program was based on Fortran code written by Aoiz and co-workers to calculate and analyse product properties of quasi-classical trajectories [59, 74].

Chapter 4

The $v' = 3$ Product Quantum State

4.1 Direct Comparison with Quantum Mechanical Calculations

This section will cover the direct comparison of QCT calculations with Althorpe's quantum wave packet calculations [1], as shown in Fig. 3.1.

4.1.1 Method

The QCT program [75] was adapted to cover the range of energies used for the wavepacket calculations. QCT methodology uses a series of random numbers to sample the full range of initial conditions [73] (see also Appendix A). An additional random number was used to sample the collision energy uniformly, over the range of interest.

Reproducing Quantum Snapshots

To ensure ease of comparison with Althorpe's quantum snapshots, the timer for the trajectory was started at the same H-D_2 distance (6 Å) as in the QM snapshots. The QM snapshots were produced by projecting the total wavefunction onto a HD(v', j') product wavefunction to obtain a function which describes when and where the HD(v', j') product is formed and how it scatters [72].

A quasi-classical trajectory was deemed to have progressed to a state where the HD molecule is identifiable after the first minimum in the R_{AB} coordinate. The

QCT program output was modified to produce plots of the location of the HD molecule's centre-of-mass relative to the position of the D atom at the specific times used in Ref. [1]. During the course of the trajectory the position of the atoms was integrated every 0.035 fs. The integration step with the closest time to that of the desired snapshot was used.

Once the correct time step has a suitable product molecule the position of the HD centre-of-mass is calculated as a function of the D-HD distance, R, and scattering angle, θ, relative to the initial direction of the H atom (*i.e.* in planar polar coordinates $R\sin\theta$ vs $R\cos\theta$). This data is then plotted as dots, see Fig. 4.1.

4.1.2 Matching the Quantum Picture

QCT snapshots of HD($v' = 3$, $j' = 0$) were produced by calculating a batch of trajectories using the parameters in Table 4.1. 8,750,000 trajectories were run of which 1,729,372 were reactive and only 793 were in the HD($v' = 3$, $j' = 0$) quasi-quantum state (the full quantum state distribution for these calculations can be found in Table B.1). The selected trajectories were then re-calculated to produce the snapshots.

Parameter	Value
PES	BKMP2 (section 2.3.1)
Integration method	Hammings Predictor-Corrector [76]
integration step size	0.035 fs
initial vibrational number	$v = 0$
initial rotational number	$j = 0$
collision energy, E_{rel}	0.9–2.1 eV
maximum impact parameter	1.35 Å
initial/final atom-diatom distance	6.0 Å

Table 4.1: Parameters of QCT calculations.

To enlarge the statistical sample for comparison the 3,066 trajectories in the HD($v' = 3$, $j' = 0 - 1$) quasi-quantum states were used, as the extra rotation had very little effect upon the distribution of the products in the snapshots.

The QM snapshots used an energy range of 1.3–2.1 eV with a flat distribution damping to zero at the edges [1]. The QCT trajectories that were in the energy range 1.4–2.1 eV were used to compare with the quantum picture, as the threshold for the $v' = 3$ state is 1.4 eV.

The scattering angle, θ, only has a range of 0–180°, so for comparison with the QM snapshots the QCT snapshots are mirrored in $R \sin\theta = 0$, see Fig. 4.1.

4.1.3 QM Comparison

The direct comparison between Althorpe's quantum wavepacket contours and the HD product densities from the QCT calculations is shown in Fig. 4.1. In this plot one can see that the QCT calculations match the general temporal and spatial trends in the contours. Backwards scattered products are formed first and have the greatest density, with a gap in the middle at $\theta = 180°$. The 'arms' leading from backwards to sideways scattering are also seen in both cases. In both methodologies the forwards scattered products were formed last and moved further forwards around the transition state region towards each other.

Whilst the general trends of the QCT calculations are the same, the complete separation of the time delayed forwards and fast backwards mechanisms, as apparent in the QM snapshots (40 fs frame of Fig. 4.1), is not seen in the QCT calculations. The QCT result shows none of the enhanced intensity in the transition state region in the 40 fs frame. This may be due to the QM methodology in which the snapshots are produced by projecting the total wavefunction onto a HD(v', j') product wavefunction [72], thus recrossing trajectories are also included in the product density. QCT only uses trajectories that scatter to the HD(v', j') product state to reproduce the snapshots, so densities in the transition state region may not be comparable.

There are further differences between the QCT and QM snapshots that require an explanation: (i) The interference pattern in the forwards scattered region of the QM snapshots (an example of the glory effect [65]) is not seen for the forward scattered QCT products that move round to 'meet' each other. (ii) The fast wings to the sides of the of backwards scattered QCT products are not present in the QM picture. Such quantum interference effects would not be expected in the QCT

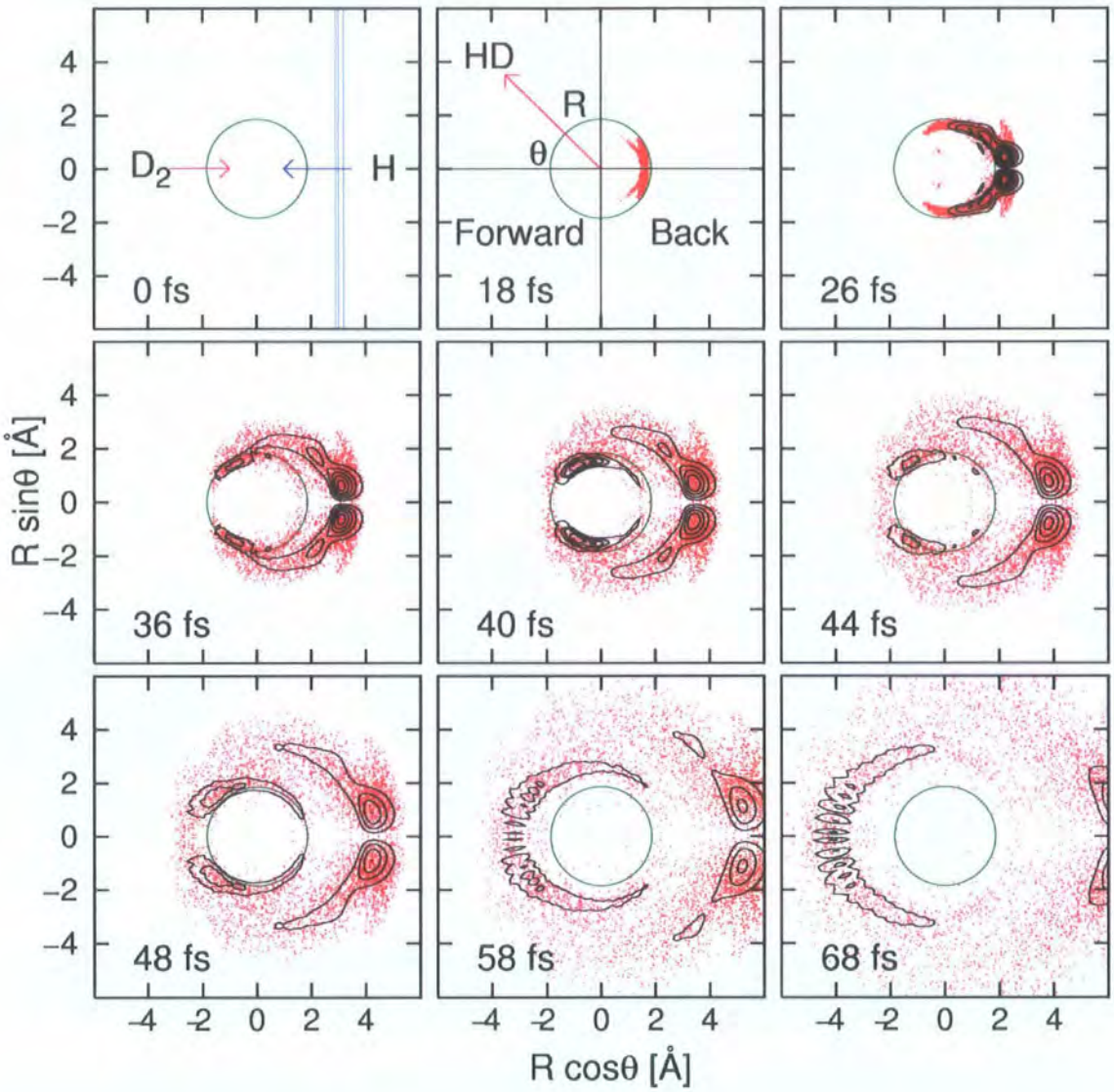

Figure 4.1: Snapshots of the QCT H + $D_2(v' = 0, j' = 0) \rightarrow HD(v' = 3, j' = 0\text{–}1) + D$ calculation over the energy range 1.4–2.1 eV overlaid with contours from Althorpe's quantum wavepacket simulation, see Figure 3.1. The height of the contours and the density of the dots indicates the quantity of $HD(v' = 3, j' = 0\text{–}1)$ molecules in that region.

results, and may also explain other discrepancies between the results.

Whilst the bulk of the QCT picture matches the QM, the QCT picture lacks definition. Better resolution was required to discern any classical reaction mechanisms that govern the scattering into the $HD(v' = 3, j' = 0 - 1)$ product states.

4.2 QCT Calculations

Restriction of initial and final conditions for QCT calculations was used to clarify the scattering dynamics of the HD($v' = 3$, $j' = 0 - 1$) product. The following restrictions were imposed.

Fixed collision energy: The use of a single collision energy gave the product molecules in any given quantum state the same relative product kinetic energy, E_{rel}, and therefore speed. This means that the time dependence of the trajectories is more clearly defined in the snapshots.

Restricted final quantum state: The QCT method assigns a continuous product state quantum number, consequently each assigned quantum state has a range of internal, and therefore kinetic, energies. This was refined by using a restricted product quantum state range, giving the products a well defined recoil speed, *e.g.* for $v' = 3$, quasi-$v' = 2.9$–3.1 was used instead of 2.5–3.5.

Two dimensional restriction: The trajectories could be restricted to the yz-plane, see Fig. 4.2, simplifying the analysis of the trajectories and making visualisation easier. *N.B.* three dimensional trajectories are used to test any hypothesis resulting from two dimensional results.

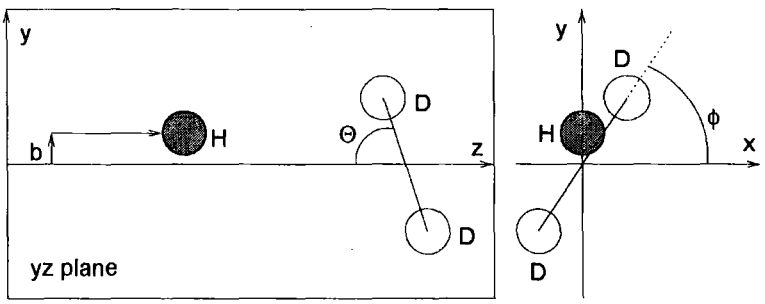

Figure 4.2: Initial conditions for a trajectory, where b is the impact parameter, Θ is the initial polar orientation angle of the D_2 axis and ϕ is the initial azimuthal orientation angle of the of the D_2 axis, where the D_2 centre-of-mass lies at the origin.

Figure 4.3 shows how the out-of-plane angle of the D_2 axis, $\alpha = \arcsin(\sin\Theta\cos\phi)$, changes with scattering angle, for trajectories in the HD($v' = 3$, $j' = 0 - 1$) product state with an $E_{\text{rel}} = 1.85$ eV. For scattering angles less than 150° the system

is very planar, so using a two dimensional restriction was appropriate to aid the investigation into the reaction mechanisms.

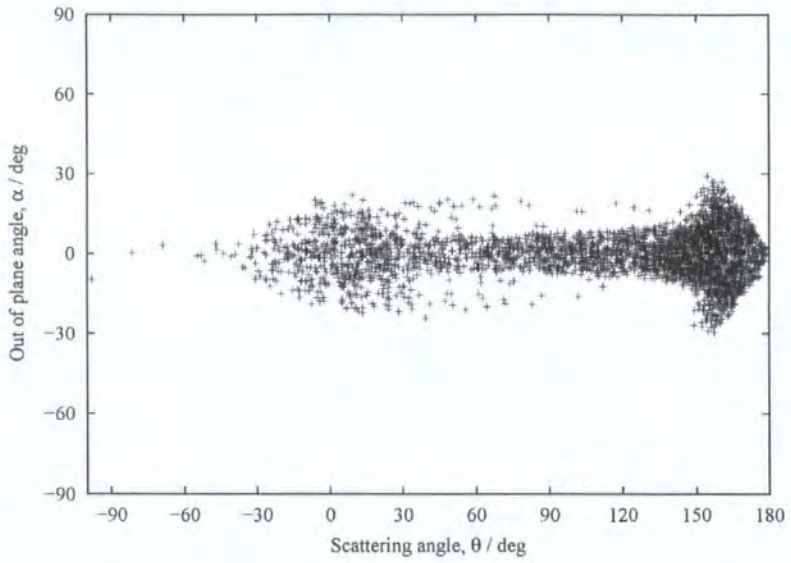

Figure 4.3: Angle of the D_2 internuclear axis out of the yz-plane as a function of scattering angular range. An out-of-plane angle of 90° indicates that the D_2 internuclear axis is perpendicular to the yz-plane, and 0° indicates a planar trajectory. This plot clearly demonstrates the tendancy of trajectories that lead to the HD($v' = 3$, $j' = 0$–1) quantum state at $E_{\text{rel}} = 1.85$ eV, to be planar.

4.2.1 Results

Calculations were carried out at several energies within the range of the energy scan used to match the quantum snapshots, using the QCT parameters shown in Table 4.1. The results of these calculations are summarised in Table 4.2.

Fig. 4.4 shows snapshots created using a single collision energy (1.85 eV), restricted final quantum state, and planar trajectories. An advantage of the QCT method is the ability to distinguish between products scattered in the positive y hemisphere (the same side as the impact parameter, b), see Fig. 3.2, and those scattered in the negative y hemisphere, called positive and negative scattering respectively from now on. This is achieved by testing the y coordinate of the HD product, if y is negative then the scattering angle is assigned a negative sign. Thus trajectories that scatter into the negative region can be discerned (as can be seen *e.g.* in the bottom half of frame 26 fs in Fig. 4.4). Figure 4.4 shows a much 'sharper'

E_{rel}	Dimensionality	Total	Reactive	v'=3, j'=0–1	QSD
2.10 eV	2D	1,000,000	288,003	1,785	Table B.2
1.85 eV	2D	1,000,000	298,819	2,300	Table B.3
1.85 eV	3D	5,000,000	1,082,947	3,346	Table B.4
1.64 eV	2D	1,000,000	300,125	2,266	Table B.5
1.64 eV	3D	1,000,000	210,992	511	Table B.6
1.49 eV	3D	1,000,000	203,834	279	Table B.7

Table 4.2: QCT Calculation results for a range of energies, showing the total number of trajectories calculated, the number of reactive, and the number that are in the HD($v' = 3$, $j' = 0 - 1$) quasi-quantum states. A full quantum state distribution (QSD) can be found in the appropriate table given in the final column.

picture when compared to Figure 4.1, the main scattering feature is shown to have a spiral form. This spiral feature was also observed for the other energies studied.

4.2.2 Investigations into Mechansims

The backwards scattered products are believed to form via a direct recoil mechanism which is collinear at attack. QCT calculations have previously shown that forwards scattering requires a large impact parameter for a glancing attack [3, 56]. It was shown that high J values in QM calculations, the equivalent of large impact parameters in QCT, also give rise to forwards scattering [1].

Both the direct recoil and glancing attack mechanism can only originate from highly correlated initial conditions, *i.e.* all the atoms have to be aligned for direct recoil.

In the next sections the correlations of initial conditions will be investigated along with an analysis of how the hydrogen atom 'impacts' upon the steep potential around the D_2. The impact and recoil mechanisms can be confirmed by analysing the configuration of the atoms at the point of impact, and the angle of the impact from the path of the incoming H atom, which relies heavily on the initial orientation of the system.

To investigate the time delayed forwards scattering mechanism the motion of the system in the transition state was examined and a measurement of the time delay was implemented. The analysis of the transition state region informed much of the other areas of analysis, and as such the following sections can not be seen as

independent, but should be viewed as a whole.

The analysis in the following sections will be concerned with the HD($v' = 3$, $j' = 0 - 1$) product states exclusively.

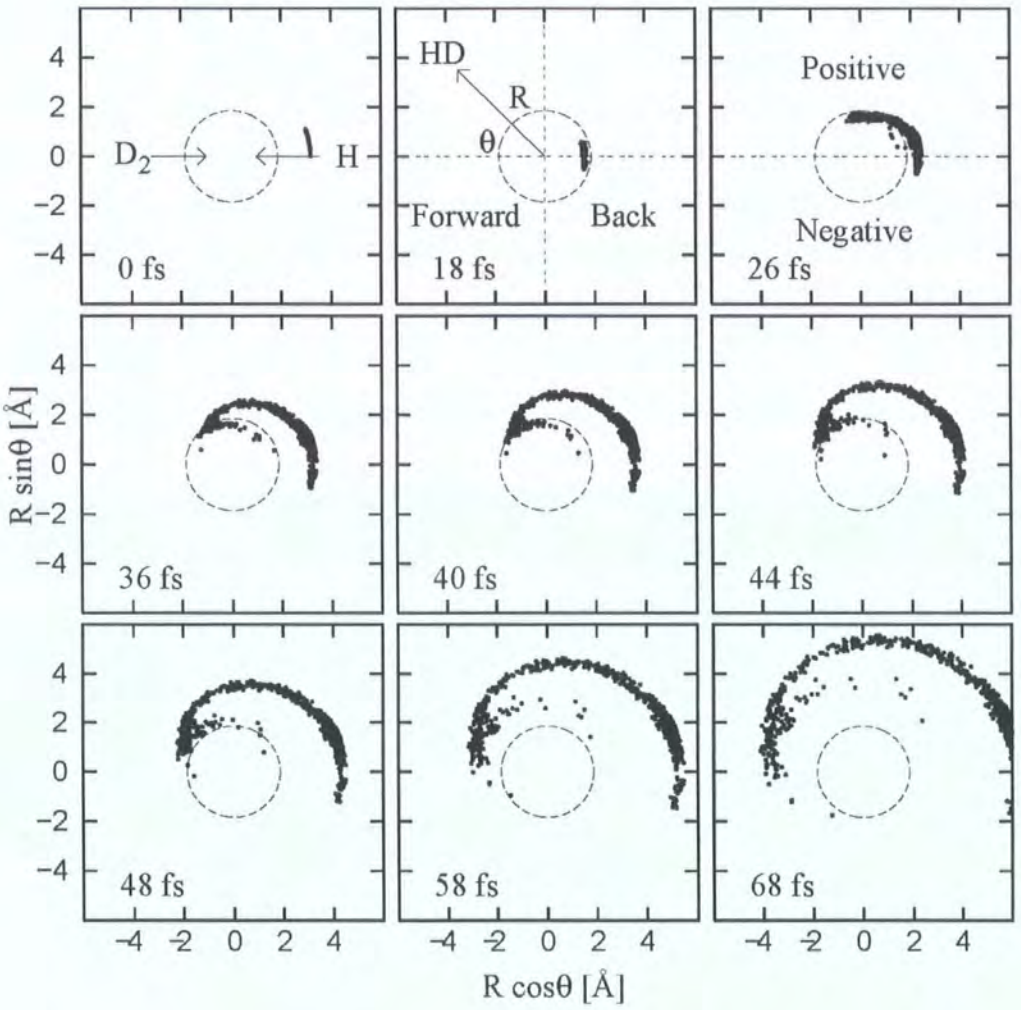

Figure 4.4: Snapshots of the HD product densities for H + $D_2(v' = 0, j' = 0)$ $\rightarrow$ HD($v' = 3$, $j' = 0$–1) + D at $E_{\text{rel}} = 1.85$ eV, restricted to the yz-plane. Each point represents the position of a HD product for a single trajectory. The central circle gives an indication of the size of the interaction region, and the arrow in panel 18 fs is pointing in the forward scattered direction. The trajectories have not been symmetrised, as in Figure 4.1, the positive and negative scattering regions are delineated in panel 26 fs. The spiral shows a continuation from backwards to forwards scattering.

4.3 Impacts

4.3.1 Method

In order to assess the validity of the supposition that glancing impacts give rise to sideways and forwards scattering it became desirable to know the configuration of the atoms at the point of first impact.

The QCT program was adapted to record the point of first impact of the H atom with the steep potential around the D_2, see Fig. 2.2. An initial criterion used to define an impact was the first clear maximum in the potential energy, a point at which the hydrogen atom is slowest, *i.e.* it has converted its kinetic energy into potential energy. This was found to provide useful information, but the first maximum in the potential is not well defined because of the molecular (reactant and product) vibration (see the dashed line in Figure 4.5). An adjusted potential

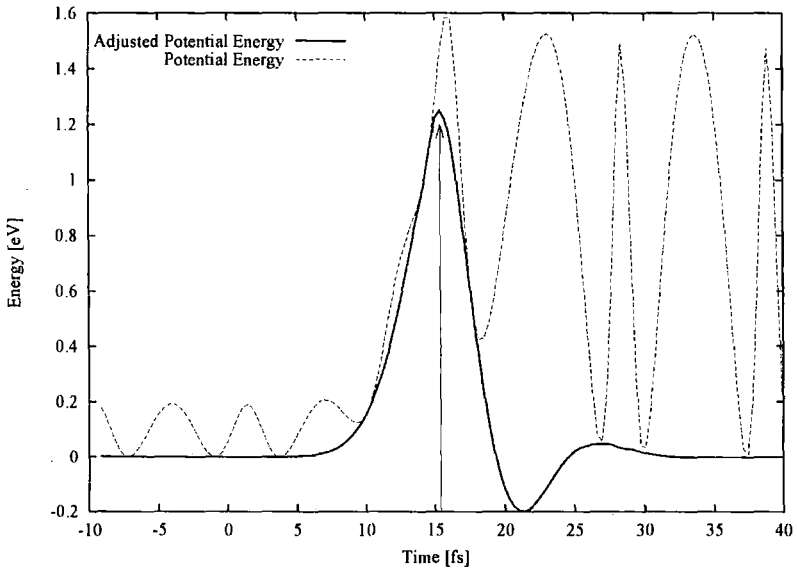

Figure 4.5: Recording impacts using the adjusted potential, $PE_{adjusted} = PE - PE_{molecule}$. The arrow shows the maximum in this adjusted potential, which is recorded as the time of impact.

was devised to remove the (current, as defined by the smallest internuclear distance) molecular vibration from the total potential (PE), $PE_{adjusted} = PE - PE_{molecule}$. This is shown as the solid line in Figure 4.5. The first maximum in the adjusted potential is recorded as the impact. For simple trajectories this is the only maximum, but for some trajectories the D_2 vibration caused the recording of a 'fake' impact with

the van-der-Waals well, so the first two impacts are recorded to enable the removal of the van-der-Waals impact from the analysis. Inspection of the trajectories shows that it is possible to record many peaks in the adjusted potential for long lived trajectories.

Information was recorded at the impact point about the relative positions of the three atoms. Using this information it became possible to produce an 'impact diagram', a plot of the first point of impact of the H atom on the H_3 potential surface, overlaid with a trace of the path taken by the H atom. This method was used to clarify the mechanism of the trajectory. For a direct recoil mechanism one would expect a single hard impact on the outside of the D_2 with a collinear arrangement at impact.

4.3.2 Backwards Recoil

As its name suggests this mechanism leads to 'backwards scattering' of the HD products, which recoil from the collision at centre-of-mass angles close to 180°. Backwards recoil may be written as:

$$\text{D-D} \quad \leftarrow \text{H} \qquad \Rightarrow \qquad \leftarrow \text{D–D} \leftarrow \text{H} \qquad \Rightarrow \qquad \leftarrow \text{D} \quad \text{D-H}\rightarrow$$

where the single arrows indicate the direction of motion of the atoms involved. This mechanism is thought to make up the bulk of all reactive trajectories. Backwards recoil can be more accurately demonstrated using the impact diagram Fig. 4.6. This

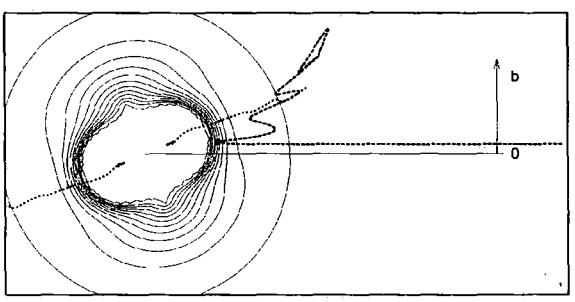

Figure 4.6: Impact diagram of a trajectory leading to a HD($v' = 3$, $j' = 0 - 1$) backwards scattered product. The dotted lines represent the motion of the D atoms; the H atom (dashed line) approaches from the right, its impact is marked with a •. The impact parameter, b, can clearly be seen as the distance above the solid line. The contours represent the H_3 PES at the impact geometry (see Fig. 2.2 panel (A)).

mechanism clearly explains the trajectories that scatter backwards, but how does a trajectory scatter sideways?

4.3.3 Glancing Impacts

To investigate the sideways scattering mechanism the initial conditions were tested for correlations with scattering angle. Results from two dimensional calculations were used to deconvolute the analysis.

Two Dimensional Results

A correlation was found between impact parameter and scattering angle, shown in Fig. 4.7, which demonstrates the continuity of the scattering from backwards to forwards. The forwards region, $\theta < 30°$, can only be accessed with the highest

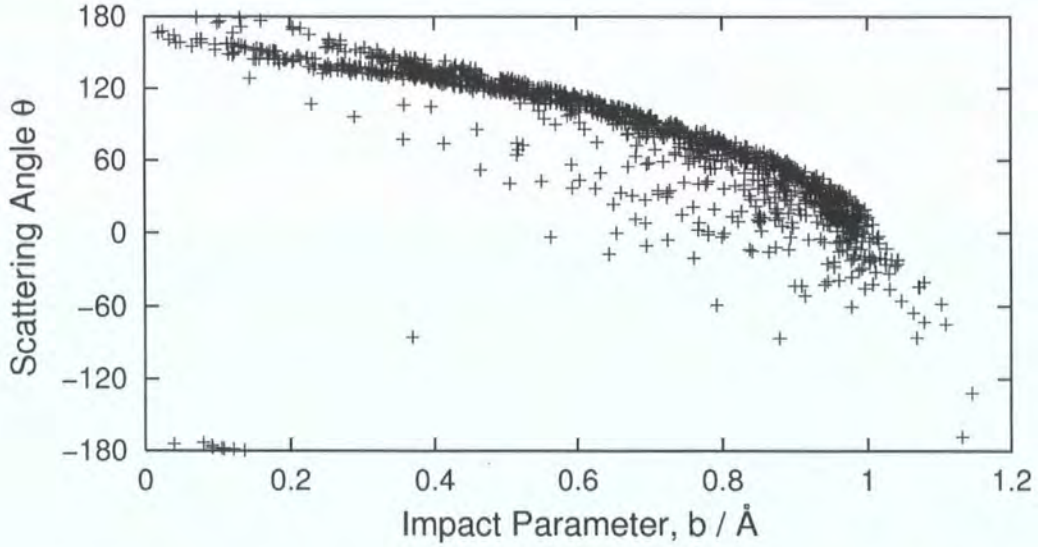

Figure 4.7: Plot showing the Scattering angles correlation with impact parameter for HD($v' = 3$, $j' = 0 - 1$) at $E_{\text{rel}} = 1.85$ eV for planar trajectories.

impact parameters. The implications of this correlation for the impact mechanism of backwards scattering (see Fig. 4.6) can be seen for a range of scattering angles in Fig. 4.8.

The left-hand panels show impact diagrams, *c.f.* Fig. 4.6. The right-hand panels show the trajectories in the product and reactant channels of the PES (see Fig. 2.1) at the bending angle at impact. These 'RR plots' show the interaction region as a dashed line box in the lower left hand corner, and the barrier is the diagonal

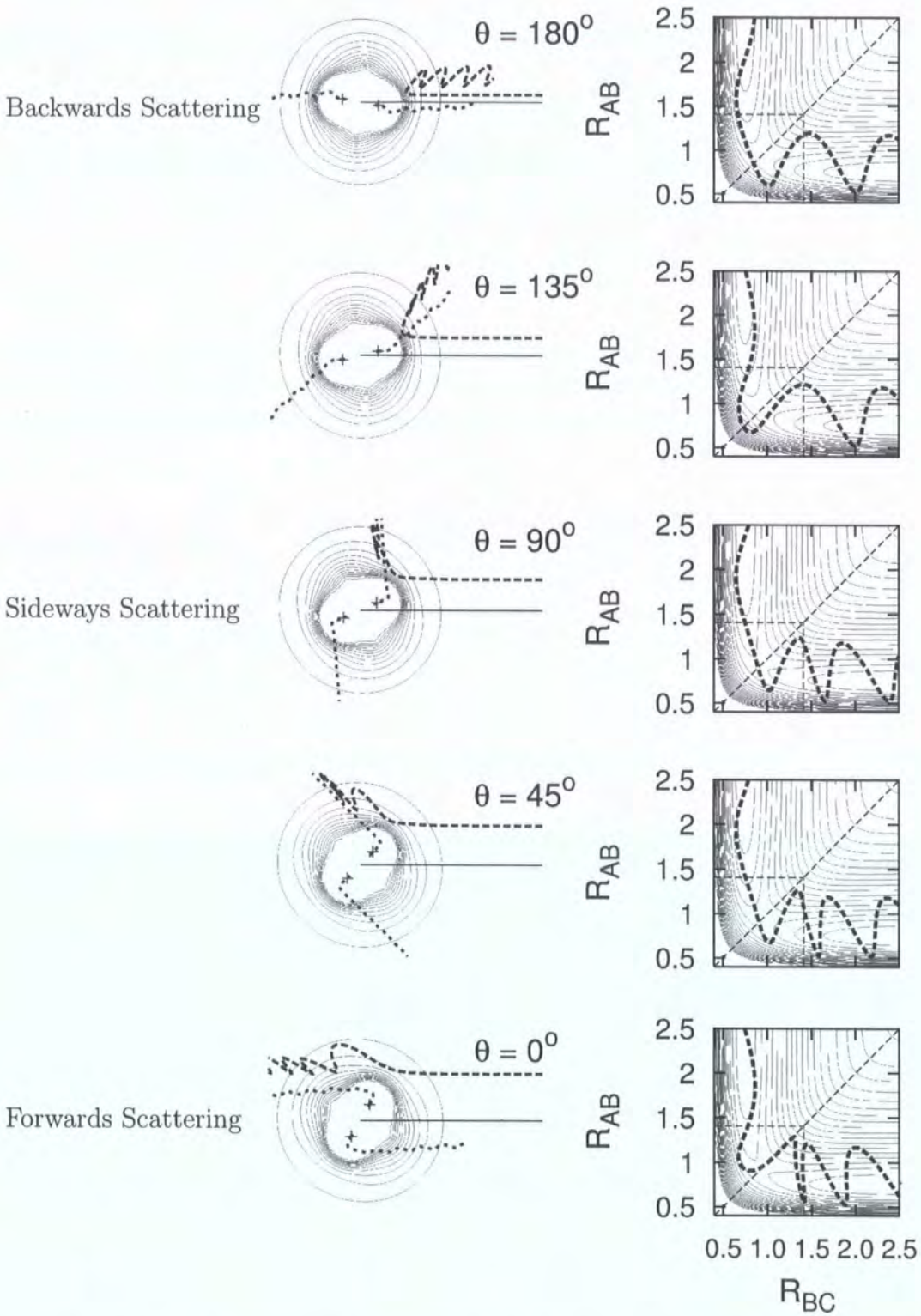

Figure 4.8: Impact diagrams (left): The dotted lines represent the motion of the D atoms; H atoms (dashed line) approach from the right *c.f.* Fig. 4.6. Contours represent the potential at the impact geometry. RR plots (right): Reactant *vs.* product bond lengths; trajectories start from the top left-hand side of the plot (R_{BC} small), the interaction region is represented by the dashed line box in the lower left hand corner. See text for details of trajectories.

dashed line. Motion of the hydrogen atom along or parallel to this line indicates a symmetrical stretching of the atoms.

The RR plot for θ=180° demonstrates the simplicity of backwards scattering; the trajectory moves directly across the reaction barrier and out of the interaction region. The θ=135° RR plot shows symmetric stretch behaviour, not all trajectories at this scattering angle demonstrate this behaviour. All trajectories forwards of θ=135° can undergo this type of stretching motion, which slows passage over the interaction region. Trajectories at each scattering angle display a range of transition state behaviour. There is a trend towards bunching-up of product state maxima in the interaction region for more forwards scattered trajectories, which also slows passage over the interaction region.

These trajectories also contain information about the rotation of the HD_2 complex, the sharp bends in the motion of the D atoms (dotted lines) indicate the magnitude of the rotation of the complex.

The following is a description of the trajectories shown in Fig. 4.8:

Backwards (θ=180°)**:** A low impact parameter and collinear attack result in direct recoil with no rotation of the complex. RR plot: The trajectory passes quickly through the interaction region with no complex excitation.

Sideways (θ=90°)**:** Glancing impact. The H atom approaches with a larger impact parameter and the D_2 axis is angled for an end-on impact, causing some rotation of the complex. RR plot: This trajectory is slightly delayed in the interaction region, the first maximum of the product vibration is within the interaction region.

Forwards (θ=0°)**:** Glancing impact. The H atom approaches at a very large impact parameter with the D_2 axis nearly perpendicular causing a glancing deflection of the H atom off the repulsive potential close to the D_2 and a large rotation of the complex. RR plot: Trapping in the interaction region is shown as a prominent symmetric stretch motion (R_{AB} and R_{BC} expand and contract concertedly) compared to backwards and sideways scattering.

Three Dimensional Trajectories

The two dimensional case has shown that a hard, end-on impact is required for the reaction to attain the HD($v' = 3, j' = 0-1$) product state, this was also found in the

three dimensional case. This restricts the possible initial orientations to those which will allow this hard collinear impact, whilst still giving the full range of scattering angles. These initial orientations are depicted in Fig. 4.9, where the orientation of the D_2 internuclear axis is represented as a point relative to the incoming z-axis. Using the polar orientation angle, Θ, the azimuthal orientation angle, ϕ, (see Fig. 3.2), and the equilibrium D_2 separation, R_e, the location of the leading deuterium atom is projected onto the xy-plane. R_e is used to make the orientation of the trajectories comparable. The circle in panel (B) has a radius of R_e, thus any trajectory at the circle represents a D_2 axis perpendicular to the z-axis.

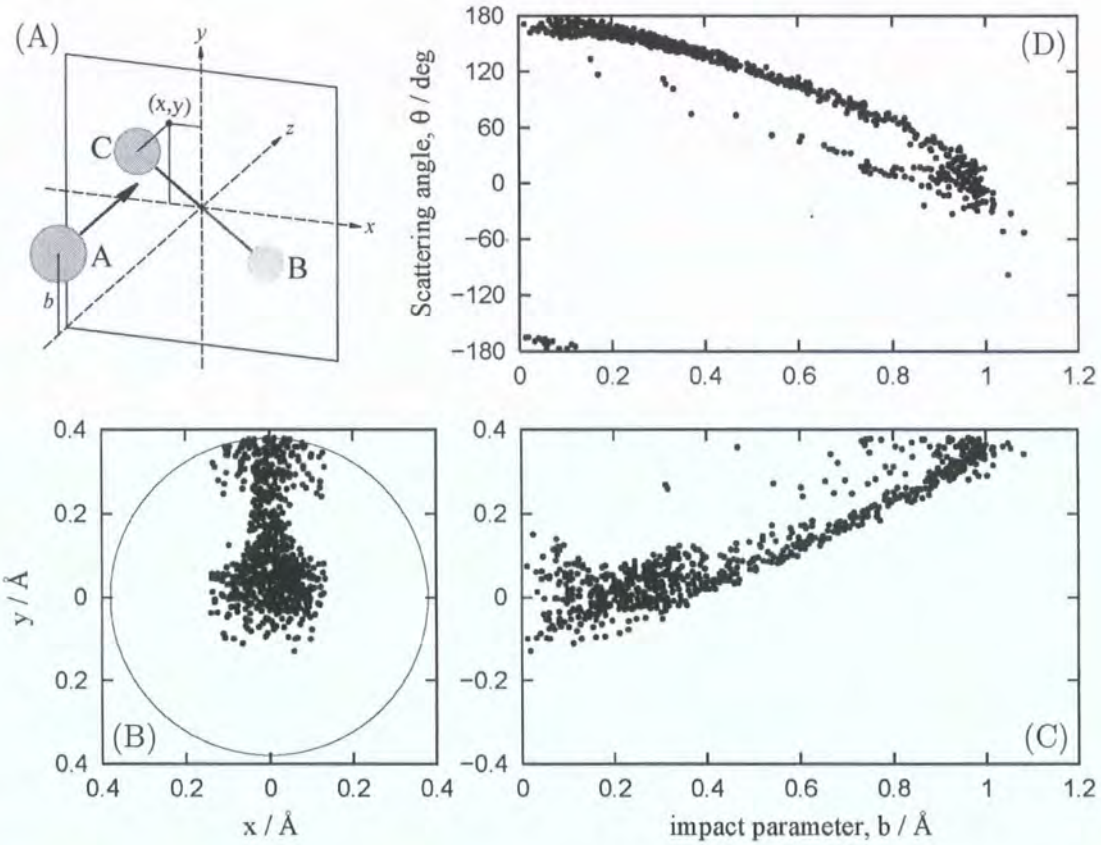

Figure 4.9: Plots showing the impact parameter, b, scattering angle, θ, correlation for the HD($v' = 3$, $j' = 0 - 1$) state at E_{rel}=1.85 eV. (A) Initial conditions for a trajectory: impact parameter, b, and location of the leading D atom projected onto the xy-plane, shown in panel (B), see text for details. (C) Correlation between impact parameter and the initial y coordinate of the leading D atom. (D) Correlation between impact parameter and scattering angle. The forwards scattering region, $\theta < 30°$, can only be accessed with the highest impact parameters.

The trajectories are shown to be planar in nature, the yz-plane has an x-coordinate of zero in panel (B), this was initially demonstrated in Fig. 4.3. A

collinear trajectory would be represented by a point at (0,0) in panel (B) with zero impact parameter in panel (C) and a scattering angle of 180° in panel (D). A forwards scattering trajectory would be represented by a point at $x = 0$ and on the top of the circle in (B) with an impact parameter of 0.9 Å and a scattering angle of 0°. Fig. 4.9 demonstrates a continuous mechanism between backwards and forwards scattering caused by the impact parameter increasing concertedly with the D_2 axis orientation.

4.3.4 Impacts Summary

The glancing impact mechanism, where the H atom glides off the end of the D_2, is a natural progression from backwards recoil. With higher impact parameters and the correct initial orientations it can lead to a continuous range of centre-of-mass scattering angles from backwards to forwards. This continuous nature was also shown in the snapshots of Fig. 4.4 where it is shown as an unbroken spiral. High impact parameters and glancing impact have been suspected of leading exclusively to forwards scattering trajectories in a separate mechanism [1], but here it can be shown that it is part of a continuous classical mechanism from backwards to forwards scattering.

It has been suggested that a glancing attack mechanism would have to convert energy initially concentrated in the HDD bend into energy along the HDD asymmetric stretch, to allow the system to pass over the transition state and react [1]. If the energy was initially converted into a symmetric stretch then the HDD complex would be 'trapped' in the transition state for the period of that stretch.

It has already been shown, Fig. 4.8, that the forwards scattered products can undergo a symmetric stretch (R_{AB} and R_{BC} expand and contract concertedly) in the transition state region. Analysis of the transition state behaviour of trajectories was conducted to judge the importance of these observations.

4.4 Transition State Behaviour

The behaviour of trajectories at the transition state is of great interest [57, 56], and can be used to explain time delays [1] found in calculations. Short-lived complexes

at the transition state should cause resonances in reactive scattering [56].

QCT calculations have been used to estimate the time the system spends in the transition state, the time delay of the trajectory. Long time delays have been attributed to trapping in a bending motion [56], or trapping in a symmetric stretching motion [57]. The time delay of a trajectory is in general an ill defined concept, and previous attempts have used arbitrary measurements, some of which were affected by the different recoil speeds that are dependent upon product state [56].

4.4.1 Symmetry Coordinates

To analyse the trajectories in the transition state, it was useful to use a coordinate system that could describe the vibrational motion of a molecule in terms of the readily recognisable structural features, the bond lengths and angles [77], these are called internal coordinates.

For HDD three internal coordinates are required to describe the relative positions of the atoms: r_1 and r_2 are the distances from the centre atom to each of the end atoms, and θ_b the angle between r_1 and r_2. Symmetry coordinates relate to r_1, r_2 and θ_b as follows.

Symmetric stretch coordinate:

$$s_1 = \frac{\Delta r_1 + \Delta r_2}{\sqrt{2}} \tag{4.1}$$

Bending coordinate:

$$s_2 = \sqrt{(r_1 r_2)}\Delta\theta_b \tag{4.2}$$

Antisymmetric stretch coordinate:

$$s_3 = \frac{\Delta r_1 - \Delta r_2}{\sqrt{2}} \tag{4.3}$$

Where $\Delta r_1 = r_1 - r_e$, $\Delta r_2 = r_2 - r_e$ and $\Delta\theta_b = \theta_b - \theta_e$, where $r_e = 0.92976$ Å and θ_e =180° are the equilibrium values at the transition state.

These coordinates were recorded over the time of the trajectory and used to determine if there was trapping in these motions at the transition state.

4.4.2 Method

Fig. 4.10 shows how the symmetry coordinates change over time for trajectories with different 'degrees of trapping'. The bending coordinate was found to correlate to the other symmetry coordinates for certain trajectories, but its interaction with the other coordinates was complex and could not be easily quantified. As such the bending coordinate is not considered in this analysis.

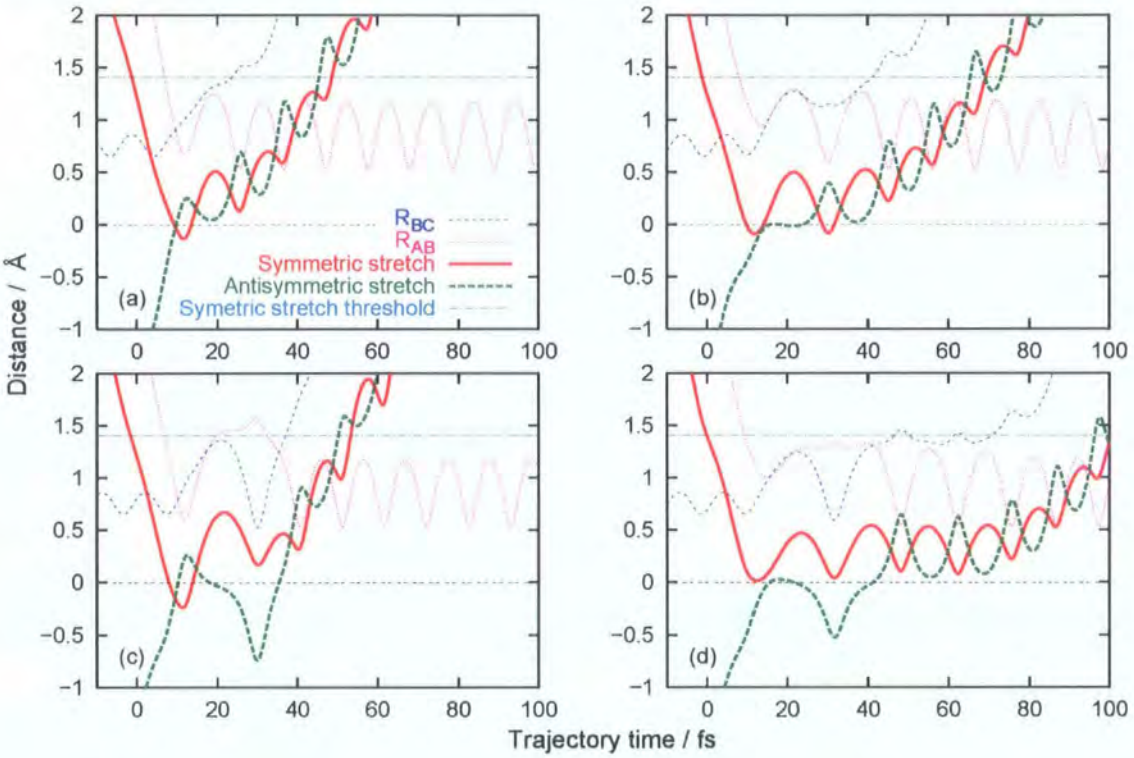

Figure 4.10: Symmetric and anti-symmetric stretch coordinates, compared to bond lengths R_{AB} and R_{BC} are plotted as a function of time for trajectories with different 'degrees of trapping' (see text). The plot also shows the Symmetric stretch threshold (see text).

A threshold can be calculated for the maximum symmetric stretch possible at the given total energy, *i.e.* the largest possible values of R_{AB} and R_{BC} whilst in a linear symmetric ($R_{AB} = R_{BC}$) stretch. This is depicted as the symmetric stretch threshold in Fig. 4.10, and was used as the threshold for a time delay and the 'degree of trapping' criteria (see below). It has the advantage of scaling with collision energy so trajectories run at different E_{rel} can be compared.

The time delay is defined as the time between the R_{AB} coordinate going below the threshold, and the time the R_{BC} goes above the threshold for the last time. This

provided an indication of the amount of time spent in the interaction region where trapping is possible.

For a direct trajectory, shown in frame (a) of Fig. 4.10, little time was spent in the interaction region, so its time delay is small (16.7 fs). The R_{AB} distance goes below the threshold at 6.8 fs and the R_{BC} goes above the threshold at 23.5 fs. But, for a trajectory that goes through a single symmetric stretch motion, frame (b), more time is spent in the interaction region, so its time delay is larger (33.1 fs for this particular trajectory). For a multiple stretching trajectory, frame (d), the time delay is much longer at 61.7 fs.

Trapping was, for our purposes, defined as a time delay caused by a symmetric stretching motion. A symmetric stretch is defined as $R_{AB} \simeq R_{BC}$ expanding concertedly, reaching a maximum, and, at least in part, contracting together. To discern if a trajectory exhibited trapped behaviour, the symmetric and antisymmetric coordinates were monitored during each trajectory. The number of minima and maxima in the two coordinates that occurred under the symmetric stretch threshold were recorded. A trajectory was said to have a symmetric stretch when at least two minima and one maxima in the symmetric coordinate were recorded under the stretching threshold. Multiple stretches were assigned if a greater number of minima and maxima were recorded. The sign of the antisymmetric stretch coordinate during a symmetric stretch was used to discern if trapping occurred in the reactant or product channel.

The degree of trapping a trajectory experiences can be described by the following generalised criteria (used for all trajectories at all energies):

Not trapped: A direct trajectory that moves quickly across the transition state and therefore has a short time delay, an example is shown in Figure 4.10 panel (a).

Long time delay: This can be caused by trapping or by slow recoil motion of the product due to high product excitation. This criterion is used to check for long time delayed trajectories that are not caused by symmetric stretching motions, and could indicate a separate mechanism. No trajectories of this type were found in the HD($v' = 3$, $j' = 0 - 1$) product states.

'Through-the-middle mechanism': A + BC → A-BC → B-A-C → B + AC; this mechanism, which accounts for 0.1% of reactive scattering, is not considered in this report, but it is important to exclude these trajectories so they do not confuse the analysis of other mechanisms.

Fuzzy cases: These cases have longer time delays, but there is no clear trapping.

Trapped in the product channel: This is shown in panel (b) of Fig. 4.10, the symmetric coordinate shows a large stretch between 16 and 26 fs, whilst the antisymmetric coordinate is zero. The R_{AB} and R_{BC} lengths are expanding and contracting together during this time.

Trapped in the reactant channel: This is shown in panel (c) of Fig. 4.10, during the symmetric stretching motion, R_{AB} and R_{BC} expanding together, the antisymmetric stretch coordinate becomes negative. This indicates the trajectory has recrossed the reaction barrier back into the reactant channel.

Trapped with multiple symmetric stretches: This is shown in panel (d) of Fig. 4.10, the symmetric stretch coordinate has a series of maxima and minima indicating the multiple stretching motions, they have been previously observed by Muga and Levine [57]. These are the most long lived trajectories, but with only a few trajectories per quantum state the contribution to the final classical cross section is negligible. These trajectories scatter to a wide range of angles and can be seen on the interaction region circle in frame 44 fs of Fig. 4.4.

4.4.3 The Importance of Trapping

For QCT the reactive cross section for a batch of trajectories is given by [73]:

$$\sigma = \pi b_{\max}^2 \frac{n}{N}, \tag{4.4}$$

where $b_{\max}$ is the maximum impact parameter sampled (1.35 Å), n is the number of trajectories with a given property (*e.g.* scattered into a given HD(v', j') quantum state or having a number of symmetric stretches) and N is the total number of trajectories run (5,000,000, for $E_{rel} = 1.83$ eV).

Using a histogram binned in cosine scattering angle and Eqn. 4.4 it was possible to produce a differential cross section (DCS) to demonstrate the contribution of symmetric stretching trajectories to the forwards scattering region of the HD($v' = 3$, $j' = 0 - 1$) product states, Fig. 4.11. Backwards scattered trajec-

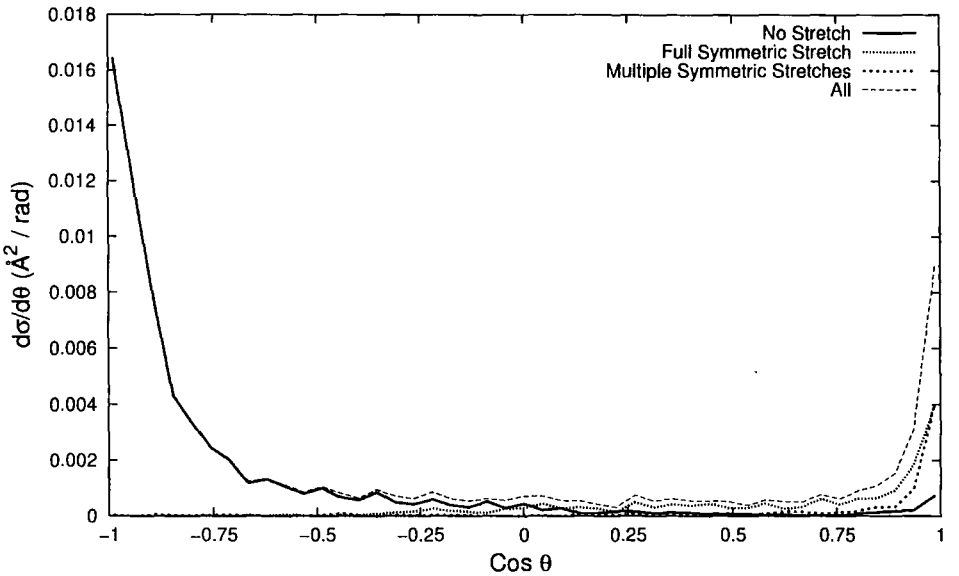

Figure 4.11: Complex excitation as a function of scattering angle. Almost all the forwards scattered trajectories, $\theta < 40°$, $\cos\theta > 0.75$, undergo at least one full symmetric stretch.

tories, $\cos\theta < -0.5$, exhibit minimal contribution from symmetric stretches. As the scattering angle decreases, the number of trajectories undergoing symmetric stretch vibrations of the HDD complex increases. Moreover, the forward scattering mechanism requires the system to undergo these stretching motions.

4.5 Complex Rotation

Fig. 4.8 in Section 4.3.3 demonstrates that the amount of rotation of the HDD complex during the collision is correlated with the scattering angle, θ. As part of the investigation into time delayed scattering it was suspected that the time delay was due to the rotation time of the HDD complex.

The rotation time was defined as the minimum time required for the complex to rotate between its initial and final angles. These initial and final angles are given by the hydrogen's initial approach vector and the products scattering vector which define the scattering plane, the angle between which is the scattering angle, θ. The angular speed, $\vec{\omega}$, was calculated using the moment of inertia tensor, $\mathbf{I}$, of the complex at the closest approach of the three atoms and the total angular momentum of the system, $\vec{L}$, (governed only by the impact parameter, b, for that trajectory, as in this case $j' = 0$).

$$\vec{\omega} = \mathbf{I}^{-1}\vec{L} \tag{4.5}$$

$\vec{\omega}$ is then projected onto the normal vector of the scattering plane (which defines the axis around which the complex has to rotate to get from the initial vector of approach to the final vector of product recoil) to calculate the required speed of rotation, ω. The rotation time, t_{rot} is then given by:

$$t_{\text{rot}} = \theta_{\text{rot}}/\omega \tag{4.6}$$

where the rotation angle is given by: $\theta_{\text{rot}} = 180 - \theta$.

The correlation between t_{rot} and scattering angle is shown along with the time spent in the interaction region (defined by the symmetric stretch threshold, see section 4.4.2 for details) in Fig. 4.12. It can be seen that the major contribution to the time spent in the interaction region is the time required for rotation of the HD_2 complex. A small part of the longer time taken by forwards scattering trajectories can be attributed to the extra distance that has to be travelled, and the extra time it takes to make the first impact. The longer time delays seen in Fig. 4.12 (> 21 fs) are caused by multiple symmetric stretches as well as rotation.

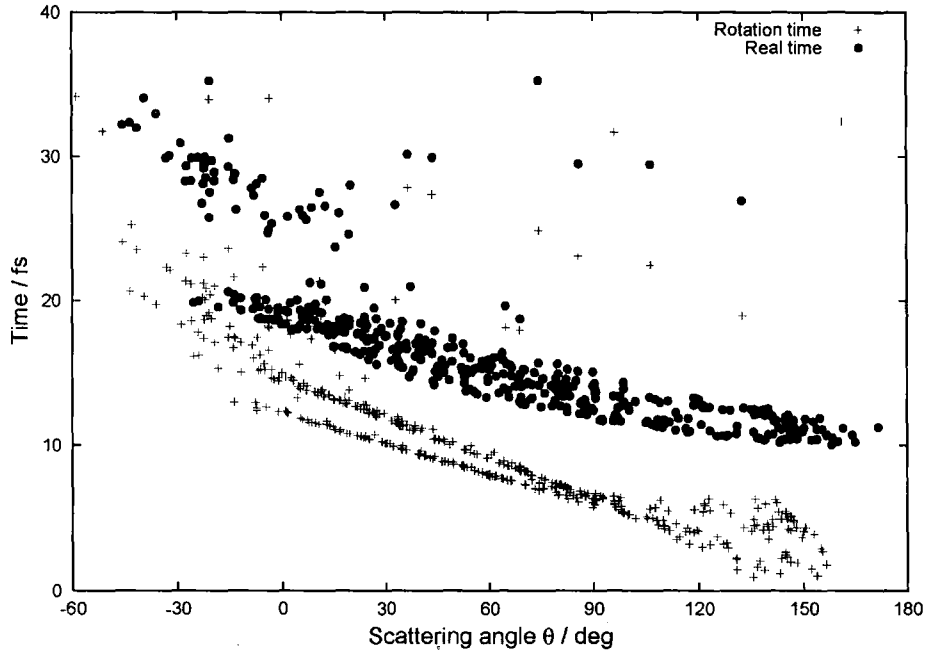

Figure 4.12: Correlation between time and scattering angle. Real time spent in the interaction region (•) compared to minimum time required for complex rotation, t_{rot}, (+), as a function of scattering angle.

4.6 v'=3 Summary

Fig. 4.1 shows that the QCT calculations are a good match for the temporal and spatial trends of the QM results, but the QCT do not have the separation between forwards and backwards scattering, or the quantum effects such as glory scattering. It is proposed that both of these quantum effects can be justified as interferences between two independent classical trajectories that lead to the same scattering angle [8]. The glory scattering derives from the time delayed trajectories moving around the interaction region from sideways to forwards scattering angles and interfering in the forwards region. The separation between forwards and backwards scattering in the QM picture could be seen as an interference between the fast (recoil/glancing) trajectories that scatter sideways and the multiple stretching (trapped) trajectories (sitting on the interaction region circle in frame 44 fs of Fig. 4.4) that scatter into the same region. This effect would be more pronounced if the population of trapped trajectories was enhanced due to a resonance effect.

Using single energy trajectories and restricting the product quasi-quantum state allowed the elucidation of the mechanisms present. The dominant mechanism pro-

gresses from hard collinear impacts to glancing impacts, where the increased time for the sideways and forward scattered trajectories is due to the rotation of the HDD complex and extra distance travelled. This mechanism derives from the strong correlations between the initial conditions of D_2 axis orientation and impact parameter and the scattering angle, as shown in Fig. 4.9.

The minimum distance between the hydrogen and deuterium atoms during a hard collinear impact is the inner turning point of the $v' = 3$ vibration, allowing the excitation into the $v' = 3$ product state. For the glancing impacts the closest approach of the hydrogen does not allow this direct excitation, but the subsequent motion of the atoms, especially if in a symmetric stretch, provides excitation to the $v' = 3$ state through the outer turning point of the $v' = 3$ vibration.

It has been suggested that a glancing attack mechanism would have to convert energy initially concentrated in the HDD bend into energy along the HDD asymmetric stretch, to allow the system to pass over the transition state and react [1]. If the energy was initially converted into a symmetric stretch then the HDD complex would be 'trapped' in the transition state for the period of that stretch.

This study has shown that forward scattered trajectories display a significant amount of symmetric stretch vibrations of the HD_2 complex. These 'vibrations' can be caused by the motion of the H flying past the D_2 before the 1st impact, as a direct consequence of the scattering mechanism, *i.e.* glancing impacts are required for forward scattering and the fly past leads naturally to a symmetric stretch. A significant number of trajectories undergo multiple stretches which are not attributable to a fly past stretch, some even show longer term excitation as previously observed by Muga and Levine [57].

This excitation of transition state vibrations indicates the presence of a scattering resonance. QCT cannot detect resonances or quantum bottleneck states (QBS), but the symmetric stretches described here for the forwards scattered trajectories are consistent with the complex motions predicted for both resonances [19, 67] and QBS [38, 39].

Chapter 5

The $v' = 0$, low j' Product Quantum States

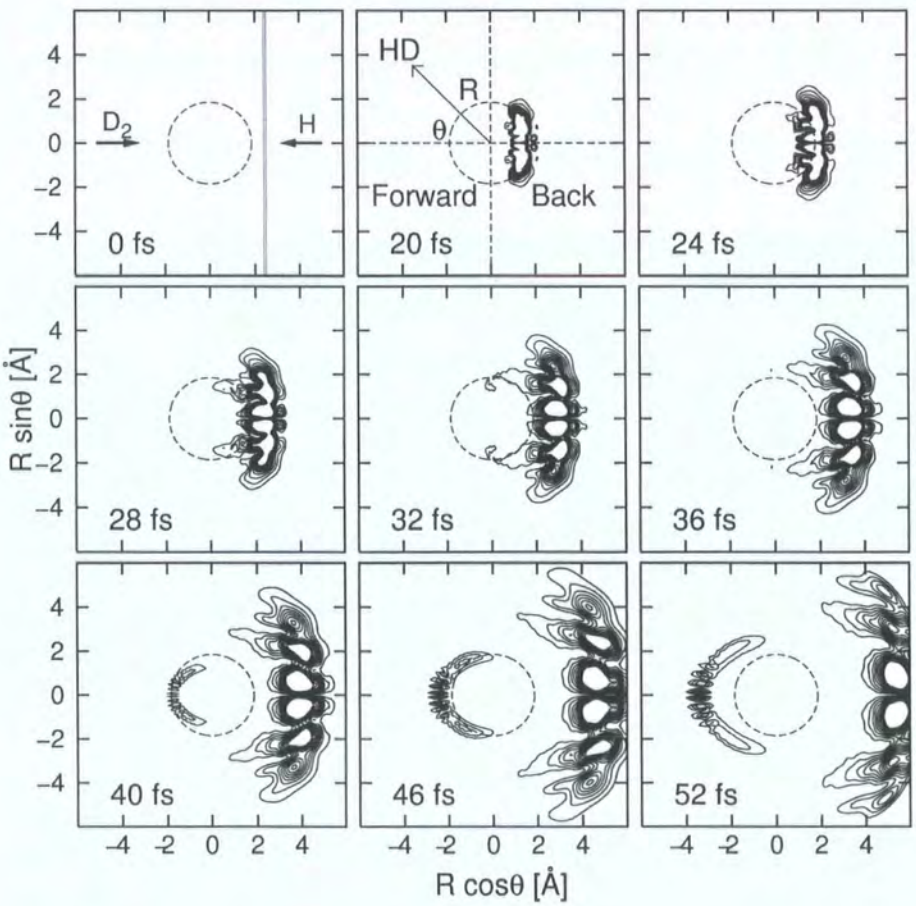

Figure 5.1: Snapshots from the quantum simulation of the H + $D_2(v' = 0, j' = 0)$ $\rightarrow$ $HD(v' = 0, j' = 0)$ + D reaction resulting from a range of collision energies, $E_{\text{rel}} = 0.4 - 2.5$ eV [65] *c.f.* Fig. 3.1.

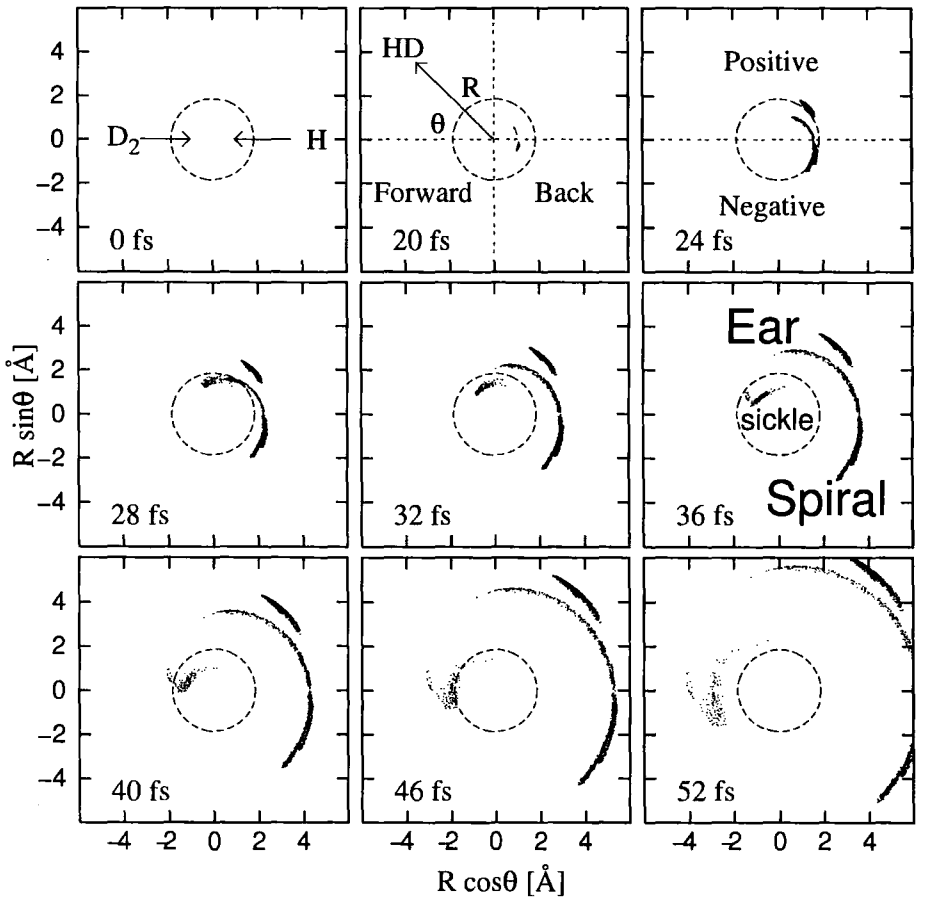

Figure 5.2: Snapshots representing the product densities for HD($v' = 0, j' = 0 - 1$) product molecules (as Fig. 4.4), at a collision energy of 1.85 eV in three dimensions. Panel 36 fs shows labels for the three clear regions of the scattered products, Ear, Spiral and Sickle.

5.1 Introduction

After the investigation of the HD($v' = 3$, $j' = 0 - 1$) quantum state trajectories the techniques and methodology developed were also applied to the HD($v' = 0$, $j' = 0 - 1$) product states, as part of an ongoing investigation into the reaction mechanisms of the hydrogen exchange reaction. The complex nature of reactive scattering is highlighted in the quantum snapshots for the H + $D_2(v' = 0, j' = 0)$ $\rightarrow$ HD($v' = 0, j' = 0$) + D reaction shown in Fig. 5.1.

It was demonstrated in the v'=3 case that the analysis of mechanisms was greatly assisted by the use of single energies and restricting trajectories to the yz-plane, this methodology will be used here before addressing the three dimensional problem.

It was expected, after the v'=3 case, that the dominant mechanism would be the

direct recoil, which would also be consistent with established ideas of the hydrogen exchange reaction [3, 66]. The first visual comparison between the two quantum states can be made between Fig. 5.2 for v'=0 and Fig. 4.4 for v'=3. Fig. 5.2 depicts QCT snapshots representing the time evolution of product densities for HD($v' = 0$, $j' = 0 - 1$) at $E_{\mathrm{rel}} = 1.85$ eV.

First inspection of Fig. 5.2 shows a smoother spiral (labelled in frame 36 fs) than that seen in the v'=3 case, which goes from very negative backwards scattering angles to forwards scattering. There is also greater product density in the negatively backwards scattered region compared with v'=3. The most important differences to note are the separate, and faster product forming region, labelled the Ear, which scatters sideways and the much slower product forming region, scattering forwards, which is labelled Sickle. Three similar regions have been noted before, in a symmetrised scattering angle trajectory time correlation plot, but were never separately examined [56]. The long lived trajectories of the Sickle appear to have a similar configuration to the long lived trajectories in the v'=3 case (see Fig. 4.4) that undergo multiple symmetric stretches.

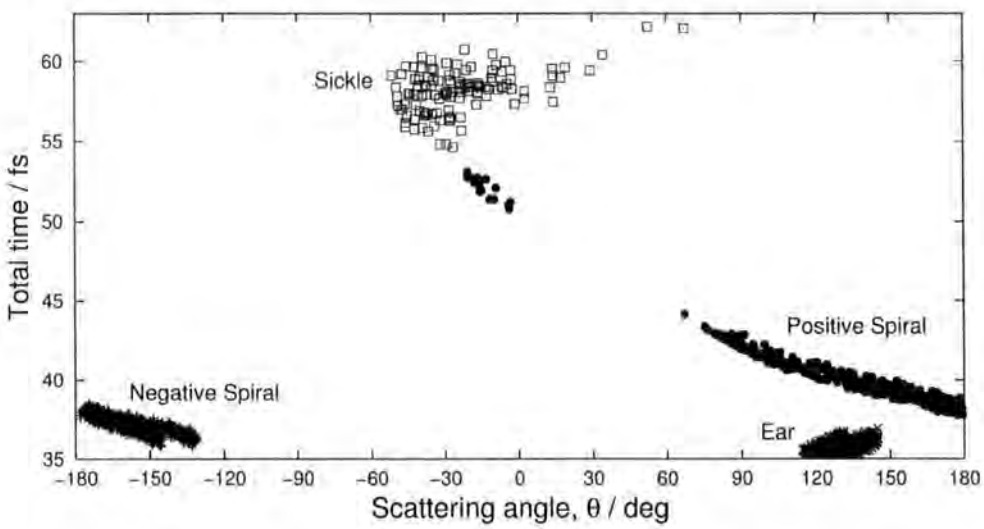

Figure 5.3: Scattering angle–time correlations, for HD($v' = 0$, $j' = 0 - 1$) product molecules, for the three clear regions, Ear, Spiral and Sickle. The full range of QCT scattering angles is shown, the forwards scattering region is in the centre of the graph, with the backwards region shown towards the edges. The trajectories were restricted to two dimensions, in the yz-plane, at an energy of 1.85 eV.

The three separate regions would seem to indicate that three separate mechanisms are at work here, in comparison to the v'=3 case where only one continuous

mechanism was found with the additional time delayed symmetric stretching trajectories. The snapshots in Fig. 5.2 can also be more simply represented by a plot of scattering angle with total time, Fig. 5.3, in this plot the spiral feature has been further subdivided into positive and negative regions according to the scattering hemisphere of the product. This demonstrates that the Ear and Negative Spiral regions are the fastest trajectories scattering to a limited range of angles, whilst the spiral covers a range of scattering angles and time, leading to the Sickle which scatters last and mostly forwards.

In this section it will be shown that, as in the v'=3 case, the spiral trajectories come about from a single mechanism that smoothly evolves over all scattering angles. However, this is not the direct recoil mechanism that leads to the v'=0 state products. The Ear and the Sickle will also be shown to have independent and quantifiable mechanisms.

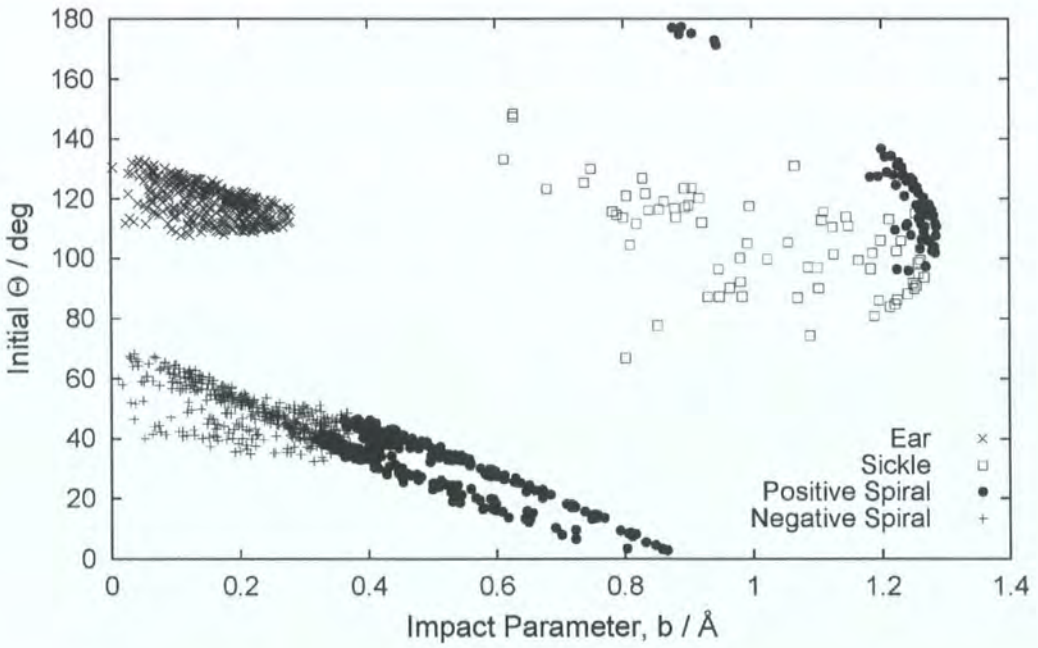

Figure 5.4: Initial conditions: correlation between impact parameter and initial polar orientation angle for HD($v' = 0, j' = 0 - 1$) product molecules in the three regions, Ear, Spiral and Sickle. The trajectories were restricted to two dimensions, in the yz-plane, at a collision energy of 1.85 eV.

For further analysis it was instructive to consider the relationship between the initial parameters leading to the different regions in the snapshot diagram. Fig. 5.4 shows the correlation between impact parameter and initial polar orientation

angle for a system restricted to the yz-plane, (the initial conditions can be seen in Fig. 4.2). The separate regions of the snapshot diagram were found to have highly correlated initial conditions.

5.2 Fast Trajectories

5.2.1 Ear (2D)

The Ear contains trajectories that scatter faster than most other trajectories into a well defined and restricted angular range, see Figs. 5.2 and 5.3. It is produced by a separate unique mechanism due to the initial orientation of the system as shown in Fig. 5.4. This initial orientation causes the H atom in the Ear trajectories to approach the D_2 from the side with a low impact parameter and therefore to impact on the H_3 PES near the conical intersection (CI), as shown in Fig. 5.5 (the spatial features of the CI can be seen in Fig. 2.2). The CI diverts the path of the H atom onto the foremost D atom.

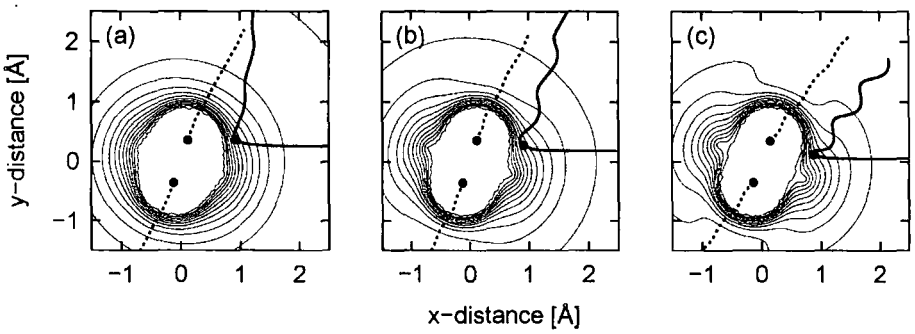

Figure 5.5: Impact diagrams for trajectories from the Ear region, see Fig. 4.6. The dotted lines represent the motion of the D atoms; the H atom (thick solid line) approaches from the right at an impact parameter, b, above $y = 0$, its impact is marked with a • (see Section 4.3). The contours represent the H_3 PES at the impact geometry. The trajectories with the highest impact parameter are the most sideways scattered. The trajectories were restricted to two dimensions, in the yz-plane, at a collision energy of 1.85 eV.

5.2.2 Negative Backwards Scattering (2D)

This Spiral feature contains some of the fastest trajectories, in the negatively scattering backwards region, on a similar time frame to the Ear, see Fig. 5.3, *i.e.* with little

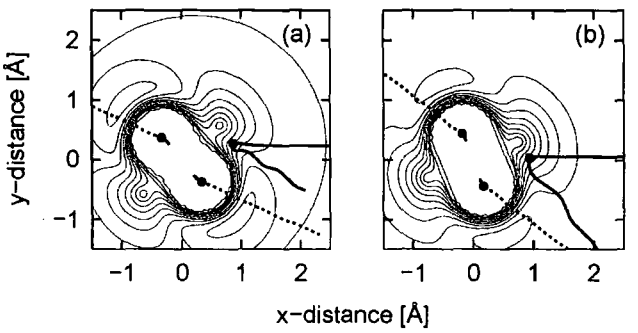

Figure 5.6: Impact diagrams (see Fig. 5.5) for the Negative Spiral region. The trajectories with the lowest impact parameter are the most sideways scattered. The trajectories were restricted to two dimensions, in the yz-plane, at an energy of 1.85 eV.

time delay. Fig. 5.6 shows impact diagrams for scattering to the negative backwards region. It is instructive to note how similar these frames are to the impact diagrams for the Ear, Fig. 5.5. Again, on approach to the D_2 the hydrogen is diverted by the CI onto the foremost deuterium atom.

5.2.3 Conical Intersection Mediated Recoil (2D)

The Conical Intersection Mediated Recoil (CIMeR) mechanism describes the scattering into the Ear and Negative Spiral regions.

Fig. 5.5 demonstrates the impact parameter dependence of CIMeR: as the impact parameter increases the scattering angle becomes smaller. The deviation in the path of the H atom caused by the conical intersection is obviously dependent upon the prominence of the conical intersection, and hence upon the value of the D_2 separation, q, at the point of impact. The shape of the potential in this location causes the Ear trajectories to be scattered sideways. This mechanism cannot produce backwards scattering, as the D_2 axis would have to be perpendicular to an incoming hydrogen with zero impact parameter. Such a trajectory would be non-reactive as the conical intersection would deflect the hydrogen away from the deuterium molecule.

A more detailed description of the CIMeR mechanism is given by the movie sequence in Fig. 5.7 and the following description.

0-15 fs The hydrogen approaches the D_2 molecule with a very small impact para-

meter.

15-18 fs The D_2 bond stretches as the hydrogen approaches, making the conical intersection more prominent. At the point of impact the gradient of the potential deflects the hydrogen away from the centre of the D_2.

18-22 fs The D_2 bond continues to stretch as the hydrogen moves towards the closest D atom, where it also impacts and is repelled by the steep potential at the deuterium atom.

25-29 fs The H atom is captured by the potential well of the D atom.

29-44 fs The products are formed rapidly.

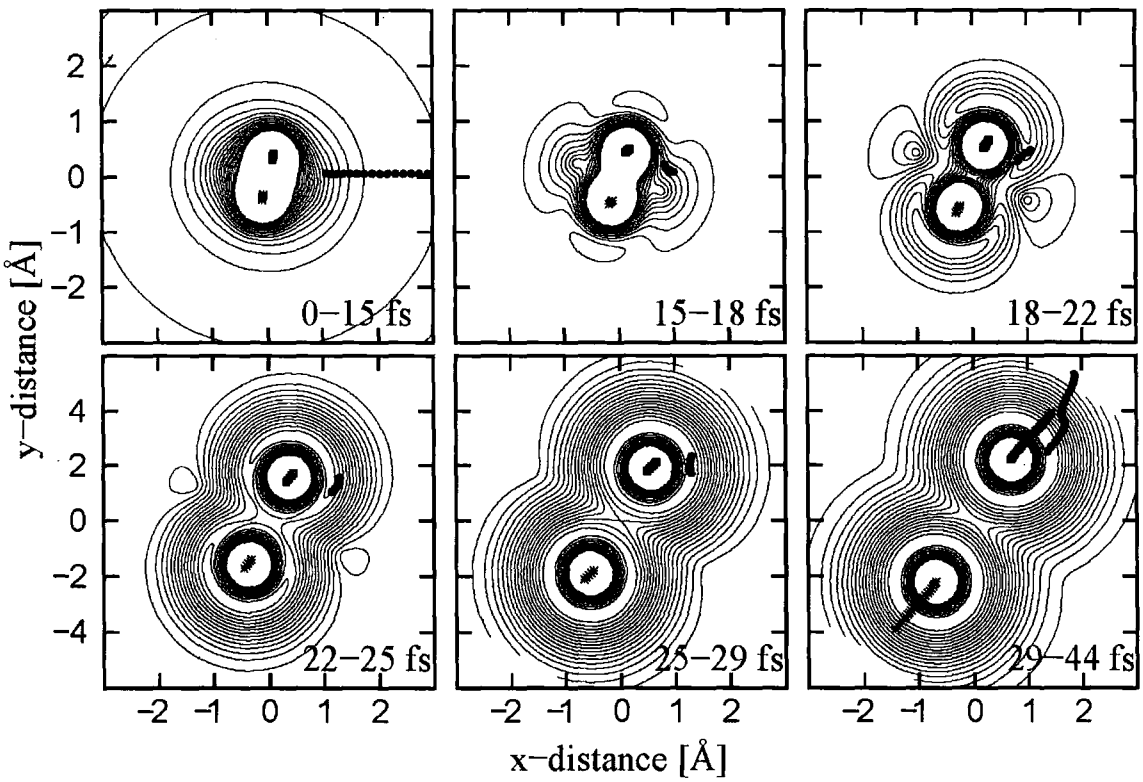

Figure 5.7: Reaction mechanism diagram for a typical trajectory in the Ear region. The second frame shows how the rising potential around the conical intersection deflects the incoming Hydrogen from the centre of the D_2 molecule.

Because of the low impact parameters very little rotation is imparted onto the D_2 at collision. As the interaction with the conical intersection is only slight the mechanism is very direct, showing no signs of complex transition state behaviour.

These are clear demonstrations from the two dimensional case, but the CIMeR mechanism also operates in non-planar trajectories.

5.2.4 CIMeR Mechanism in 3D

Fig. 5.8 shows the correlation between the initial geometry of the collision (the impact parameter and D_2 axis orientation) and the centre-of-mass scattering angle for the CIMeR mechanism, *c.f.* Fig. 4.9.

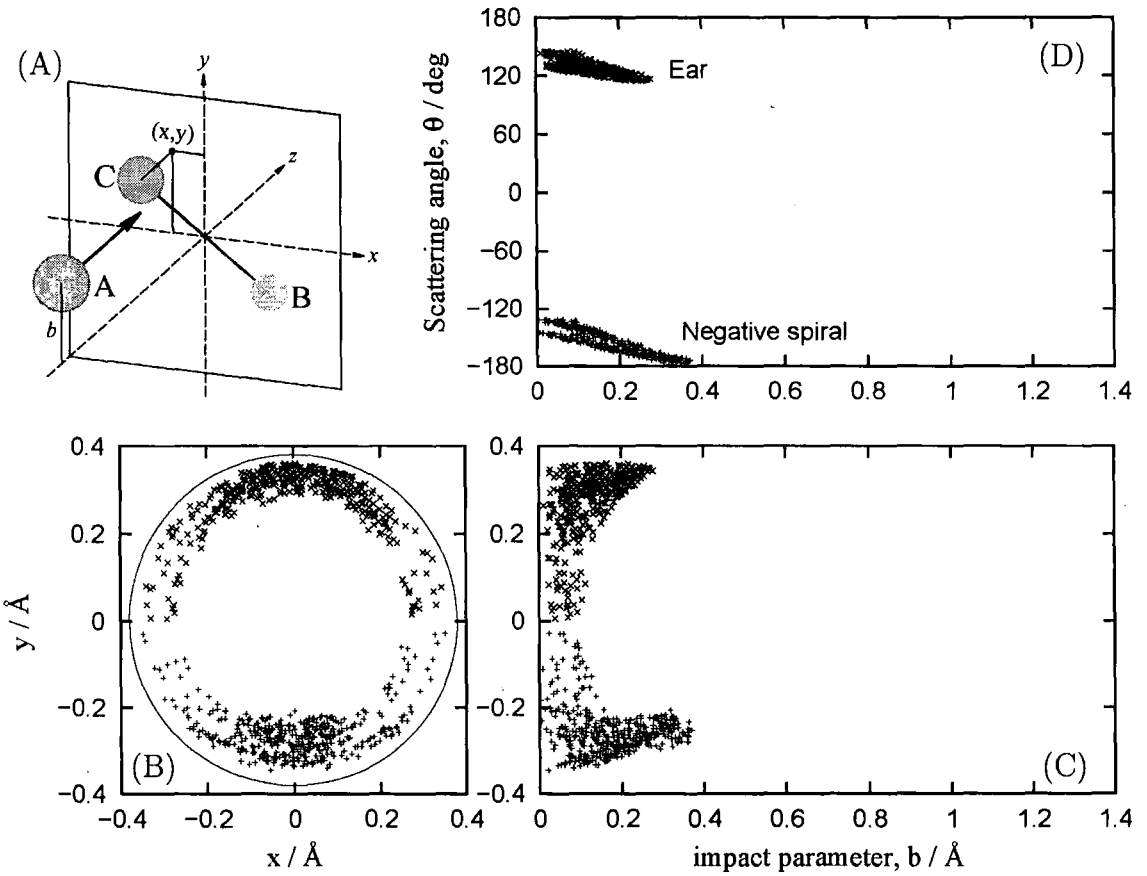

Figure 5.8: Plots showing the correlation between impact parameter, b, D_2 axis orientation and scattering angle, θ, for CIMeR trajectories in the HD($v' = 0$, $j' = 0 - 1$) state at E_{rel}=1.85 eV (*c.f.* Fig. 4.9). (A) Initial conditions for a trajectory: impact parameter, b, and location of the leading D atom projected onto the xy-plane, shown in panel (B). (C) Correlation between impact parameter and the initial y coordinate of the leading D atom. (D) Correlation between impact parameter and scattering angle. The Negative Spiral is shown to be the continuation of the CIMeR mechanism, with all trajectories having a side-on approach to the D_2.

Panel (A) of Fig. 5.8 shows the initial conditions for a trajectory: impact parameter, b, and location of the leading D atom projected onto the xy-plane. Panel (B) shows the orientation of the D_2 internuclear axis represented as a point relative to

the incoming z-axis. Using the polar orientation angle, Θ, the azimuthal orientation angle, ϕ, (see Fig. 3.2), and the equilibrium D_2 separation, R_e, the location of the leading deuterium atom is projected onto the xy-plane. R_e is used to make the orientation of the trajectories comparable. The circle in panel (B) has as its radius R_e, thus any trajectory at the circle represents a D_2 axis perpendicular to the z-axis. A collinear trajectory would be represented by a point at (0,0) in panel (B) with zero impact parameter in panel (C).

Fig. 5.8 demonstrates the side-on nature of the trajectories, which is in stark contrast to the case for the recoil/glancing mechanism seen for $v' = 3$ in Fig. 4.9. With the foremost deuterium in these positions, and a low impact parameter, the hydrogen will impact upon the conical intersection and be deflected onto the leading deuterium atom. It is clear to see that the Negative Spiral is the continuation of the CIMeR mechanism, with the conical intersection deflecting the hydrogen downwards towards the foremost deuterium in the lower hemisphere.

This correlation diagram clearly highlights the differences of orientation at impact between the v'=3 case, which is dominated by collinear collisions (see Fig. 4.8), and the v'=0 Ear case with its side-on collision. The end-on collision in the v'=3 case is a direct impact upon the hard wall (steep potential) at the head or tail of the D_2 molecule which is required to excite the v'=3 product state.

5.3 Positive Spiral (2D)

The Positive Spiral trajectories cover the full range of both the scattering angle and trajectory time, from the fast backwards scattering trajectories through to the slow forwards scattering trajectories.

Again, the initial conditions for these trajectories demonstrate (see Fig. 5.4) that a specific orientation of the system is required for spiral trajectories. As with the Ear trajectories the initial conditions for this group of trajectories are highly correlated (see Fig. 5.4), they are also correlated with the scattering angle. As the impact parameter increases and the initial polar angle, Θ, decreases, the scattering angle decreases becoming more forwards in character. Positive Spiral impact diagrams are shown for the range of scattering angles in Fig. 5.9. These diagrams also contain

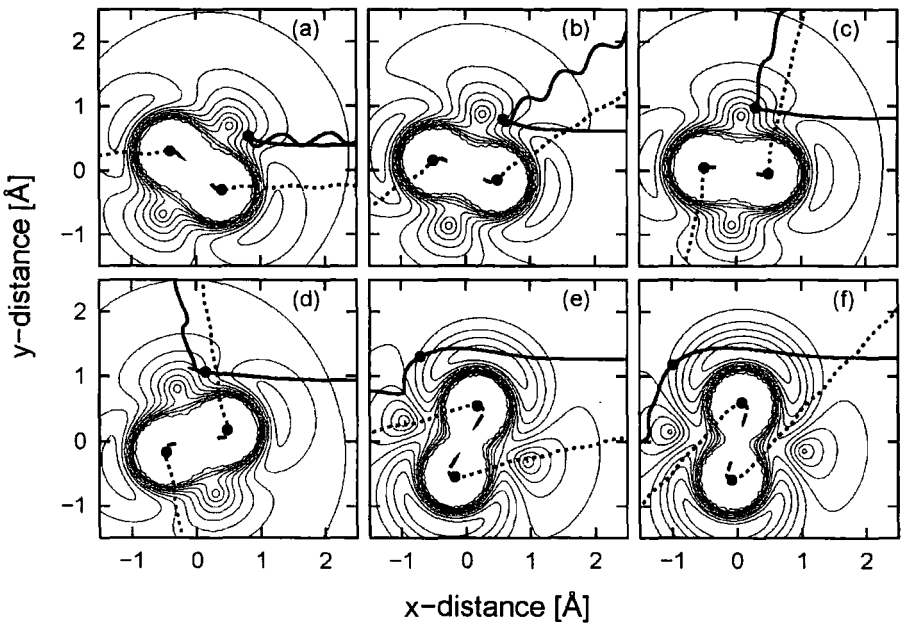

Figure 5.9: Impact diagrams (see Fig. 5.5) for the Spiral region. Scattering angles for the trajectories shown in frames (a) to (f) are, respectively: 179°, 146°, 104°, 81°, −11° and −46°.

information about the rotation of the HD_2 complex, the sharp bends in the motion of the D atoms (dotted lines) indicate the magnitude of the rotation of the complex.

5.3.1 Revolving Door Mechanism (2D)

All of the trajectories in the Positive Spiral impact on the conical intersection. The most forwards scattered trajectories display H atom impacts on the conical intersection on the 'far-side' of the D_2, as they are going away from the D_2, as shown in frames (e) and (f). The impacts for the Positive Spiral occur at larger D_2 separations than the Ear trajectories (see Fig. 5.5) when the conical intersection is more prominent.

It is this impact on the conical intersection that causes the Revolving Door Mechanism, which is clearly demonstrated in the movie sequence Fig. 5.10 and the following description.

0-15 fs The hydrogen approaches the D_2 molecule with a large impact parameter.

15-18 fs The D_2 bond stretches as the H atom flies past the end of the D_2.

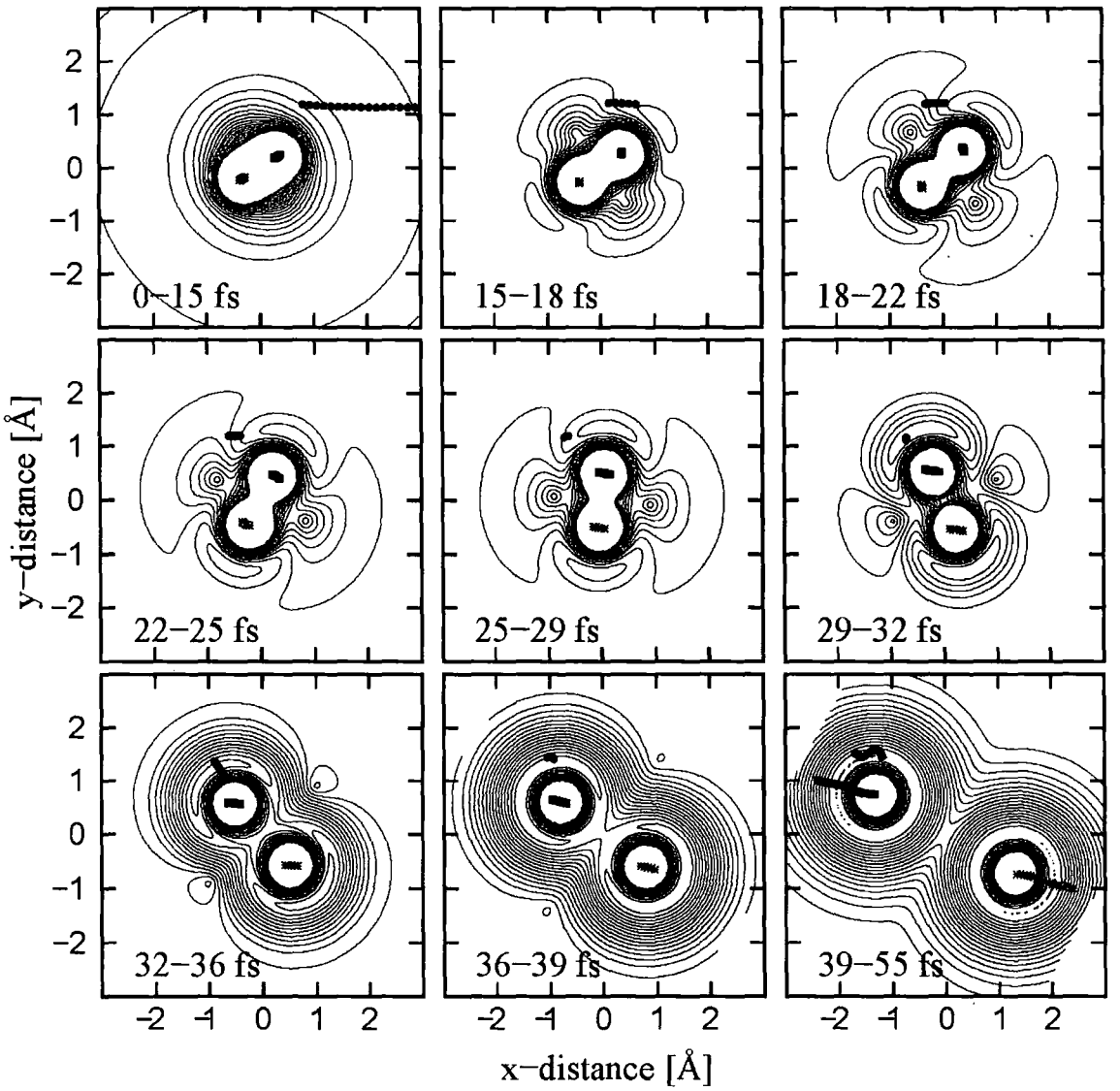

Figure 5.10: Reaction mechanism diagram for a typical trajectory in the positively scattered Spiral region of HD($v' = 0$, $j' = 0 - 1$) product state. The trajectory was restricted to two dimensions, in the yz-plane, at an energy of 1.85 eV.

18-22 fs The H atom is slowed by the increasing potential gradient at the conical intersection.

22-25 fs The H atom has transferred most of its translational energy to the D_2, via the 'lever arm' of the conical intersection, which starts to rotate about its centre-of-mass.

25-29 fs The continued rotation moves the linear well towards the almost stationary H atom, which starts to 'fall' into it.

29-32 fs This causes the D_2 bond to stretch even further, deepening the potential

well.

32-36 fs The H atom makes its first impact on the D atom at the inner turning point of the v'=0 vibration to set-up the product state.

36-39 fs The H atom is now trapped in the increasingly deep well as the D_2 bond breaks.

39-55 fs The HD + D products are formed and scatter.

The conical intersection acts as a lever to rotate the D_2 bond and in transferring its kinetic energy to the D_2 rotation the H atom is stopped and therefore able to impact upon the D atom when the D_2 rotation catches up with it.

The Revolving Door Mechanism was so named because of the similarity it shows to the probable outcome of running into a revolving door *i.e.* you stop on hitting one of the doors, but cause the door to rotate, then another of the doors hits you in the back and pushes you forwards.

For the HD product to be scattered forwards the D_2 has to rotate through a large angle and therefore requires a large impact parameter to give it maximum torque at impact. On going from forwards to backwards scattering around the spiral the amount of D_2 rotation required is diminished. The impact parameter decreases concertedly with the increasing scattering angle. These factors lead to a decrease in the torque exerted on the D_2 and therefore less rotation.

The longer times of the forward scattered trajectories are due to the longer distances travelled by the hydrogen before the first impact, and the D_2 rotation time. Backwards scattered trajectories have earlier impacts and require less rotation and consequently take less time. The trajectories that are scattered sideways with similar scattering angles to the Ear take longer times than the Ear trajectories because of the extra time required for the impact and rotation.

5.3.2 Revolving Door Mechanism in 3D

Because of the nature of the rotation required for the Revolving Door Mechanism it has to operate in a planar system. If the system was not planar then the D_2 rotation, caused by the impact of the H atom on the conical intersection, would not

result in the D atom hitting the H atom in such a way as to lead to HD($v' = 0$, $j' = 0-1$) products. The correlation diagram for three dimensional trajectories from the spiral region is shown in Fig. 5.11, where the CIMeR trajectories are overlaid for comparison.

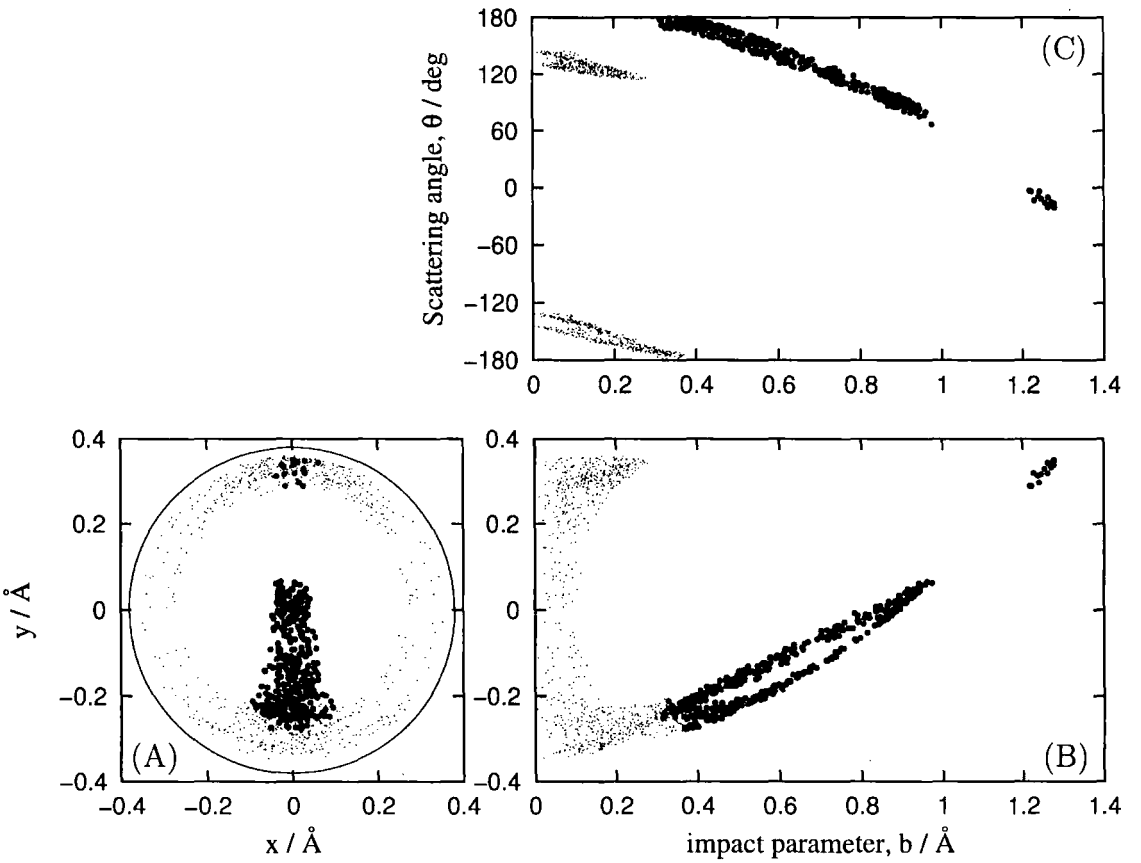

Figure 5.11: Plots showing the correlation between impact parameter, b, D_2 axis orientation and Scattering angle, θ, for Revolving Door trajectories in the HD($v' = 0$, $j' = 0 - 1$) state at E_{rel}=1.85 eV, *c.f.* Fig. 4.9. (A) Location of the leading D atom projected onto the xy-plane. (B) Correlation between impact parameter and the initial y-coordinate of the leading D atom. (C) Correlation between impact parameter and scattering angle. The CIMeR trajectories are overlaid (dots) for ease of comparison.

The planarity of the spiral is demonstrated by the clustering of the trajectories around the yz-plane. The system becomes less planar in the lower half of the diagram as it overlaps with the D_2 axis orientation used by the Negative Spiral. The overlap at the top of the diagram is not due to a similar effect, as the Ear trajectories at that point have low impact parameters and the Spiral trajectories have large impact parameters, and consequently do not impact at the same point. Fig. 5.11 also shows the strong correlation between impact parameter and scattering angle.

The collision on the conical intersection slows the motion of the hydrogen allowing it to match speeds with, and impact upon, the deuterium at the inner turning point of the v'=0 vibration, allowing excitation into this product state. This leads to the conclusion that the Revolving Door mechanism, like the CIMeR mechanism, is a way of dissipating excess collision energy to allow access to lower vibrational states.

5.4 Sickle (2D)

The Sickle trajectories scatter in the forwards direction and have the largest total times of the three regions in the snapshots, but the trajectory time shows no dependence on scattering angle as it did for the Spiral, see Fig. 5.3. The initial conditions are also less correlated than for the Ear or Spiral, with no discernible dependences, apart from requiring a relatively large impact parameter, see Fig. 5.4.

Fig. 5.12 shows impact diagrams and RR plots for trajectories over the range of scattering angles covered by the Sickle. The upper panels show impact diagrams *c.f.* Fig. 4.6. The lower panels show the trajectories in the product and reactant channels of the PES (see Fig. 2.1) at the bending angle at impact. These RR plots (see Section 4.3.3) show the interaction region as a dashed line box in the lower left hand corner, and the barrier is the diagonal dashed line. Motion of the hydrogen atom along or parallel to this line indicates a symmetrical stretching of the atoms.

It is important to note that none of the impacts shows any interaction with the conical intersection, therefore the excess energy is dissipated by other mechanisms. Frames (a) and (b) of Fig. 5.12 show a different type of mechanism to the other frames, which will be described first before a more in-depth discussion of the mechanism that is in evidence in frames (c), (d), (e) and (f).

The trajectories in frames (a) and (b) have impact parameters so large that the H atom initially misses the D_2 molecule, it only receives a small deflection from the outer section of the PES. As the H atom goes past the linear configuration with the D_2 the deuterium bond expands forming the linear well. The H atom runs around the outside edge/wall of the well, and because the well is still deepening due to D_2 bond stretch the H atom cannot leave. After the H atom has moved up the

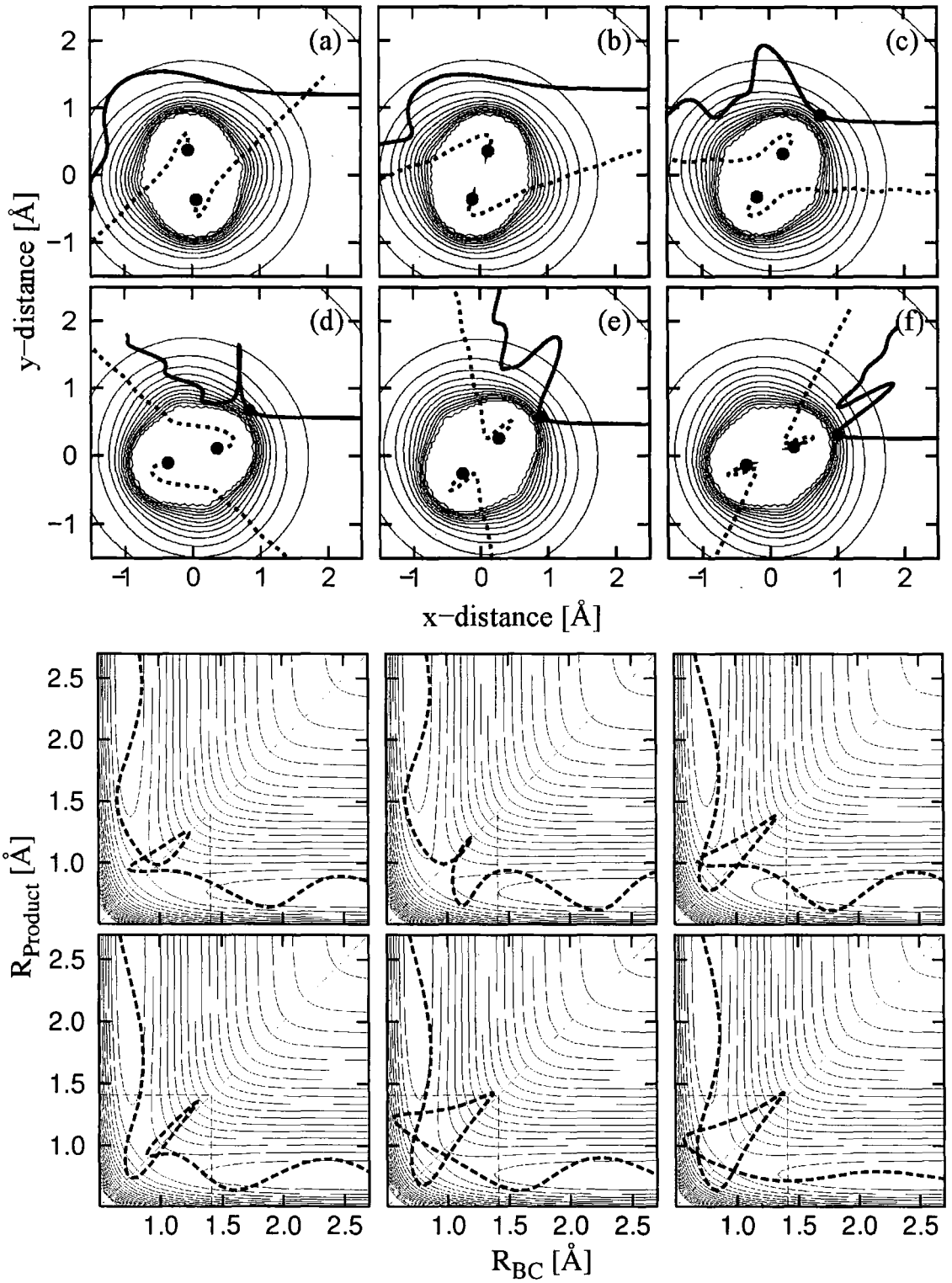

Figure 5.12: Top: Impact diagrams (*c.f.* Fig. 5.5) for the Sickle region. Scattering angles of the trajectories shown in frames (a) to (f) are respectively –48°, –21°, 1°, 42°, 79° and 118°. Bottom: RR plots for the same trajectories; Reactant *vs.* product bond lengths; trajectories start from the top left-hand side of the plot (R_{BC} small), the interaction region is represented by the dashed line box in the lower left hand corner. See text for details.

outside wall of the well (the outer turning point of the v'=0 vibration) it reverses its motion and is directed towards the deuterium atom. The H atom forms the product molecule during its collision with the D atom at the inner turning point of the v'=0 vibration. Because of the initial passage of the hydrogen past the D_2 this mechanism has been dubbed the Slingshot mechanism. This mechanism *could* be seen as a progression of the Revolving door. If the trends seen in Fig. 5.9 continued, the impact parameter would increase and the D_2 would become more perpendicular, and you would see frames (a) and (b) of Fig. 5.12. Due to the relatively low number of these trajectories this was hard to determine conclusively.

The mechanism responsible for the reactive scattering in frames c, d, e and f is shown in the movie sequence Fig. 5.13 and the following description.

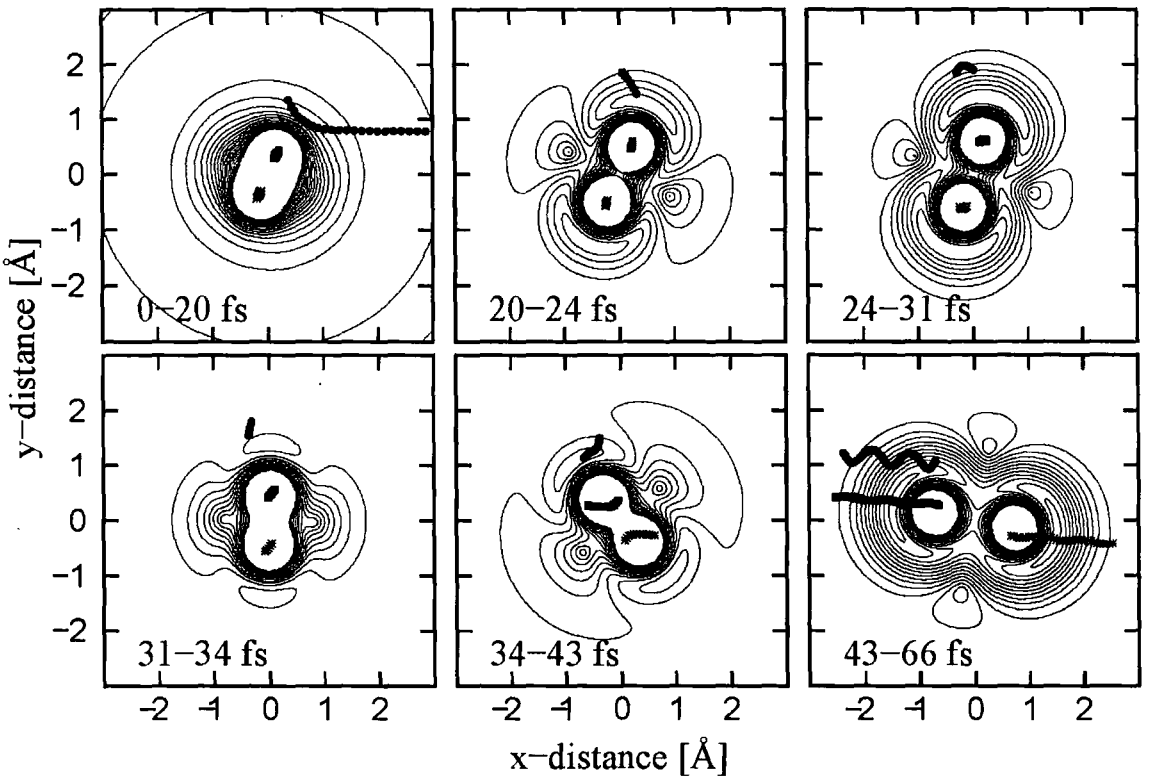

Figure 5.13: Reaction mechanism diagram for a typical trajectory in the Sickle region of the HD($v' = 0$, $j' = 0 - 1$) product state. The trajectory was restricted to two dimensions, in the yz-plane, at an energy of 1.85 eV.

0-20 fs The H atom approaches the D_2 from the side with a large impact parameter and has a hard impact with the end of the deuterium.

20-24 fs The H begins to leave the interaction region, but its presence has caused

the D_2 bond to expand.

24-31 fs The bond expansion causes the linear potential well to open up behind the H atom preventing it from leaving. The momentum of the H atom is transferred to the rotation of the D_2 by collision with the outer wall of the well.

31-34 fs The D_2 bond contracts during the rotation, as the H atom heads towards the deuterium.

34-43 fs The H atom collides for the second time on the deuterium atom and the D_2 bond expands.

43-66 fs The D_2 bond expands and breaks as the products are formed.

The rotational part of the mechanism occurs later in this scheme when compared with the Revolving door mechanism. The amount of rotation has no effect on the time of the trajectory in contrast to the Revolving door mechanism.

The Sickle in 3D

As with the two dimensional case the initial orientation of the three dimensional trajectories shows less prominent correlations, as can be seen in Fig. 5.14, apart from the need for large impact parameters and perpendicular D_2 axis orientation. Sickle trajectories display a short term reaction intermediate which undergoes symmetric stretching motions, as highlighted by the complex behaviour in the interaction region of the RR plots in Fig. 5.12 (Motion of the hydrogen atom along or parallel to the diagonal dashed line indicates a symmetrical stretching of the atoms). As such they behave in a very similar way to the long time delayed trajectories found in the v'=3 case (see section 4.4.3). Sickle trajectories seem to be responsible for the time delayed forward scattering seen in frame 40 fs of Fig. 5.1. Further analysis of the sickle was prevented by the small number of trajectories in the region.

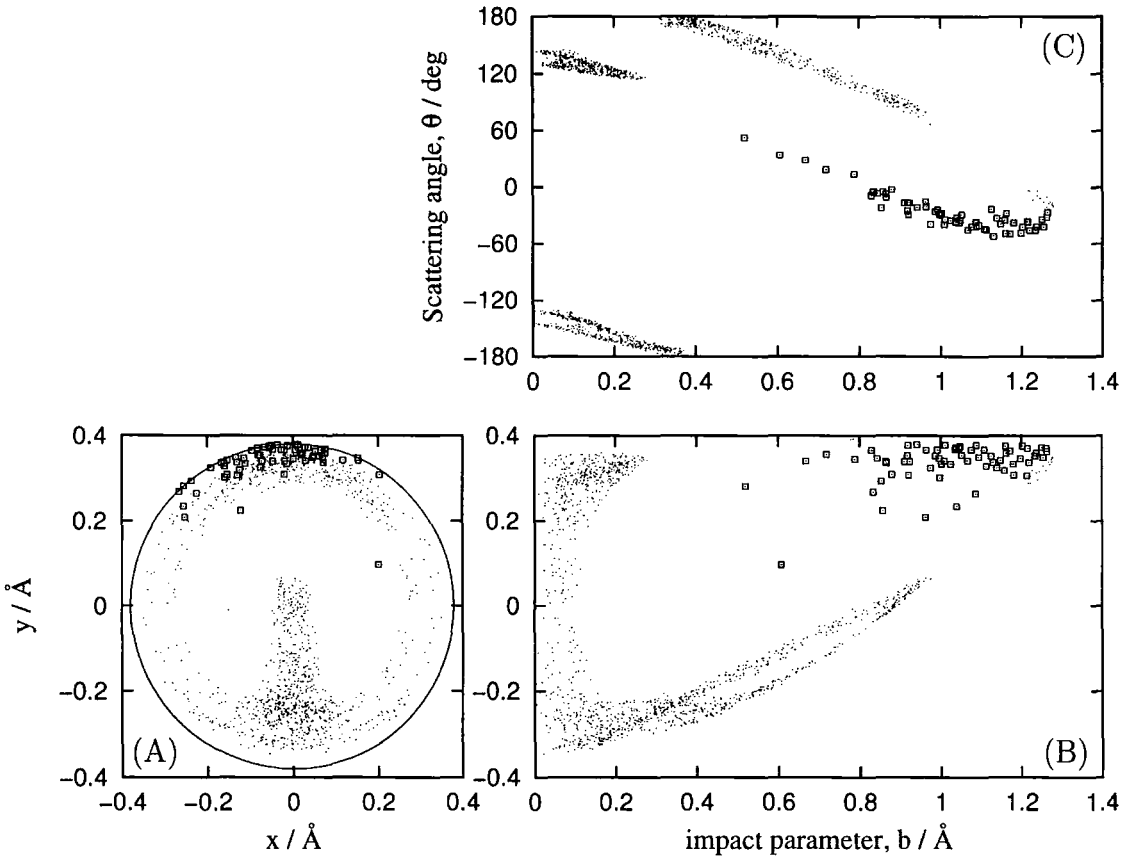

Figure 5.14: Plots showing the correlation between impact parameter, b, D_2 axis orientation and Scattering angle, θ, for Sickle trajectories in the HD($v' = 0$, $j' = 0 - 1$) state at E_{rel}=1.85 eV, *c.f.* Fig. 4.9. The relationship between the initial conditions is less correlated than for the CIMeR or revolving door mechanisms.

5.5 v'=0 Summary

To illustrate the relative significance of the new mechanisms described above, the cross sections of each mechanism are compared with the total scattered flux for the HD($v' = 0$, $j' = 0 - 1$) product state in Fig. 5.15. The cross sections were calculated using Eqn. 4.4 and the procedure described in Section 4.4.3. The results for 5 million 3-dimensional trajectories carried out at an E_{rel} of 1.85 eV were used for the calculations.

The differential cross section (see Fig. 5.15) clearly shows that the majority (74%) of scattered HD($v' = 0$, $j' = 0 - 1$) flux arises from the CIMeR mechanism. These trajectories are the most direct seen at this energy leading to these quantum states. The Revolving Door corresponds to 21% of the total HD($v' = 0$, $j' = 0 - 1$)) scattering, and is therefore statistically significant. The Sickle trajectories only

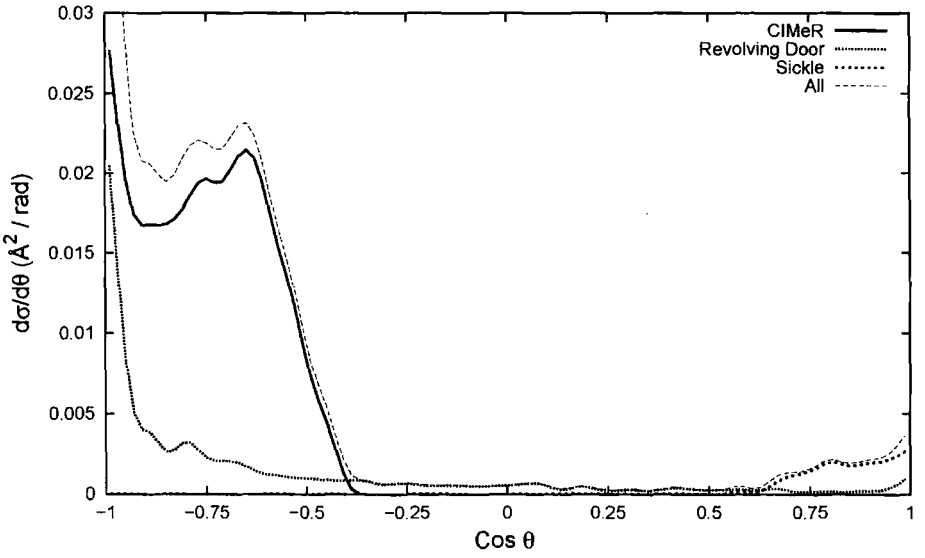

Figure 5.15: Cross section of the new mechanisms in the H + $D_2(v'=0, j'=0) \rightarrow$ $HD(v'=0, j'=0-1)$ + D reaction at a collision energy of 1.85 eV as a function of scattering angle, showing the dominance of the CIMeR mechanism.

correspond to 5% of the classical scattering, but may be more significant in the QM picture.

The dominance of the CIMeR and Revolving Door mechanisms demonstrates the importance of the conical intersection in reaction dynamics.

The end-on collisions seen in the v'=3 case are direct impacts upon the hard wall (steep potential) at the head or tail of the D_2 molecule to give the inner turning point of the $HD(v'=3)$ vibration. These hard impacts are not found in the v'=0 case. The CIMeR and Revolving Door mechanisms use the conical intersection to dissipate excess kinetic energy and match the speeds of the product atoms so that the first impact upon the D atom is at the inner turning point of the v'=0 vibration.

Comparison with HD($v'=0, j'=0$) QM snapshots

The QM snapshots, Fig. 5.1, result from a range of collision energies, 0.4–2.5 eV, and so contain low energy trajectories which proceed via the recoil mechanism, as well as high energy trajectories that require the CIMeR and Revolving Door mechanisms to dissipate excess energy. Thus a large amount of direct recoil flux can be seen in the backwards scattering region. In contrast the QCT snapshots, Fig. 5.2, have a collision energy of 1.85 eV and require the CIMeR and Revolving Door mechanisms

exclusively to access the v'=0 product state. By comparing the two figures it can be seen that the two sideways scattering wings in the QM snapshots are due to CIMeR and Revolving Door mechanisms. The gap between the backwards and sideways scattering flux in the QM picture could be described as an interference between the direct recoil and CIMeR/Revolving Door mechanisms.

The forwards scattering in the v'=0 QM snapshots shows similar glory scattering to that in the v'=3 QM snapshots in Fig. 4.1. By comparing the v'=0 QCT snapshots, Fig. 5.2, with the v'=0 QM snapshots, Fig. 5.1, it can easily be seen that the forwards scattering is described by the sickle trajectories, again reinforcing the similarity these trajectories have to the forwards scattered v'=3 products.

5.6 Importance of the Conical Intersection

The importance of the conical intersection to the mechanisms of the hydrogen exchange reaction leading to the HD($v' = 0$, $j' = 0 - 1$) product states has been shown in the previous section. These product states only account for 1% of the reactive scattering at 1.85 eV. Initial two dimensional analysis of the higher j' states of HD($v' = 0$) shows a continuation of the CIMeR and Revolving Door mechanisms. The full three dimensional picture of these states is considerably more complex and would require an exorbitant effort to examine the reaction mechanisms state-by-state. To assess the significance of these new mechanisms a series of criteria for all reactive trajectories were developed to discern the proportion which involve interaction with the conical intersection.

The distance from the H atom to the conical intersection, R_{CI}, was monitored during each trajectory, along with the product bond length, R_{AB} and bending angle, α. The first minimum in each of these coordinates, as well as the time at which it occurred, was recorded. These data points were then tested by a series of geometrical considerations to assign reaction mechanisms.

Trajectories which undergo a hard collinear impact (*e.g.* the v'=3 case), and therefore do not have any possible interaction with the conical intersection, were identified to simplify the subsequent analysis. A trajectory was deemed to be of the hard collinear impact type if the distance of the first close approach of the H

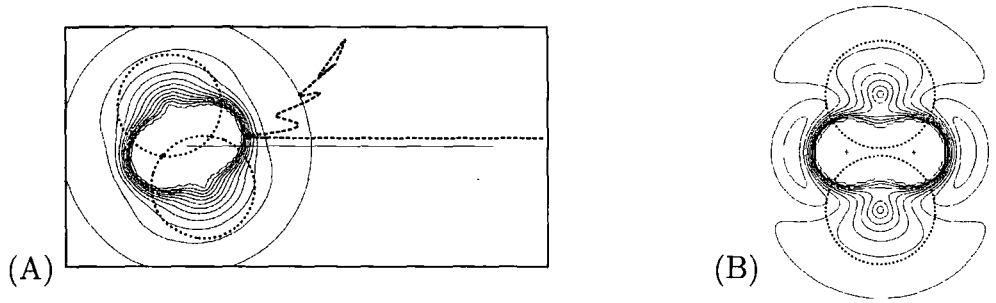

Figure 5.16: (A) Impact diagram, *c.f.* Fig. 4.6, demonstrating the criterion for the assignment of the hard impact mechanism. The dashed circles have a radius of the D_2 separation, q, around the conical intersection. (B) The PES with a larger D_2 separation, the dashed circles have the radius of the outer turning point of the reactant vibration, 0.858474 Å.

atom to the CI was greater than the D_2 separation, q, at that point. This criterion is demonstrated in panel (A) of Fig. 5.16 in which circles of radius q at closest approach are drawn. It is clearly seen that this hard impact, direct recoil trajectory does not enter the circles.

A similar argument can be made for trajectories which do not pass within 0.858474 Å (the outer turning point of the reactant vibration) of the CI. As can be seen in panel (B) of Fig. 5.16 trajectories that do not pass through the circle can be considered to have no interaction with the conical intersection, and are called 'case 2' trajectories.

The trajectories that did not conform to the previous two criteria were then further subdivided using temporal and spatial arguments. Fig. 5.17 shows how the reactant and product internuclear distances, as well as the distance of the hydrogen atom to the CI, change with time for four trajectories with different degrees of interaction with the conical intersection. The thin dotted line in this figure represents the 0.858474 Å limit of the outer turning point of the reactant vibration discussed above.

The degree of interaction with the conical intersection a trajectory experiences can be described by the following generalised criteria (used for all trajectories):

Hits CI The minimum in R_{CI} is smaller and happens before the first minimum in the R_{AB} coordinate; the H atoms hit the CI and this interaction was crucial

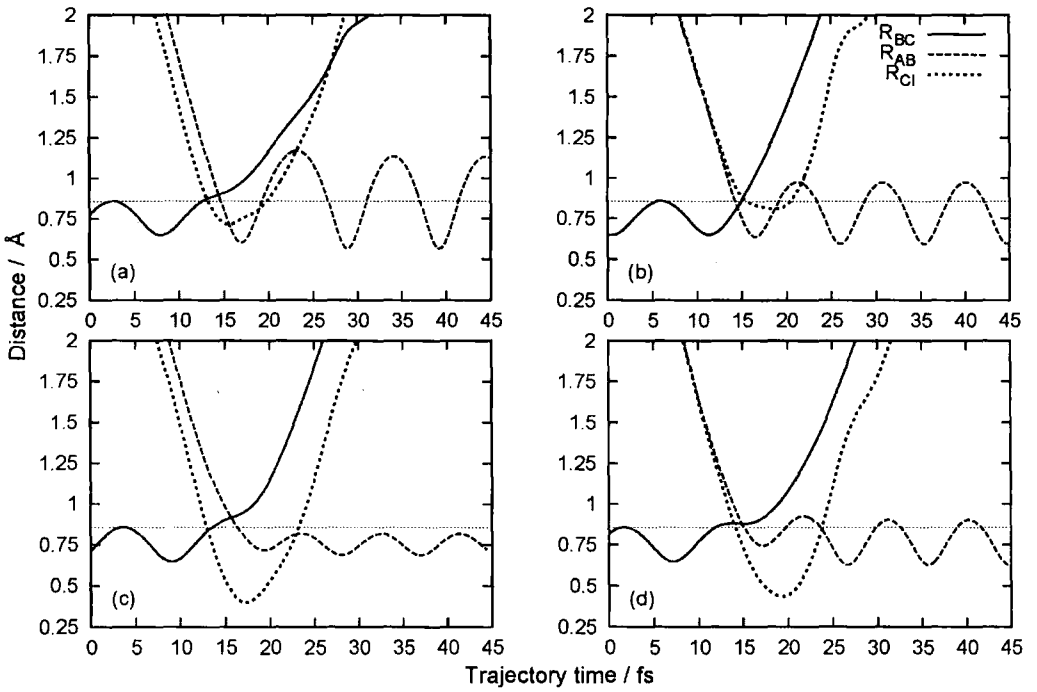

Figure 5.17: Distance from the H atom to the conical intersection, R_{CI}, compared to bond lengths R_{AB} and R_{BC} plotted as a function of time for trajectories with different degrees of interaction with the conical intersection (see text). The plot also shows the 0.858474 Å threshold, thin dotted line (see text).

to the products forming. An example is shown in panel (c) of Fig. 5.17. These trajectories involve CIMeR and revolving door mechanisms.

Non-decisive interaction with the CI The minimum in R_{CI} is larger and happens later than the first minimum in the R_{AB} coordinate; the interaction with the conical intersection, if any, is not decisive and as such these trajectories are also labelled 'case 2' trajectories. An example is shown in panel (b) of Fig. 5.17.

Probable decisive interaction with the CI The minimum in R_{CI} is smaller but happens later than the first minimum in the R_{AB} coordinate; this can occur if the hydrogen flies past the end of the D_2 on its way to hit the conical intersection. An example is shown in panel (d) of Fig. 5.17, note that the approach to the CI is as close as in the **hits CI** case, panel (c).

Possible decisive interaction with the CI The minimum in R_{CI} is larger but happens before the first minimum in the R_{AB} coordinate; this can indicate a

CIMeR type mechanism where the potential around the conical intersection deflects the H atom towards a close impact with D_2. An example is shown in panel (a) of Fig. 5.17.

Dividing the results from the 5 million trajectories run at 1.85 eV (see table B.4 for the quantum state distribution) according to the above criteria yielded the following initial results: 28 % of reactive trajectories undergo hard end-on collisions leading to the direct recoil mechanism. 16 % are 'case 2' trajectories and do not interact with the CI during the reaction, but are currently unassignable. 28 % hit the CI (and probabally undergo a revolving door or CIMeR mechanism). 28 % interact with the CI during the reaction in a less well defined way, these trajectories can be involved in insertion mechanisms, but a quantitative analysis was not conducted due to time constraints.

The importance of the conical intersection at this collision energy (affecting up to 56 % of reactive trajectories) has been shown.

Chapter 6

Conclusions

6.1 Conclusions

Results from a QCT study into the hydrogen exchange reaction for the H + D_2 isotopic variant have been presented. The results were compared with recent quantum mechanical (QM) calculations [1] and used to elucidate reaction mechanisms in the HD($v' = 0$, $j' = 0 - 1$) and HD($v' = 3$, $j' = 0 - 1$) product states.

v'=3 Conclusion

QCT calculations have been demonstrated to be a good match for the temporal and spatial trends in the contours of the QM snapshots (see Fig. 4.1), including the time delay between forwards and backwards scattering. However, the separation between forwards and backwards scattering, or the quantum effects such as glory scattering were not observed. It is proposed that both of these quantum effects can be justified as interferences between two independent classical trajectories that lead to the same scattering angle [8]. The glory scattering derives from the time delayed trajectories moving around the interaction region from sideways to forwards scattering angles and interfering in the forwards region. The separation between forwards and backwards scattering in the QM picture could be seen as an interference between the fast (recoil/glancing) trajectories that scatter sideways and the multiple stretching (trapped) trajectories that scatter into the same region. This effect would be more pronounced if the population of trapped trajectories was enhanced due to

a resonance effect.

The dominant mechanism progresses from hard collinear impacts to glancing impacts, where the increased time for the sideways and forward scattered trajectories is due to the rotation of the HDD complex and extra distance travelled. This mechanism derives from the strong correlations between the initial conditions of D_2 axis orientation and impact parameter and the scattering angle.

The v'=3 product state is excited by hard impacts at the inner turning point of the $v' = 3$ vibration, or by glancing impacts that excite through the outer turning point of the $v' = 3$ vibration.

It has been suggested that a glancing attack mechanism would have to convert energy initially concentrated in the HDD bend into energy along the HDD asymmetric stretch, to allow the system to pass over the transition state and react [1]. If the energy was initially converted into a symmetric stretch then the HDD complex would be 'trapped' in the transition state for the period of that stretch.

This study has shown that forward scattered trajectories display a significant amount of symmetric stretch vibrations of the HD_2 complex. Moreover, the forward scattering mechanism requires the system to undergo these stretching motions. A significant number of trajectories undergo multiple stretches, and some even show longer term excitation as have been previously observed by Muga and Levine [57].

This excitation of transition state vibrations indicates the presence of a scattering resonance. QCT cannot detect resonances or quantum bottleneck states (QBS), but the symmetric stretches and bends described here for the forwards scattered trajectories are consistent with the complex motions predicted for both resonances [19, 67] and QBS [38, 39].

v'=0 Conclusion

The mechanisms responsible for scattering into the HD($v' = 0$, $j' = 0$) product state are not of the hard impact or glancing type observed for v'=3. Although the sickle trajectories display the same type of complex motion as the time delayed forwards scattered trajectories in the v'=3 case. There are at least two new reaction mechanisms present in the v'=0 quantum state that do not rely in any way upon direct recoil.

The CIMeR mechanism, in which the hydrogen 'slides off' the conical intersection (CI) to form products with the foremost deuterium atom, is dominant accounting for 74% of reactive trajectories leading to these low j' product states. The Revolving Door Mechanism, in which the CI is used as a lever to cause rotation of the D_2 before scattering to a wide range of angles, corresponds to 21% of these reactive trajectories (see Fig. 5.15).

The CIMeR and Revolving Door mechanisms use the conical intersection to dissipate excess energy and match the speeds of the product atoms so that the first impact upon the D atom is at the inner turning point of the v'=0 vibration. This is in contrast to the end-on collisions seen in the v'=3 case where direct impacts upon the hard wall (steep potential) at the head or tail of the D_2 molecule give the inner turning point of the HD(v'=3) vibration.

The dominance of the CIMeR and Revolving Door mechanisms demonstrates the importance of the CI in reaction dynamics.

Importance of the Conical Intersection

To assess the significance of the new mechanisms to the total reactive scattering a series of criteria have been developed to discern the proportion of trajectories that interact with the conical intersection during a reaction.

Initial studies of trajectories at a collision energy of 1.85 eV have shown that:
28 % of reactive trajectories undergo hard end-on collisions leading to the direct recoil mechanism.
16 % do not interact with the CI during the reaction, and are currently unassignable.
28 % hit the CI (and probabally undergo a revolving door or CIMeR mechanism).
28 % interact with the CI during the reaction in a less well defined way, these trajectories can be involved in insertion. Many new ideas for these mechanistic criteria came about during the preparation of this thesis, but due to time constraints they could not be quantitatively investigated.

The importance of the conical intersection at this collision energy (affecting up to 56 % of reactive trajectories) has been demonstrated. These are initial results from an ongoing study of the hydrogen exchange reaction mechanisms.

QCT

The quasi-classical trajectory method has been shown to give valuable insight into the simplest chemical reaction. By examining individual quantum states, finding correlations between initial conditions, and using simplified reaction systems, reaction mechanisms have been discerned. This method has the ability to graphically demonstrate the reaction mechanisms that can lead to interference phenomena in QM calculations.

6.2 Future Work

Further work on the H + D_2 system would include refining the criteria for the assignment of mechanisms to reactive trajectories. Determining the energy dependence of the (new) mechanisms would confirm the hypothesis that they are a way of dissipating excess collision energy to allow access to lower vibrational states at high collision energies.

Further comparison with quantum snapshots may be able to confirm the presence of the new mechanisms and help to explain quantum interference effects.

The hydrogen exchange reaction is now so well understood that further work is currently unforeseeable without surprising experimental or theoretical results. For example if QM scattering calculations on the new CCI PES display new and unexpected features that are difficult to explain, the QCT methodology described here could be used. Likewise if experimental studies discover unexpected new scattering features for H + D_2 or any other isotopic variant this QCT methodology can be used.

Another possible area for future study is the contribution of the geometric phase effect [78, 79] to reactive scattering in the hydrogen exchange reaction. The QCT methodology presented here could be used to help understanding of how this effect comes about.

The QCT methodology described here could also be applied to other three and even four body reactive systems, especially if there are QM and highly resolved experimental results available for comparison. An initial system of interest is F + HD → HF + D, where a resonance has been observed causing state-specific forward

scattering of product molecules [68]. QCT could be used to investigate the dynamics of this resonance.

Part II

UV Cavity Ring-Down Spectroscopy of BPEB

Chapter 7

Motivation and Method

7.1 Molecular Wires and Switches

7.1.1 Introduction

The increasing demand for computational power is being met by efforts to miniaturise the basic devices on a microchip. For the past 40 years the number of transistors that can be fabricated on a silicon integrated circuit - and therefore the computing speed of such a circuit - has been doubling every 18–24 months, a phenomenon known as Moore's law [80]. Components are now so small the challenges of the quantum effects such as tunnelling, diffraction and interference of electrons, are threatening to halt further miniaturisation of components and hence invalidate Moore's law.

One possible solution lies in the field of molecular electronics which attempts to fabricate logical circuits at the single molecule level, such molecules not being subject to the quantum effects mentioned above. Molecules are required that can perform functions identical or analogous to those of the transistors, diodes and other key components of today's microcircuits. Molecules which display negative differential resistance (NDR) behaviour have numerous device applications and can give rise to novel compact circuits [81]. In a typical semiconductor device, current tends to rise with increasing voltage, but there is a region between the peak voltage and valley voltage where the the current falls as the voltage is increased. This is the negative differential resistance (NDR) region. In this voltage range the differential

resistance is less than zero. The peak voltage is often called the threshold voltage since it represents a threshold beyond which is the negative resistance region. Several studies have demonstrated possible candidates for molecular wires, switches, diodes and systems which demonstrate NDR (see Refs. [81, 82, 83, 84, 85, 86] and references therein).

One class of compound showing promise in this area is oligomeric materials with conjugated π-electron systems, such as polythiophenes [87, 88, 89] or ethynylated aromatic systems such as poly(phenyleneethynylene)s (PPE) and their derivatives.

Poly(phenyleneethynylene)s

PPE's (see Fig. 7.1) have interesting electronic characteristics, and along with their derivatives, have been studied as possible candidates for molecular wires, switches and diodes. Experiments have been conducted which show these molecules and their

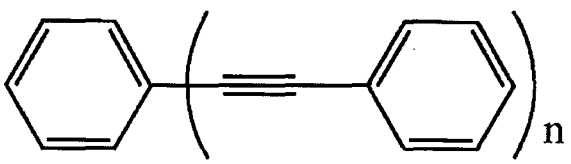

Figure 7.1: Poly(phenyleneethynylene).

derivatives exhibiting NDR, bistable conductance states (memory), and controlled switching under an applied electric field [81, 82, 83, 84, 85, 86].

Two different types of switching experiment that have been demonstrated are:
(i) measurements are made with a scanning tunnelling microscope (STM); of either a self assembled monolayer (SAM) of the molecule of interest chemisorbed on a gold surface [86], or of a silicon nanopore with the molecule of interest sandwiched between a gold surface and a small gold contact [81].
(ii) the molecule of interest forms a SAM on two facing gold electrodes of a break junction allowing for direct observation of charge transport [86]. It is important to point out that the results of these switching studies may not be as straight forward as they seem. For example it has been suggested [90] that some experiments may be probing a different phenomena, namely pulling monoatomic gold wires from the gold surface on which the molecules are chemisorbed.

Theoretical and experimental studies of the mechanism behind the NDR and switching results have postulated two possible causes of switching: (i) due to a two step reduction process, in the first step the molecule undergoes a one electron reduction, turning on the conduction channel; then a second electron reduction causes the blocking of the current [91]. (ii) conformational changes in the molecules, specifically the relative intramolecular orientation of the aromatic rings, brings about a disruption in the conjugation of the molecule [86]. This second cause can be justified by looking at the model used to describe conductance in these molecules; the highest valence and lowest conduction bands (highest occupied molecular orbital (HOMO) and lowest unoccupied molecular orbital (LUMO)) are based on carbon π-orbitals (on both the phenyl ring and the triple bond carbons) that are perpendicular to the plane of the phenyl rings. These π-orbitals must be delocalised across the whole molecule to allow conductance through it. When the aromatic rings are twisted relative to each other, the alignment of the ring π-orbitals is destroyed (the orbitals are localised on individual rings) and therefore can no longer be used to transport electrons [92].

Another potential use for this class of compound arises from consideration of the molecular orbitals (MO's), namely as emitting layers in electroluminescent devices. The photo- and electroluminescent properties are dependent upon the HOMO-LUMO gap which varies with the effective conjugation length.

> "To engineer molecular devices based upon conjugated frameworks, a firm grasp of the factors that control the geometry of the compound, and hence the π-conjugation pathway, in both the ground and excited states is required" [93].

Tolane

The smallest PPE, Tolane ($n = 1$), was used in a nanopore switching experiment [84] where it was concluded that the conductivity was dependent upon the relative twist angle between the two benzene rings. Greater understanding of this twisting motion will elucidate the degree of π-conjugation and allow molecules to be designed that are able to control switching.

Ring twisting in Tolane has been studied by Okuyama *et al.* [94, 95], who obtained the ground and excited state ring twisting potentials from fluorescence spectroscopy.

The excited states of PPE's are not well modelled by Tolane, whose S_1 and S_2 excited states are very similar in energy [95, 96]. The S_1 and S_2 states have markedly different structures, with the higher state having a linear acetylenic type structure, and the lower state a bent conformation with a substantially weakened C≡C link [96].

7.1.2 1, 4-bis(phenylethynyl)benzene (BPEB)

In contrast 1, 4-bis(phenylethynyl)benzene (BPEB, the $n = 2$ PPE, see Fig. 7.2) behaves in a manner similar to the higher oligomers of PPE, its excited states do not show any substantial change in structure, and is therefore chosen as a model system to study the behaviour of this family of materials.

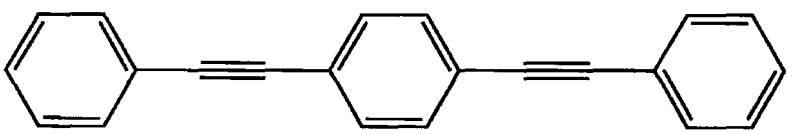

Figure 7.2: 1, 4-Bis(phenylethynyl)benzene.

Switching Studies

BPEB is used as a backbone, and comparator, in switching experiments [81, 85, 86, 91]. The molecules 2'-amino-4,4'-di(ethynylphenyl)-5'nitro-1-benzenethiol and 4,4'-di(ethynylphenyl)-2'nitro-1-benzenethiol (see Fig. 7.3) have gained much attention recently as single molecule switches that display NDR behaviour [81, 85, 86, 91, 97]. These substituted phenylene ethynylene oligomers have often been compared with BPEB, which does not display the NDR behaviour, to gain an insight into the mechanism behind NDR in these molecules. Whilst BPEB does not display NDR it does exhibit stochastic conductance switching when inserted into SAM dodecanethiol films [86].

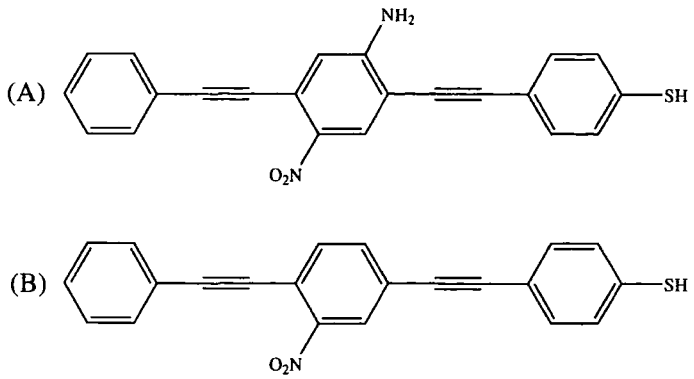

Figure 7.3: Molecules used in switching studies, (A) 2'-amino-4,4'-di(ethynylphenyl)-5'nitro-1-benzenethiol. (B) 4,4'-di(ethynylphenyl)-2'nitro-1-benzenethiol.

Theoretical Studies

Theoretical switching studies have been conducted examining the two possible mechanisms for NDR and switching. Many of these studies have looked at the frontier orbitals of BPEB and its derivatives, in both the twisted and planar configurations. These MO pictures show the π-orbitals to be delocalised across the whole molecule in the planar configuration and isolated on the central ring in the twisted configuration [91, 98]. The different methodologies used for these calculations appear to have very little effect upon the MO picture, but the energies of the orbitals are markedly different [98]. The effect of charge on the frontier orbitals has been examined to justify the charge switching explanation of NDR [91]. The effect terminal sulphur atoms (used to bind the molecules to the gold surfaces in experimental studies) have on the MO's has also been studied [99]. It has been shown that there is a 500 times change in conductance on rotation of the middle ring, from planar to perpendicular, of BPEB [92].

When rotation of the rings has been discussed only a twist of the central ring is generally considered. Some have tried to estimate the energy dependence of twisting the middle ring [98] or independently twisting the end rings of 2'-amino-4,4'-di(ethynylphenyl)-5'nitro-1-benzenethiol [97]. A recent paper has used a lumped-inertia technique to analyse the frequencies of the torsional modes of PPE's up to n = 5 [100]. The calculated value for the Tolane torsion, 16 cm^{-1} is in good agreement with the experimental value of 17 cm^{-1} [94], the predicted values for the two BPEB torsional frequencies are 13.2 and 19.4 cm^{-1}. It was found that

force constants used for the twist of adjacent rings were invariant with the length of the PPE, n, but the force constants for longer range interactions (next nearest neighbour) increased with n, highlighting the effect of the extended conjugation system.

The internal vibrations of BPEB have been predicted using a "building block" scheme. The normal modes are predicted using a building block (Tolane) and group theory considerations. This methodology has predicted a vibrational frequency for the ring torsion of BPEB of 8 cm^{-1}, which could not be confirmed by IR or Raman spectroscopy [101].

Spectroscopy of BPEB

Solution phase spectroscopy has been carried out by groups with interests in BPEB, and its derivatives, as a potential emitting layer in electroluminescent devices [93, 98, 102]. Absorption spectra show a series of partially resolved absorption bands between 250 and 350 nm, with a sharp band edge at the red end of the absorption profile. Fluorescence emission spectra indicate that BPEB behaves in a conventional manner at room temperature, displaying a continuum of rotational conformers in solution. However in a viscous low temperature glass it indicates a slow relaxation of rotamers of the excited states compared to the rate of fluorescence [93].

A time-resolved fluorescence examination of BPEB showed that subtle changes in the emission spectra less than 50 ps after excitation are due to the reorientation to the lowest energy torsional levels of the S_1 state, which has a more static molecular geometry than the ground state [102]. This observation was supported by resonance/non-resonance Raman spectroscopic results, which also showed that the acetylenic bond still had triple bond order in the excited state *i.e.* no evidence was found for any significant cumulenic/quinoidal character in the S_1 state.

Whilst these results give a valuable insight into the character of the excited state of BPEB, they are unable to provide detailed information about the important torsional motion of the molecule in either the ground or excited state. This is unsurprising since BPEB has 102 normal vibrational modes and therefore the absorption spectrum is broad and mostly featureless, especially as the torsional motion has been predicted to have a frequency of 8 cm^{-1} [101] or two frequencies of 13.2 and

19.4 cm^{-1} [100]. Even if this frequency could be achieved using conventional infra-red/Raman spectroscopy there are several other low frequency vibrational modes which could confuse analysis, such as bends in and out of the plane.

To be able to study the torsional motion of BPEB, spectral congestion (caused by the many low frequency modes) must be reduced. This can be achieved by using a molecular beam to cool the internal motions of the molecule [103]. This technique was used to elucidate the torsional motion of Tolane [94]. A highly sensitive absorption technique is required to measure transitions, as molecular beams have very low concentrations.

7.2 Molecular Spectroscopy

Absorption Spectroscopy

Absorption spectroscopy is often used to measure the electronic spectra of molecules and clusters in the gas phase. This approach is the most straight forward and accurate means of yielding both quantitative absolute concentrations and absolute frequency-dependent cross-sections.

There are also indirect techniques that are based on the detection of phenomena induced by the absorption of light, *e.g.* fluorescence in Laser Induced Fluorescence (LIF), ions in Resonance Enhanced Multi-Photon Ionisation (REMPI) or pressure changes in photoacoustic spectroscopy. The great advantage of these techniques (over direct absorption spectroscopy) is that they are background free, but disadvantages include; the calibration procedure required to make these techniques absolute (*i.e.* they are not self calibrating), the requirement for states that fluoresce for LIF, or ionize for REMPI. Certain environments, such as flames or plasmas are inaccessible to these other techniques due to collisional quenching for LIF, or the difficulties in extracting charged particles in REMPI.

In comparison to these indirect techniques absorption spectroscopy can see all electronic states that are accessible using one photon.

In absorption experiments the amount of light transmitted through a sample is measured. If the light source is monochromatic (*e.g.* a laser), the absorption spectrum can be measured by recording the transmitted intensity as a function of

photon energy. The absorption of light by a sample is described by the Beer-Lambert law [77], which states the quantitative relationship between the intensity of a spectral feature and the frequency dependent absorption properties of the sample as:

$$I = I_0 \exp(-\sigma \rho l) \tag{7.1}$$

where I and I_0 are the intensities of light leaving and entering the sample respectively, ρ is the number density of the absorber, l is the sample pathlength and σ is the absorption cross-section of the sample at the current wavelength of light. The absorption coefficient, α, is the product of ρ and σ and absorbance is defined as $\sigma \rho l \cdot \log_e 10$. Using the Beer-Lambert law, it can be seen that the detection limit of the absorption technique is governed by the concentration of the sample and the pathlength of the beam through the sample. For experimental systems where the concentration is limited by the technique being used, *e.g.* molecular beam studies, it is, therefore, the pathlength that determines the sensitivity of the experiment. Thus, multiple pass cells have been developed [104, 105] to increase the effective pathlength of the beam through the sample.

The main problem with laser absorption spectroscopy, when detecting inherently weak absorptions, is that the change in intensity of the light as it passes through the sample is very small compared to the initial laser intensity, so the sensitivity is generally limited by fluctuations in I_0.

7.2.1 Cavity Ring-Down Spectroscopy

In comparison Cavity Ring-Down Spectroscopy (CRDS) has very long pathlengths, and is also independent of fluctuations in I_0.

CRDS is a relatively new direct absorption spectroscopic technique which has found a wide range of applications due to its ease of use and high sensitivity. Initially designed to study molecular beams of metal clusters [106], it has become a versatile and widely used tool for studies of molecular spectroscopy and dynamics, with applications in trace gas detection, combustion, weak absorption transitions and low fluorescing yields.

In the CRDS method the rate of absorption of a light pulse confined in a stable optical cavity formed by two highly reflective mirrors (reflectivity, $\mathcal{R} > 99.9\%$) is

measured. An optically stable cavity configuration is achieved by ensuring $0 < l < R$ or $R < l < 2R$, where l is the separation, and R is the radius of curvature of the mirrors. A short laser pulse is coupled into the cavity, this pulse is reflected back and forth inside the cavity and, every time the light is reflected, a small fraction ($\approx 1 - \mathcal{R}$) of this light 'leaks out' of the cavity, leading to exponential decay of the pulse in the cavity. This light is detected by a photomultiplier tube (PMT) and can be recorded using an oscilloscope and PC. The exponential decay time of the cavity is determined by measuring the time dependence of the light leaking out of the cavity. Absorbance is obtained from this time dependence; the greater the absorption of the sample in the cavity, the shorter the measured decay time will be. This approach brings several advantages. The absorption is independent of pulse-to-pulse fluctuations of the laser as it is determined only from the time behaviour of the signal. Furthermore, the effective absorption path length, which depends upon $\mathcal{R}$, can be tremendously long (up to tens of kilometres), while the sample volume can be kept small. Another attractive property is its simplicity; it is relatively easy to construct a CRD set-up out of a few components on a bench-top, a typical set-up is shown in Fig. 7.4.

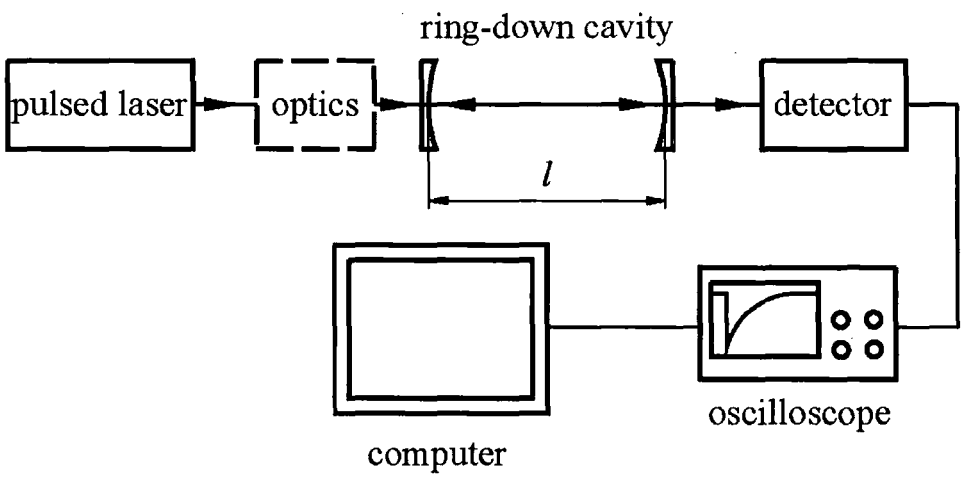

Figure 7.4: Scheme of the standard experimental set-up for pulsed CRDS.

In this section the initial development of the technique will be discussed briefly, along with the developments and uses of CRDS. The requirements for CRDS, with consideration given to the issues of mode matching, will then be reviewed.

Initial Development

The first demonstration of CRDS in 1988 by O'Keefe and Deacon [107] built upon the work of Herbelin *et al.* in the early 1980's [108, 109, 110] and Anderson *et al.* in 1984 [111] to measure mirror reflectivities. This earlier work on mirror reflectivities used Continuous Wave (CW) laser sources. O'Keefe and Deacon bypassed the drawbacks of these techniques, namely unpredictable mode matching and complex experimental set-up, by switching to a pulsed laser system. It is interesting to note that both of these earlier works have been redeveloped into CW-CRDS techniques [112, 113]. The sensitivity of the new technique, demonstrated by measuring the doubly forbidden $b^1\Sigma_g^+ - X^3\Sigma_g^-$ visible bands of O_2 in a static gas cell, was found to be roughly 1 ppm (fractional absorption) per pass. This first CRDS experiment was conducted as a proof of both concept and sensitivity before studying copper dimers and trimers in a molecular beam [106].

The early literature has been reviewed [114, 115] with specific application to pulsed molecular beams.

Continued Development

CRDS is a popular technique, resulting in many publications, and has been applied from 205 nm to 10617 nm almost continuously [116]. Due to the rapid growth in development and application of this technique a full review is beyond the scope of this work, readers are directed towards the comprehensive reviews that have been published on this topic [114, 116, 117, 118] and references therein.

Of all the developments of the CRDS technique only CW-CRDS has found as wide a range of applications as pulsed CRDS ([112, 116, 117] and references therein) due to its increased resolution and higher repetition rate. The lower bandwidth of CW lasers is likely to be less than the free spectral range of the cavity, thus techniques have been developed to match the laser frequency to the cavity modes. This has made the CW-CRDS set-up more complex than pulsed CRDS, even when ultra-high sensitivity is not required. Another disadvantage of CW lasers is that they can only be scanned over small wavelength regions, whereas pulsed dye lasers can be scanned over a large wavelength range, including IR and UV by the use of

nonlinear conversion techniques.

Applications of CRDS

Discussions of the multitude of applications of the CRDS technique can be found in the review articles [114, 116, 117, 118, 119] therefore only a few of the applications will be mentioned here.

CRDS is suited to studying weak absorbances such as electronically forbidden transitions [107, 120, 121]. Overtone transitions are also inherently weak and have been studied using the high sensitivity of CRDS. The reduced concentrations of species in molecular beams are often probed, and are particularly appropriate when using slit jets as the linear expansion can overlap the cavity axis [122, 123, 124, 125].

O'Keefe and Deacon recognised the potential application to atmospheric pollution analysis, *i.e.* the detection of trace gases [126, 127, 128, 129], and hostile environments such as combustion. The application of CRDS to measurement of radicals in flames has been discussed by Cheskis [130], radical species probed include; OH [131], CH [132, 133], CN, CH_2, H_2O, HCO, CH_3, CH_2, H_2O as well as soot. Radicals are also probed, along with other species, by CRDS during diamond growth [134, 135, 136], which uses plasmas, another hostile environment that can be probed by CRDS [137, 138].

An overview of CRDS used in the study of fast predissociation of electronically excited states of small molecules and radicals has been given by Wheeler *et al.* [119]. The technique has also been applied to reaction kinetics [119, 139, 140], and intramolecular vibrational redistribution (IVR).

7.2.2 Principles of CRDS

In this section we discuss the decay of light intensity leaving the cavity after excitation by a pulsed laser, and how absorption coefficients can be calculated from the decay rate. Later in this section cavity mode effects will be discussed.

The decay of the intensity of light that leaks out of a ring-down cavity at a set wavelength is given by an exponential:

$$I(t) = I_0 \exp(-t/\tau) \tag{7.2}$$

Where τ is the empty cavity ring-down time (RDT), the time for the intensity to decay to $1/e$ of its original value. This is determined by the reflectivity of the mirrors and the optical pathlength, l, between the mirrors. Mirror transmission, diffraction and scattering are generally much smaller than the reflection losses of the mirrors, and $\mathcal{R} \approx 1$, therefore $|\ln \mathcal{R}| \approx (1 - \mathcal{R})$, thus

$$\tau = l/c|\ln \mathcal{R}| \approx l/c(1 - \mathcal{R}) \tag{7.3}$$

where c is the speed of light. The empty cavity RDT is thus determined by these loss processes, and depends strongly on the reflectivity of the mirrors. For a cavity bound by two mirrors of reflectivity $\mathcal{R}$, the number of round trips, N, performed in the time taken for the intensity to fall to $1/e$ of its initial value is obtained from $N = -1/[2\ln(\mathcal{R})]$. So for a 1 m cavity with mirrors of only $\mathcal{R} = 0.999$, $N = 500$ and the effective path length is 0.5 km. It is these long effective path lengths that help to give CRDS its high sensitivity.

When the wavelength of light matches an absorption of a sample held between the mirrors the decay of light in the cavity is faster. If the absorption conditions correspond to Beer-Lambert law behaviour, the decay of the light intensity will be exponential:

$$I(t) = I_0 \exp\left(-\frac{t}{\tau} - \alpha c t\right) \tag{7.4}$$

Where α is the molecular absorption coefficient. The product of c and t is the total pathlength, L, over which the absorption is measured. The RDT is now given by

$$1/\tau' = 1/\tau + c\alpha. \tag{7.5}$$

If the empty cavity RDT, τ, is known, measurement of the decay rate of the light intensity as a function of laser wavelength gives the absorption coefficient as a function of wavelength, and hence the absorption spectrum. For a discrete spectrum, τ can be determined from the baseline level between absorption features (where $\alpha = 0$). For a non-discrete spectrum τ can be obtained from a scan of the cavity under the same conditions but without the absorbing species present, known as a 'mirror scan'. Absorption cross sections can be obtained if the partial pressure of the absorbing species in the cavity is known.

Two simple methods for extracting spectra from the exponential decays recorded at each laser wavelength are as follows. (i) Direct fitting (*e.g.* least-squares fitting) of the exponential decay or of its logarithm. The fit will give the decay time τ', the magnitude of τ' determines the effective pathlength through the sample. (ii) Setting two gates of equal width on the exponential at some time separation Δt. This time separation then determines the pathlength, and manipulation of the signal at the two time gates gives a value that is directly proportional to the absorption coefficient.

Both methods rely on the decay being a true exponential in order to extract accurate values. Care must be taken when averaging data for a spectrum, as it is mathematically incorrect to average out shot-to-shot fluctuations by adding a series of exponential decays for multiple laser shots at a particular wavelength and then fitting the resultant decay to obtain an absorption coefficient. The correct procedure must be to fit each decay separately and average the resultant absorption coefficients [119].

The direct fitting method has the advantage of being able to check if the decay of light intensity is exponential. The decay can become non-exponential if Beer-Lambert behaviour for a single pass of the light through the cavity is violated, or if interference effects between the longitudinal and transverse modes of the cavity become pronounced (see Section 7.2.2). If non-exponential decay is observed, transition intensities and absorption coefficients obtained using a single exponential fit will become inaccurate.

Beer-Lambert Behaviour

Beer-Lambert behaviour requires the spectral absorption lines to be wider than the bandwidth of the laser light within the cavity. If an absorption line is narrower than the bandwidth of the light in the cavity a bi-exponential decay will occur, with the frequency of the absorbed light decaying faster than the rest of the laser pulse.

If the duration of the laser pulse, t_p, in the cavity is less than the lifetime of the upper state of the medium in the cavity, T_2, (determined by radiative and non-radiative decay rates), the pulse will have a spectral content that is broader than the absorption line of the attenuating medium [141]. If the round trip time of the

cavity, t_r, is greater than T_2 then the absorption feature will span many cavity modes, and a smooth complete absorption spectrum can be recorded [142]. These issues of timescale have been discussed in detail by Zalicki and Zare [142]. For the CRDS studies of BPEB, whose fluorescence lifetime is 530 ps [102], this important criterion was satisfied.

Mode Effects

The implications of cavity mode structure for CRDS have been discussed by several authors [142, 143, 144, 145, 146] both time and frequency domain treatments have been used, with the two methods linked by Fourier transform. Exponential decay of light within the cavity can be shown to be equivalent to the cavity possessing Lorentzian longitudinal cavity modes [143]. The frequency spacing of these modes, also called the free spectral range (FSR) of the cavity, $\Delta\nu$, is dependent upon the round trip time, t_r, of light within the cavity:

$$\Delta\nu = \frac{1}{t_r} = \frac{c}{2l} \tag{7.6}$$

If the spacing of the longitudinal modes in a cavity is greater than the width of an absorption feature the absorption line will not contribute to the rate of decay of light in the cavity and so will not appear in the spectrum [143]. If the probe laser has a bandwidth smaller than the cavity mode spacing then light will only be coupled into the cavity, and therefore give a ring-down event, when it has a frequency that matches a cavity mode. As long as the bandwidth of light used spans several cavity modes the probe laser can be scanned continuously.

A ring down cavity does not only contain longitudinal modes. For each longitudinal mode there are corresponding transverse electro-magnetic (TEM) modes as well. These modes are denoted TEM_{qmn}, where m and n are the order of the Gauss-Hermite polynomials for the transverse modes, for each longitudinal mode q. The frequencies of the TEM modes are given by:

$$\nu_{qmn} = \frac{c}{2l}\left[q + (m+n+1)\frac{2}{\pi}\arctan\left(\frac{l}{\sqrt{l(2R-l)}}\right)\right] \tag{7.7}$$

where R is the radius of curvature of the cavity mirrors and adjacent TEM modes [$\Delta q = 0$ and $\Delta(m+n) = 1$] are separated by $\nu_{\mathrm{tr}} = (c/\pi l)\arctan[l/\sqrt{l(2R-l)}]$. In

general, transverse and longitudinal modes are not degenerate and there is essentially a quasi-continuum of modes [144]. The TEM modes can be observed in the output from a ring-down cavity, Fig. 7.5, and observation of these modes using a charge-coupled device (CCD) camera has been used to optimize mode matching [144, 147].

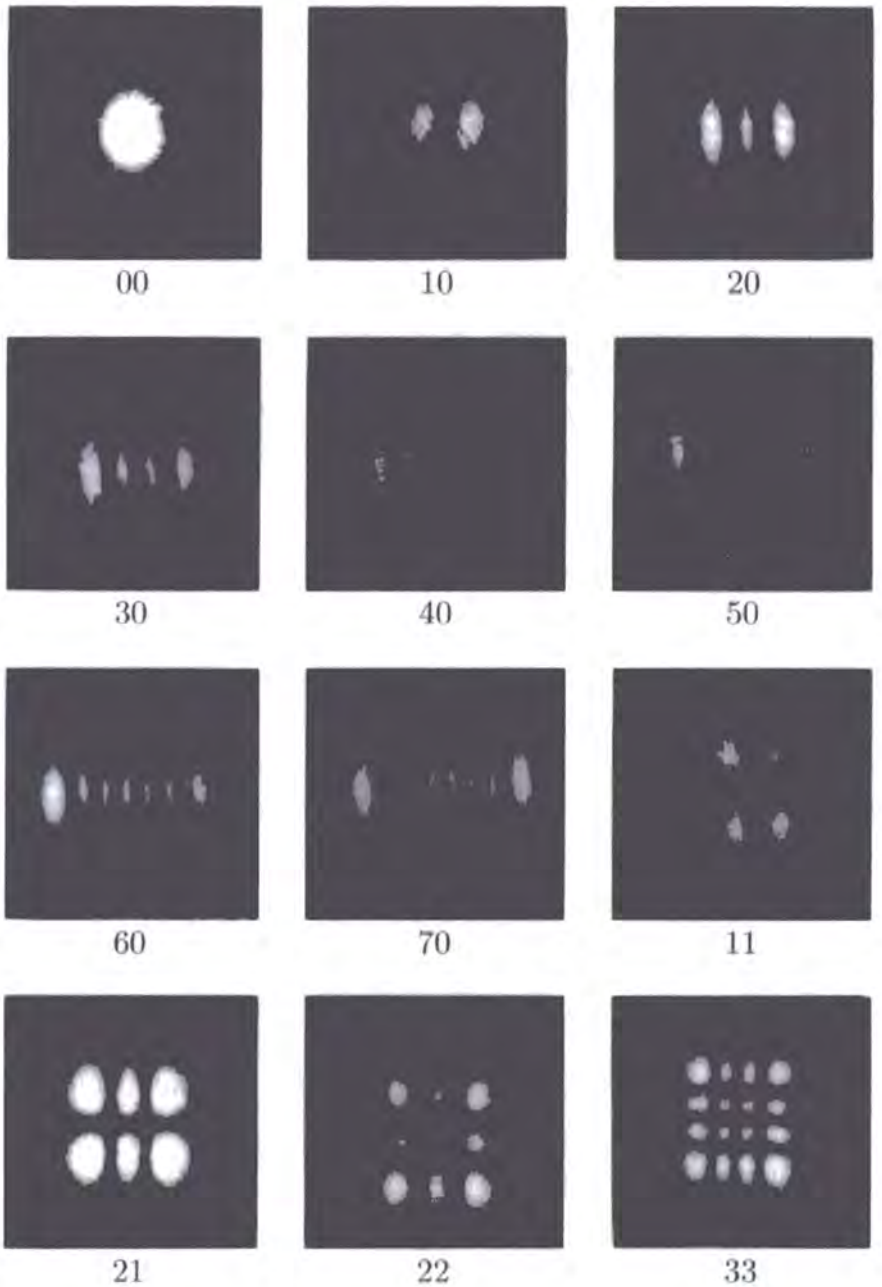

Figure 7.5: Pictures of TEM modes of an optical cavity, the numbers under the images are the m and n values for that mode. [148].

If a single Lorentzian cavity mode is excited, then the decay of the light intensity

within the cavity will be exponential. However, if several cavity modes are excited then the decay of light will be multi-exponential, unless the different modes have the same loss per round trip. Non-exponential decays can still occur in this case due to beating caused by interference between the different frequency components in the (longitudinal) modes. If multiple transverse modes are excited then beatings can occur between the slightly different decay rates of the TEM_{mn} modes. As shown by Martin *et al.* [145] and Lee *et al.* [146] these mode beatings lead to slow oscillations superimposed on the single exponential decay.

Whilst fast beatings can be filtered out electronically, Lee *et al.* [146] have proposed a general purpose alignment scheme to optimize mode matching and improve sensitivity. This will work for all frequencies and does not require a CCD camera. The technique involves introducing a pinhole between the cavity exit mirror and the photomultiplier tube (PMT) detector, and aligning the cavity to minimize the mode beating on the ring-down trace caused by this. Once the cavity is aligned the pinhole is removed before spectra are recorded.

Transverse mode beatings are minimized by suppressing the higher order TEM_{mn} modes by spatially matching the input laser beam to the TEM_{00} mode of the cavity. In practice this is achieved using a telescope and pinhole arrangement to form a Gaussian beam [146]. This Gaussian beam can then be coupled into the TEM_{00} mode of the cavity. A ring-down cavity is an optical resonator, and as such, it supports an electromagnetic field whose spherical wavefront matches the curvature of the mirrors. To efficiently couple into a transverse mode of the cavity the focus of the input light has to match the waist of the cavity with the correct spot size [149]. A measure of the spot size at the cavity waist is ω_0, defined as the radius of the beam at the centre of the cavity, where the light intensity drops to $1/e$ of its value on the axis. In practice this can be achieved by the addition of a 'coupling' lens before the cavity, as shown in Fig. 7.6.

For this discussion of optical resonators we closely follow the approach of Yariv [150]. For a symmetric mirror resonator ω_0 is defined by

$$\omega_0 = \left(\frac{\lambda z_0}{\pi n}\right)^{1/2} \tag{7.8}$$

where λ is the wavelength of light, n is the refractive index of the medium in the

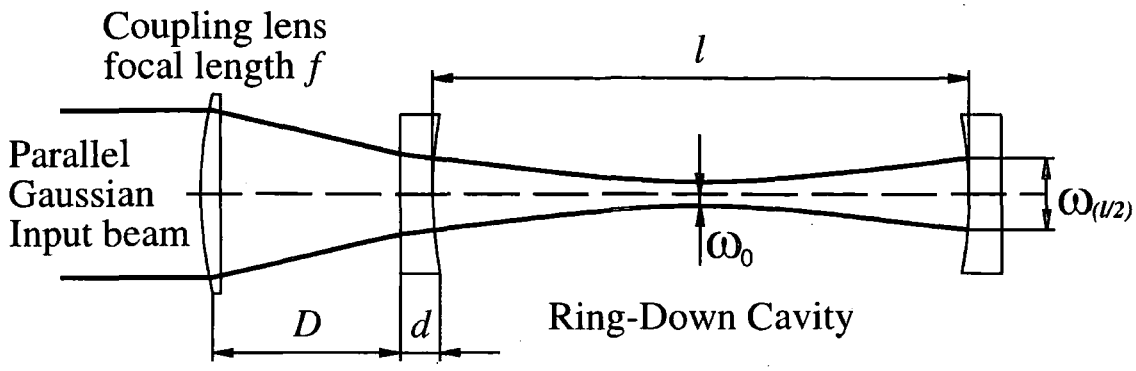

Figure 7.6: A theoretical RDC with coupling lens, showing the light path into the cavity, the beam waist ω_0, the size of the beam at the output mirror $\omega_{(l/2)}$, and all relevant dimensions.

cavity and z_0, the characteristic length of the cavity, which is given by

$$z_0 = \frac{(2R - l)l}{4} \tag{7.9}$$

where R is the radius of curvature of the mirrors. This allows the calculation of the beam spot size at the mirror,

$$\omega_{(l/2)} = \omega_0 \left[1 + \frac{l}{2z_0}\right]^{1/2} \tag{7.10}$$

which, along with the gradient of the beam at the mirror $[\omega'_{(l/2)} = \omega_{(l/2)}/R]$ can be used with ray matrices (see Yariv Ch. 2 [150]) to calculate the position, and focal length, of the lens which will efficiently couple a parallel Gaussian beam into the cavity. It is important to note that because the mirror acts as a diverging lens the lens cannot be placed at its focal length away from the centre of the cavity. Ray matrix calculations lead to a formula for the gradient of the light incident on the lens, r'_{lens}, which has to equal zero for a parallel input beam (see Appendix C):

$$r'_{\text{lens}} = \frac{\omega_{(l/2)}(-n_2R - dn_2 - Dn_1 + n_1f)}{fn_2R} \tag{7.11}$$

Where d is the thickness of the mirror, n_1 is the refractive index of the mirror substrate and n_2 is the refractive index of air (outside the cavity). This leaves two unknowns, the focal length of the coupling lens, f, (which is governed by commercial availability), and its distance from the input mirror of the cavity, D, so the equation can be solved for D for a given f. See Appendix C for full details.

Sensitivity

The sensitivity of CRDS is commonly given as the fractional loss of intensity per round trip, $\delta I = (I_0 - I)/I_0$ [114]. The Beer-Lambert law states that for a single pass through a cavity with an absorbing sample of length l_s, the absorption is

$$I = I_0 \exp(-\alpha l_s) \tag{7.12}$$

and for very small absorbancies in a single pass ($\alpha l << 1$), it can be approximated that

$$\delta I = \frac{I_0 - I}{I_0} \approx \alpha l_s \tag{7.13}$$

For a change in the ring-down time $\Delta\tau = \tau - \tau'$ on an absorption feature, the corresponding absorbance per pass is [142]

$$\alpha l = (1 - \Re)\frac{\Delta\tau}{\tau'} \tag{7.14}$$

Hence the minimum detectable fractional absorption per pass (or absorbance per pass) can be written as

$$\delta I_m \approx (1 - \Re)\frac{\Delta\tau_{\min}}{\tau} \tag{7.15}$$

where $\Delta\tau_{\min}$ is the minimum detectable change in ring-down time on absorption.

As can be seen from equation 7.15 the ultimate sensitivity of CRDS is dependent upon the precision with which $\Delta\tau$ can be measured. This is, in turn, dependent upon a range of practical considerations, which have been discussed in detail elsewhere [114]. The ability to measure small changes in RDT is improved with longer ring-down times, which can be gained by increasing mirror reflectivity, but will be reduced by strong absorptions. Other factors to consider are the resolution of the detection electronics and noise from the laser system (shot noise) and the detector. In the detection electronics a major limiting factor is the digitizing system used, for example an 8 bit digitizer has a resolution of 1 part in 256, but a 12 bit digitizer has a resolution of 1 part in 4096, a factor of 16 better. Shot noise is insignificant compared to other sources of noise, as the uncertainty in the amplitude of a single pulse exiting the cavity is insignificant, because there are thousands of pulses exiting the cavity during a ring-down event [114].

Chapter 8

Experimental Development and Characterisation

8.1 Experimental

This section describes the development of the experiment from a bench-top set-up used to investigate the practical aspects of CRDS, through the development of a Molecular beam (MB) apparatus, tested by recording the iodine spectrum, to its final application recording the jet cooled spectra of BPEB.

8.1.1 Equipment Development

Starting From Scratch

The initial CRDS set-up was designed to mimic the first CRDS experiment of O'Keefe and Deacon [107], a small bench top experiment observing the (2-0) band of the O_2 $b^1\Sigma_g^+ - X^3\Sigma_g^-$ system.

This initial experimental set-up used a pulsed (10 Hz repetition rate) Nd:YAG laser (Spectra-Physics GCR-150) to pump a dye laser (Spectra-Physics PDL 3) with DCM dye (175 mg/litre in MeOH, giving a wavelength range of 620 to 660 nm), only low power was required so the PDL was run with oscillator only, giving an output of 0.1 mJ. The ring-down cavity was formed by two highly reflective plano-concave mirrors (Layertec, $R = 1$ m, $\geq$99.98% reflective between 585 and 650 nm) held in kinematic mirror mounts (Thorlabs) with a separation, L, of 79 cm on a laser table.

The dye laser output was steered along the cavity axis after initial alignment of the cavity using a HeNe CW laser.

A spatial filter consisting of a lens (planoconvex, 100 mm) pinhole (diameter 100 μm) and lens (planoconvex, 50 mm) was used to ensure all light entering the cavity had a Gaussian profile, as described by Lee *et al.* [146] (The pinhole was chosen to be 30% bigger than D, the diffraction limited spot size, $D = \lambda f/r$ where f is the focal length of the 1st lens and r = input beam $1/e^2$ radius.). The spatial filter was used in combination with a 500 mm lens (mounted in an x-y adjustable lens holder) in front of the cavity entrance mirror to allow the laser light to be coupled predominantly into the TEM_{00} mode of the cavity.

Laser light passing through the exit mirror of the cavity was detected by a photomultiplier tube (Hamamatsu PMT: Model R1463; Quantum efficiency: maximum 20% at 350 nm, 6% at 600 nm) mounted in a black Delrin cylinder to ensure that stray light was unable to reach the PMT. The PMT voltage was adjusted to between 380 V to 420 V to observe an exponential ring-down curve; a balance was struck between light input levels and PMT amplification to avoid distortions resulting from over-saturation of the detector or non-linear PMT response. The PMT was coupled (50Ω coupling) to a digital oscilloscope (Tektronix TDS320). The exponential traces were transferred from the scope, via an RS232 serial port, to a PC running a customised version of a LabVIEW (National Instruments) program developed at the University of Bristol [151].

The program normalised the data by subtracting the baseline (region of trace before the ring-down event corresponding to no laser light in cavity) from the exponential curve. A least-squares fit was performed on the natural logarithm of these data to obtain a straight-line graph. The inverse of the gradient of this linear fit gave the ring-down time. The least-squares fit was also used to calculate the mean squared error (MSE) of the exponential fit, which was compared with a user set value of maximum MSE so that non-exponential curves could be excluded from data acquisition (*i.e.* if the spread of points around the fitted line was significantly large to indicate non first order exponential behaviour). MSE was calculated using

$$\mathrm{MSE} = \frac{1}{n}\sum_{i=0}^{n-1}(f_i - y_i)^2, \tag{8.1}$$

where n is the number of data points, y is the natural logarithm of the data point and f is the equivalent point on the fitted line. Potential causes of these non-exponential curves were discussed in Section 7.2.2.

Due to the very slow data transfer rate via the RS232 serial port, between the scope and PC typically four laser shots were averaged on the oscilloscope before data transfer to the computer. Further summing over a number (typically three) of calculated ring-down times on the PC allowed spectra with reasonable signal/noise ratios to be recorded. This was only used as a stop-gap measure to assist experimental development until better data transfer rates could be achieved to analyse each laser shot in real time.

To acquire a spectrum, the dye laser was stepped through the wavelength range of interest. A multifunction I/O card (National Instruments, PCI-6024E) in the PC was used to control a driver box (Chemistry Electronics Workshop) which stepped the PDL 3 by 0.003 nm (equivalent to one step of the stepper motor) when an averaged RDT had been obtained at the current wavelength.

These first bench top experiments were used to prove the functionality of our new CRDS set-up before moving onto more complex set-ups, for more details see Ref. [152].

The subtleties of cavity ring-down were highlighted by these experiments, especially the need for a good laser profile and how to overcome the issue of mode beatings. The spectra of oxygen in air taken using this bench top set-up were of low quality, due to the open cavity and air movement in the lab.

Molecular Beam Apparatus

The next step in the experimental development was the design and construction of a vacuum chamber to study molecules in molecular beams with CRDS. The chamber design was based around a 6-way cross (BOC Edwards, 100/80 ISO-K/F) Fig 8.1. On one pair of horizontally opposed arms, 80 ISO-K, extension tubes, DN16CF standard, were built for the cavity axis. On the end of these tubes were flexible knife edged bellows (CF 16) onto which the cavity mirrors were mounted as end windows for the cavity, which had a length of 77 cm. The mirrors were secured in place by external Delrin mounts, which also served to mount irises central to

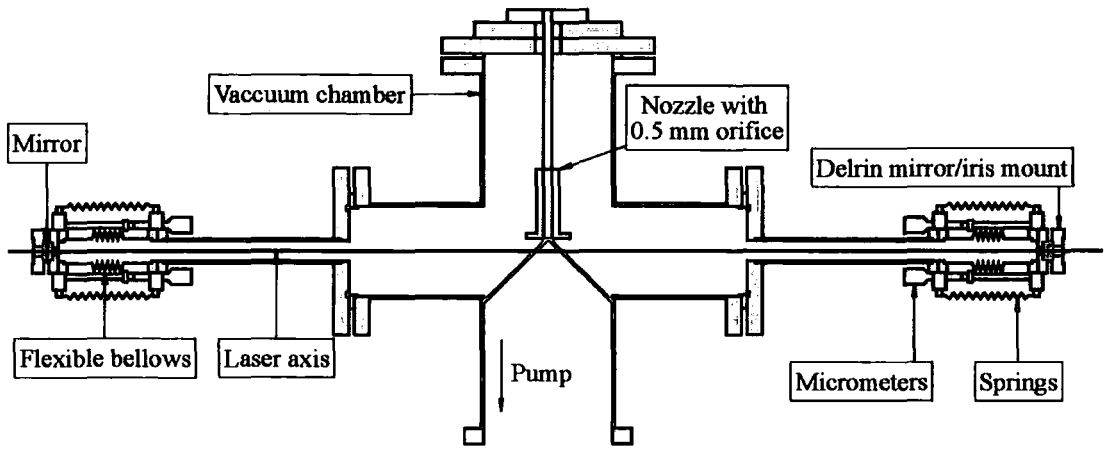

Figure 8.1: Schematic of the vacuum chamber designed for the study of molecules in a MB.

the mirrors. Mirror positions were adjusted by micrometer screws (Thorlabs) in a configuration designed to replicate a kinematic optical mount. Two micrometers were used for independent vertical and horizontal adjustment about a ball bearing pivot, a third micrometer was available to 'lock' the adjustment.

A diffusion pump (BOC Edwards CR100/300, 230 ls^{-1}), backed by a rotary pump (Varian DS202, 8.3 m^3 per hour) which allowed the chamber to be pumped to pressures of approximately 1×10^{-7} mbar, was mounted below the chamber on the lower arm of the vertical axis, 100 ISO-K. A quartz observation window and a blank flange were mounted on the other two horizontal arms of the cross.

This new set-up was initially used as a cell, with closed pumps, to acquire the spectrum of O_2 in a static air sample at 1 bar.

New Lasers

A new laser system was used for the remainder of the experiments, Fig. 8.2 shows this new optical set-up. The second harmonic of a Nd:YAG laser (Continuum, Surelight I-10 with second harmonic generator (SHG) and dichroic separator (DS), pulse length 5 ns) was used to pump a pulsed dye laser (Sirah, Cobra Stretch with optional SHG and 4× Pellin-Broca separator) with DCM dye (300 mg/litre in methanol, oscillator only) giving a wavelength range of 602 to 660 nm. Prism 1 was placed inside the dye laser to steer the light out of the laser before it passed through the SHG. The

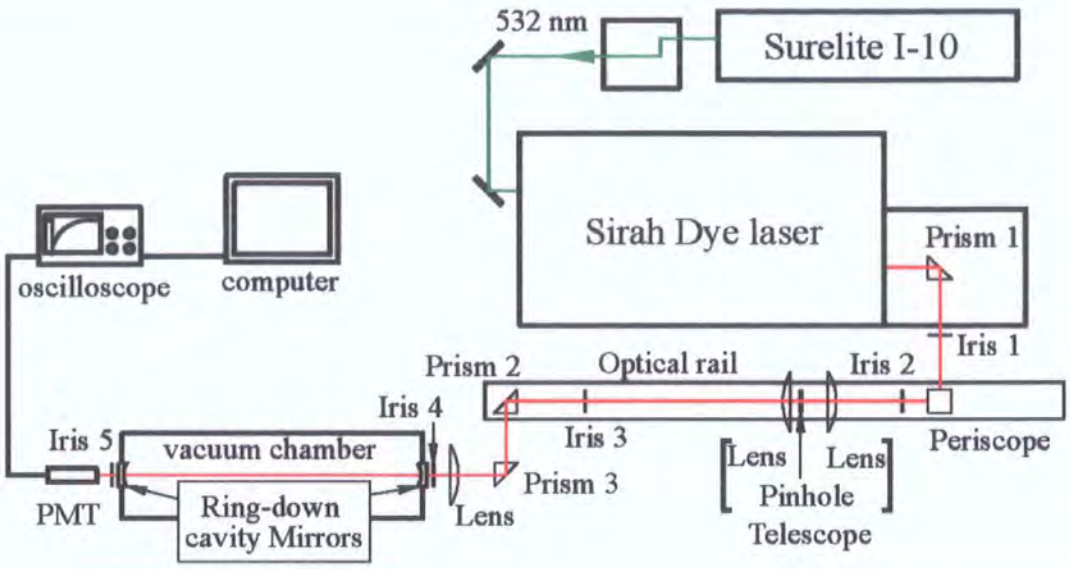

Figure 8.2: New experimental set-up.

periscope was used to lower the height of the laser beam to match the height of the optical cavity. The telescope arrangement (described above), periscope, irises and prism 2 were all mounted on an optical rail (Linos X-95) which allowed all optics to be moved smoothly and reproducibly back and forth along the rail. After passing through the cavity the laser light was detected by the PMT which was coupled to a new digitizing oscilloscope (LeCroy, Waverunner LT584), which in turn was connected to a PC via a GPIB card (National Instruments). This allowed real time data transfer at the laser repetition rate (10 Hz).

The new equipment was used to repeat the O_2 spectra experiment described above, the results, Fig. 8.3, show the increased resolution achieved with the Sirah dye laser (Sirah bandwidth at 628 nm: 0.06 cm^{-1}, the PDL specification claims a bandwidth at 628 nm of 0.06 cm^{-1}, but the spectrum clearly shows otherwise).

Nozzle Arrangement

The experiment was changed to create a molecular beam (MB) to intersect the laser axis within the cavity. A nozzle was mounted at the end of a 1/4″ pipe, to deliver the gas to the nozzle. An o-ring sealed feedthrough (Cajon, Ultra-Torr fitting) allowed the pipe, and hence the nozzle, to be moved vertically to adjust the distance between

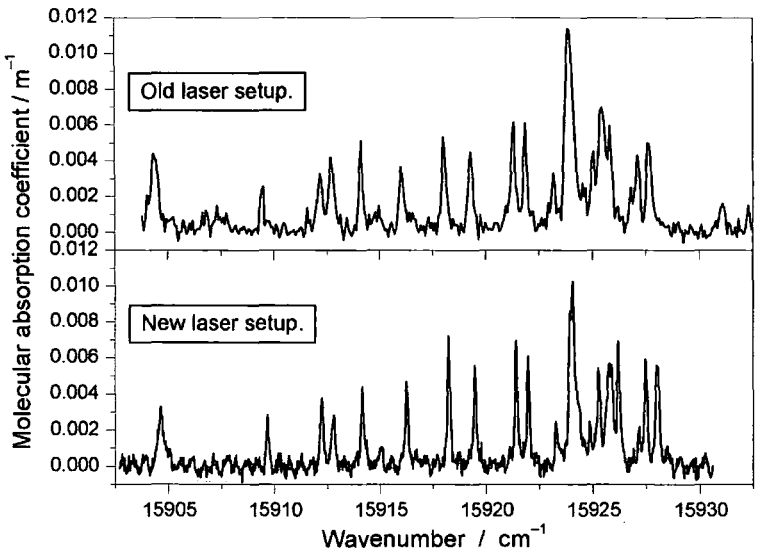

Figure 8.3: Comparison of O_2 in air (within the chamber) spectra using the old (top, PDL 3) and new (bottom, Sirah) laser systems.

the nozzle and laser axis, typically 5–8 mm. The feedthrough was, in turn, mounted on a stage that allowed horizontal adjustment of the nozzle position to gain best overlap of molecular beam and laser. This whole nozzle apparatus was mounted on the upper arm of the vertical axis of the vacuum chamber, as shown in Fig. 8.1. The pressure in the chamber was monitored using a pressure gauge (Leybold, Ionivac ITR90, #12091).

Jet Cooled Spectroscopy

Temporal overlap of the molecular beam and laser was achieved with the use of a delay box (University of Bielefeld, Physics Department) to control both the firing of the laser and the nozzle, via a pulse driver (Parker Instrumentation, Iota One). An approximate time delay between firing the nozzle and laser was calculated considering the carrier gas used (Ar) and the distance between the nozzle and the laser axis. This time delay was then adjusted to optimise signal levels.

Iodine was chosen as a test molecule for this experiment, due to its large absorption coefficient and well known spectrum. Iodine spectra were recorded in the wavelength range of 567.5–569.3 nm using mirrors that had a maximum reflectivity occurring at 570 nm (Layertec, plano-concave $R = 1$ m, $\geq$99.97 reflective between

545 and 595 nm). The dye in the Sirah laser was also changed, to Rhodamine 6G (90 mg/litre in methanol, oscillator only, 10 μJ at 565 nm) giving a wavelength range of 559 to 576 nm.

Optimising Gas Delivery

First tests used I_2 in a glass bulb just outside the chamber to seed the beam, but most of the I_2 re-condensed on the walls of the pipe into the chamber, so only very low signal levels were detected. To minimize the amount of I_2 recondensing before the expansion, the next seeding attempt utilised an I_2 source as close to the expansion as possible, inside the nozzle body. I_2 crystals were sandwiched in glass wool at the top of the nozzle, so as not to interfere with the nozzle mechanism. Unfortunately the I_2 just recondensed lower in the nozzle clogging up the orifice, preventing a proper beam expansion.

Finally, an inline filter, with a 7 micron filter element (Swagelok), was introduced into the gas line just before the nozzle, Fig. 8.4. Heaters (Omegalux, Kapton flex-

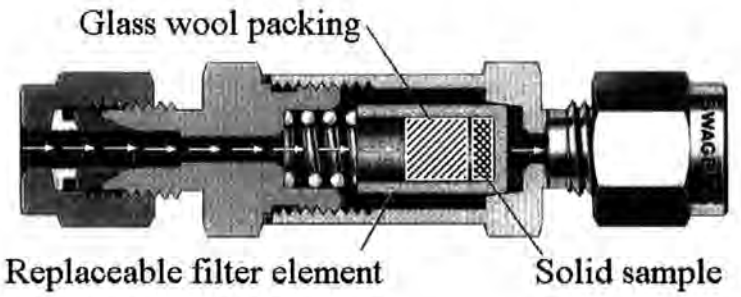

Figure 8.4: Inline filter for beam seeding, a 7 micron replaceable filter element was used for the I_2 experiments. The white arrows indicate the direction of gas flow.

ible heater, low voltage) with an external adjustable DC power supply (SkyTronic, 650.682) were attached to the inline filter and nozzle to increase the quantity of I_2 in the carrier gas and prevent it from re-condensing in the nozzle. A thermocouple (K type) was used to monitor the temperature of the inline filter with the temperature displayed on a digital thermometer (Fluke, 50D). Spectra could now be acquired to optimise experimental conditions and characterise the experiment.

Jet Cooling

Jet cooling works by expanding a small quantity of a sample molecule in a carrier gas from a high pressure region through a small orifice into a vacuum chamber. As the molecules accelerate into the vacuum they undergo a large number of two- and many body collisions. Elastic collisions equalise the speed of the molecules in the beam (translational cooling). Internal motions are cooled by inelastic collisions where the chances of high energy transfer are less likely. Thus, cooling of vibrations is much harder to achieve than rotational cooling due to the larger quanta of the internal motion, *i.e.* $T_{\text{vib}} > T_{\text{rot}}$. The greater the number of collisions the greater the chance to match the quantization of an internal motion.

The choice of backing gas used has an effect on the temperature of the molecular beam produced. Monoatomic carrier gases (e.g. Ar) result in spectra of colder molecules than diatomic carrier gases (e.g. N_2), because the carrier gas atoms do not have to be cooled rotationally and vibrationally. Therefore the absorbing species under investigation are cooled to a greater extent, resulting in a colder molecular beam. The lower the temperature of the molecular beam the higher the concentration of molecules occupying the lowest rotational and vibrational levels (Boltzmann). Spectra of cold molecules are less congested and can thus be interpreted more easily than 'hot' spectra.

8.1.2 Test Results

Iodine Spectra

Iodine spectra were obtained under various conditions to optimise the cooling effect of the molecular beam and the signal levels. A range of temperature and backing pressure conditions was investigated, for each temperature and pressure the PMT voltage, nozzle delay and duration were optimised. It was found that the optimum conditions were a temperature of 80 °C and a backing pressure of 3.5 bar Ar. This provided the best signal intensity as well as the lowest rotational and vibrational temperatures. Higher backing pressures increase the density of the molecules passing through the nozzle orifice, allowing more collisions to occur between the molecules. Higher backing pressures could not be used due to the pumping speed of the diffusion

pump. Higher temperatures could not be used as the increased signal levels would have reduced the sensitivity of the experiment at the bandhead.

Rotationally resolved iodine spectra were obtained under optimum conditions for the wavelength range 567.5–569.3 nm, with the CRDS program summing over 10 laser shots. A typical spectrum showing both the $(v' \leftarrow v'')(17\leftarrow0)$ and $(19\leftarrow1)$ bands of the $B^3\Pi^+_{0u}$–$X^1\Sigma^+_g$ transition of iodine can be seen in Fig. 8.5. The spec-

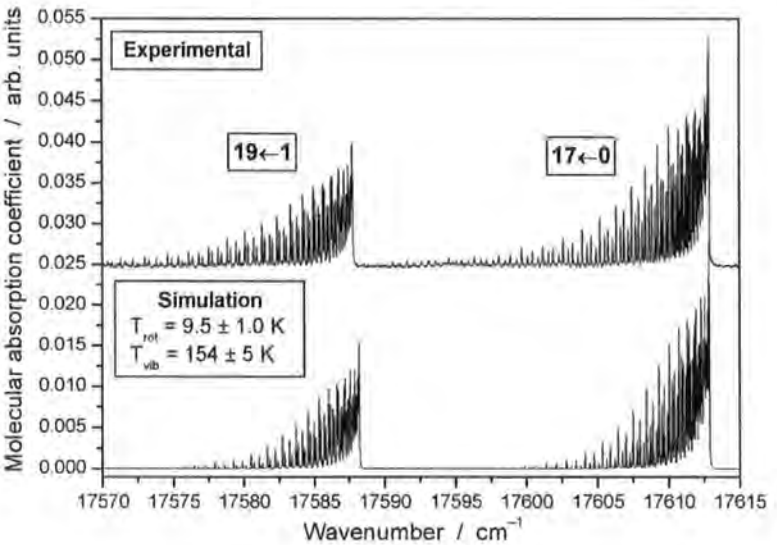

Figure 8.5: Iodine spectrum showing $(v' \leftarrow v'')(17\leftarrow0)$ and $(19\leftarrow1)$ bands of the $B^3\Pi^+_{0u}$–$X^1\Sigma^+_g$ transition of the experimental and simulated absorption spectra of iodine, between 567.5 and 569.3 nm. The experimental spectrum was obtained using 0.0005 nm steps and summing over 10 laser shots per step. The nozzle was heated to 80 °C with a backing pressure of 3.5 bar Ar.

trum is given with arbitrary units for the molecular absorption coefficient as the concentration of I_2 in the molecular beam was unknown.

The simulated spectrum of the $(v' \leftarrow v'')(17\leftarrow0)$ and $(19\leftarrow1)$ bands of the $B^3\Pi^+_{0u}$–$X^1\Sigma^+_g$ transition of iodine was used to determine the rotational and vibrational temperatures of the molecular beam. The simulated spectrum was obtained using the WI2 program [153] which used spectroscopic constants to simulate the iodine spectrum for this electronic transition over the required wavelength range. The spectroscopic constants have been determined in many previous studies of the electronic spectra of iodine [154]. To simulate the spectrum the following variables were adjusted to give the best fit, by observation, to the experimental spectrum; the temperature of the iodine, Gaussian and Lorentzian linewidths that control the

shape of the absorption peaks and a wavenumber offset to allow the band heads to be aligned. The sum of the Lorentzian and Gaussian factors should be approximately the bandwidth of the laser, in this case (at 568.5 nm) 0.074 cm^{-1}. For the spectrum shown the Lorentzian and Gaussian linewidths were respectively 0.026 and 0.032 cm^{-1}, the sum of which is 0.058 cm^{-1}, approximately the laser bandwidth. The T_{rot} of the molecular beam was found by obtaining the best match, by observation, to both bandheads in the experimental spectrum, with an accuracy of 1 K. T_{vib} was obtained from a separate simulation, where the relative heights of the 17←0 and 19←1 bandheads best match the relative heights found experimentally. T_{vib} could only be determined to an accuracy of 5 K.

From the 17←0, and 19←1, bands of the experimental iodine spectrum, the rotational and vibrational temperatures of the molecular beam have been determined to be T_{vib} 154 ± 5 K and T_{rot} 9.5 ± 1 K, indicating the production of a cold molecular beam. The, 24←3, band also occurs in the wavelength range 567.5-569.3 nm with a bandhead at 17602.9567 cm^{-1}, it was only visible in spectra when the vibrational temperature was above 220 K. Its absence from the experimental spectrum confirmed the low vibrational temperature of the molecular beam produced. The shape, relative peak positions, and relative peak heights of the 17←0, and 19←1 bands of the experimental iodine spectrum, matched the simulation well.

The peak positions of the P and R branches were generated during the simulation of the spectrum in the WI2 program. Fig. 8.6 shows the P and R branch assignments of the absorption peaks in the 19←1 band. The experimental spectrum was a good match with the simulation and peak assignment. The molecular beam used was found to be very cold, 9.5 ± 1 K, resulting in a well resolved spectrum, allowing an unambiguous peak assignment.

Due to the larger energy gaps between the higher rotational states, as well as the spread of temperatures in the molecular beam (the outer part of the expansion was warmer as it undergoes fewer collisions), peaks can be seen in the tail of the experimental spectrum that are not in the simulated equivalent. The simulation was used to give an approximate rotational temperature in the tail of 15 K. It was also necessary to shift the bandhead of the 17←0 band by +0.86 cm^{-1} and the bandhead of the 19←1 band by +1.3 cm^{-1}. This shift could be considered to be the

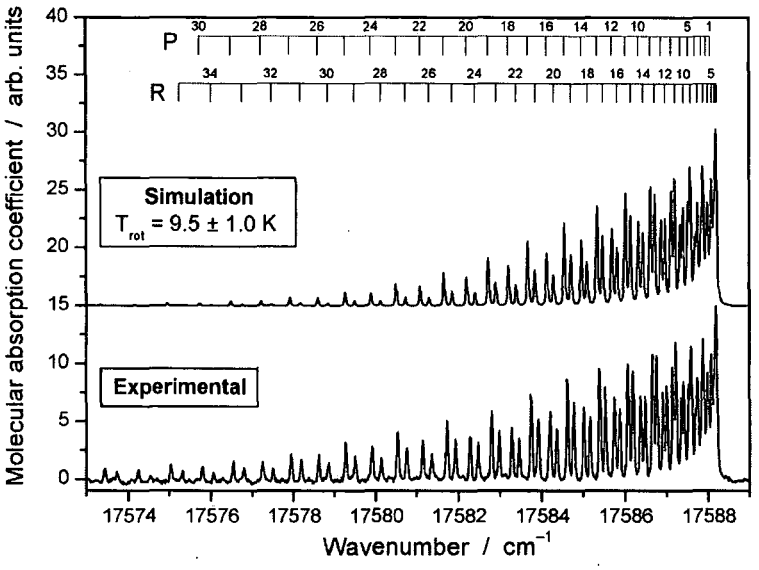

Figure 8.6: Iodine spectrum showing the 19←1 band with simulation, used to assign P and R branches as well as rotational temperature, between 567.5 and 569.3 nm, with summing over 10 laser shots. The nozzle was heated to 80 °C and a backing pressure of 3.5 bar Ar was used.

discrepancy of the factory laser calibration, but as two different shifts were required for the bands further investigation was necessary.

Initial BPEB Spectra

To our knowledge BPEB had not yet been used in gas phase spectroscopic studies, therefore, to investigate the wavelength range required for the CRDS experiment spectra were required in the gas phase. The spectrum of BPEB in cyclohexane solution, Fig. 8.7, show a series of partially resolved absorption bands between 250 and 350 nm [93], as cyclohexane is a non-polar solvent the gas phase spectrum was not expected to shift.

To obtain the gas phase spectrum a sample of BPEB (synthesised by S. R. Rutter, Department of Chemistry, Durham) was placed in a cylindrical glass cell with quartz windows at both ends. The cell was evacuated using a rotary pump, ultimate pressure $\approx 10^{-2}$ mbar. Heaters (Omegalux, Kapton flexible heater) were used to raise the cell temperature to between 110–130 °C to produce BPEB vapour. The gas phase spectrum was recorded with a UV-Vis spectrometer (Unicam UV-4), and is shown in Fig. 8.7. As the intensity of the absorptions are dependent upon the

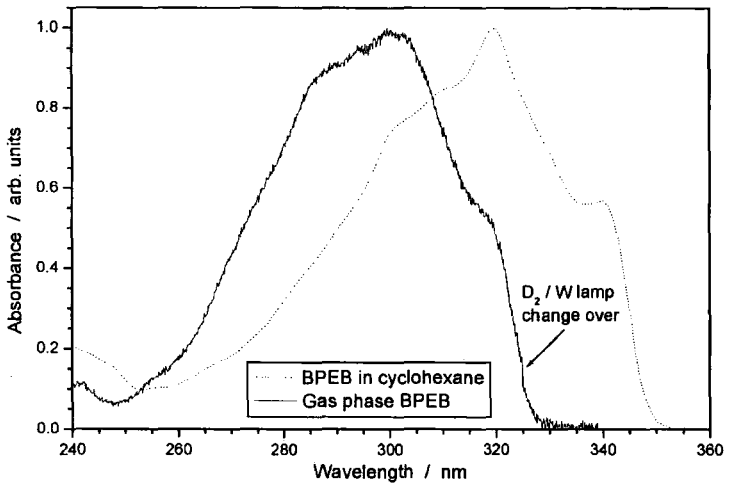

Figure 8.7: Normalized low resolution UV-Vis spectra of BPEB in cyclohexane solution (room temperature, dotted line) [93] and in the gas phase (110–130 °C, solid line).

concentration of BPEB both spectra have been normalized to aid comparison.

The absorption band of the gas phase spectrum is of comparable shape, but is shifted by –20 nm relative to the reference spectrum. Unfortunately this shift meant that our region of interest was not central to the mirrors available. It was thought that the spectrum taken in solution was red shifted due to dispersion interactions.

The BPEB sample had a slight yellow impurity (pure BPEB is white), the spectrum did not show the impurity noted by Beeby *et al.* [93] or Levitus *et al.* [155]. BPEB condensed (white) on the wall and windows of the cell, Fig. 8.8 and left behind the yellow impurity. Additional spectra showed that the BPEB condensed on the windows only caused an increase in baseline signal.

8.1.3 CRDS of BPEB

Comparing the jet cooled with the bulk gas phase spectra of tolane [94] it could be seen that the first jet cooled transitions occur under the shoulder at the lowest wavenumber end of the bulk spectrum. Thus the first investigations were targeted under the equivalent shoulder in our UV-Vis spectrum of gas phase BPEB that occurs at 320 nm. This required the dye laser to have DCM dye (300 mg/litre in MeOH, oscillator and preamplifier only, 2.7 mJ at 640 nm) which gave a wavelength

Figure 8.8: The glass cell after use for UV-Vis BPEB measurements, the white substance on the walls of the cell is re-condensed BPEB. The clear parts of the cell indicated where the heater was attached, and prevented the BPEB from condensing.

range of 602 to 660 nm (that was doubled using the SHG in the Sirah, to give a range of 301 to 330 nm (0.44 mJ at 320 nm). New mirrors (Layertec, plano-concave $R = 1$ m, $\geq$99.9% reflective between 330 and 340 nm) were fitted. They were not designed for use at 320 nm but ring-down times of $\approx$1.5 μs were achievable at this wavelength. The optical set-up was altered to take the light from the Sirah after the SHG, as shown in Fig. 8.9. The polarization of the laser light entering the cavity was vertical.

All pipe work, including the 7 micron inline filter and the nozzle used for the iodine experiment was replaced to prevent iodine contamination. With heaters on the new inline filter (now filled with BPEB) and nozzle, a range of temperatures was used to try to seed the molecular beam with BPEB whilst scanning over a wavelength range of 316 to 321 nm. Similar problems of sample re-condensing en-route to the nozzle were experienced, and as higher temperatures were used (limited by the nozzle components and the heater maximum rated temperature of 200 °C) the nozzle started to detune and no longer produced a clean pulse. Clearly a new

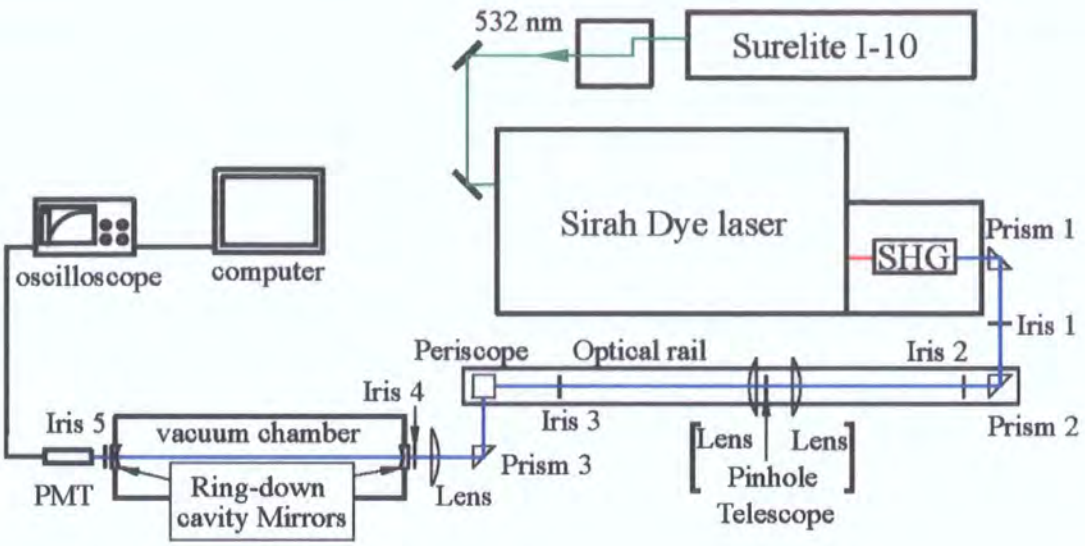

Figure 8.9: New experimental set-up for CRDS at 320 nm.

method of seeding the molecular beam and tuning the nozzle at higher temperatures was required.

Further Development

To allow the nozzle to be tuned *in situ* a frame was installed on the vacuum side of the nozzle flange. The nozzle could now be adjusted by twisting the backing gas pipe above the chamber. A further improvement to help tune the nozzle and improve the nozzle firing synchronisation was the introduction of a fast ionisation gauge (FIG) (Beam Dynamics INC., Fast Ionization Gauge, FIG-1). The FIG was mounted on a linear feedthrough, so it could be moved in and out of the beam, from one of the spare horizontal arms perpendicular to the cavity on the 6-way cross. Due to the close proximity of the FIG to the nozzle, 27–30 mm, a shielding plate with a 1 mm slit was mounted on top of the FIG to prevent detector overload. Nozzle adjustment and monitoring of the molecular beam made it possible to produce a short intense pulse (FWHM $\approx$200 μs) and obtain the correct timing.

Even with these new additions to the experiment no signal was observed using the inline filter as the beam seeding method. It was concluded the BPEB re-condensing before reaching the nozzle was preventing this seeding method from working. To get a detectable quantity of BPEB vapour into the molecular beam the sample would

have to be heated under vacuum. The inline filter, and its heater, were removed from the experimental set-up.

A 'sample oven' was designed to mount under the nozzle to heat a BPEB sample under vacuum to form a vapour cloud around the nozzle exit. The gas pulse from the nozzle would then 'pick up' the BPEB cooling it and carrying past the cavity axis. After an initial design failed, an oven (see Fig. 8.10) was adapted from a design used to study biological molecules in the gas phase [156]. The oven is a copper cylinder

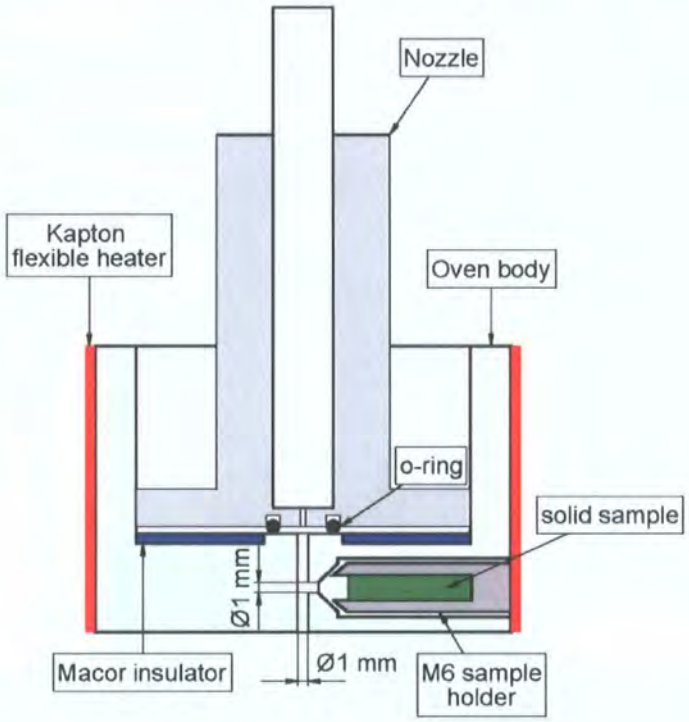

Figure 8.10: Cross section of the sample oven, showing the oven, sample holder (M6 screw), macor insulator, heater and o-ring sealing the oven to the nozzle.

with a central 1 mm diameter (exit) channel mounted directly in front of the nozzle orifice. A second 1 mm diameter channel intersects at right angles to the first, and leads to an M6 bore in the side of the oven, which houses a hollow M6 screw used to hold the sample. A Macor disc insulates the nozzle from the oven which is heated by a Kapton flexible heater (Omegalux). In this oven the BPEB vapour would be 'caught' in the exit channel so it could be picked up by the gas pulse which would expand and cool after leaving the oven. This design had the advantage of insulating the nozzle from the heater, so the gas pulse was stable and consistent.

BPEB signal was detected on the first use of this oven, but due to the cooling

effect of the gas, the BPEB was able to recondense at the top of the oven and clog up the exit of the nozzle. To prevent this the oven was slowly heated from room to operational temperature under carefully controlled conditions over two hours. This allowed repeatable BPEB spectra to be taken, although signal levels were still low.

To enhance the signal levels a 3 mm deep 40° cone was cut into the exit of the oven, Fig. 8.11, to spatially focus the beam expansion and aid in cooling. The new angular distribution of the molecular beam was $\approx 20°$ (FWHM), calculated from the size of BPEB deposits on the FIG shield. This is in comparison to a value of 11.6° (FWHM) from a custom built miniaturised nozzle with large backing gas pressures [157].

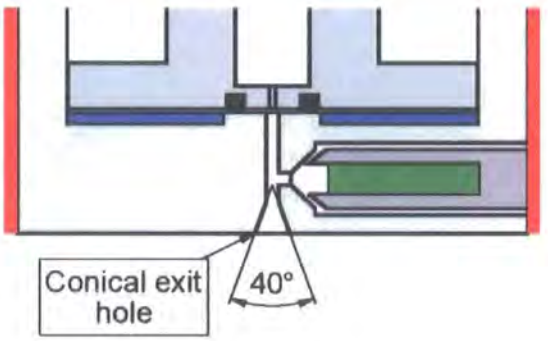

Figure 8.11: Sample oven with modified exit hole.

An interesting point to note was the timing dependence of the signal observed. Initially maximum signal was observed when the laser was timed to coincide with the maximum of the gas pulse, as measured by the FIG. Later experiments found that the maximum signal was to be found in the tail of the gas pulse. There is currently no explanation for these findings. For both sets of experiments the timing was stable as long as the nozzle produced a stable gas pulse.

Reproducible BPEB spectra could now be recorded, experimental conditions could be optimised and the range of transitions in the spectrum could be investigated.

Chapter 9

Results and Analysis

9.1 Results

To calculate the molecular absorption coefficient the ring-down time of the empty cavity is required. As the BPEB spectrum was non-discrete and occurred at the very edge of the mirrors' usable range, a mirror scan was taken for each spectrum. The mirror scan was taken under identical conditions to the spectrum, but the nozzle was miss-timed so that the laser would not intersect the molecular beam.

To facilitate analysis a good signal-to-noise ratio was required, along with a cold molecular beam to reduce spectral congestion. The signal-to-noise ratio was improved by seeding the molecular beam with a greater amount of BPEB *i.e.* by increasing the oven temperature. However, an increase in oven temperature used up the BPEB sample at a greater rate. To maintain an equal concentration of BPEB in the molecular beam care was taken to ensure that any increase in oven temperature did not exhaust the BPEB sample during a run. The maximum carrier gas backing pressure, and therefore minimum achievable beam temperature, was limited by the pumping speed of the diffusion pump. When the pressure in the chamber exceeded 1×10^{-3} mbar the molecular beam expansion had a reduced cooling effect.

Other factors also affected the temperature of the beam such as the tuning of the nozzle. Long term temperature drifts altered the timing and tuning of the nozzle over the course of a run.

The poppet in the nozzle had a direct effect upon the quality of the gas pulse, a

good quality poppet gave a sharp (FWHM $\approx$ 200 μs), stable pulse, whereas a poor quality poppet gave a wide (FWHM $\approx$ 400 μs), unstable pulse which changed in shape during short runs. The quality of a poppet determined its deformation during use, a bad quality poppet deformed to a greater extent. On several occasions, with otherwise optimised conditions, the pulse was found to be 'hot', wide and variable, this was traced to severe poppet deformation.

Optimised conditions were found to be: Oven temperature 145–155 °C, backing pressure of 4–5 bar Ar and gas pulse length with FWHM $\approx$ 200 μs. Fig. 9.1 shows a raw ring-down time spectrum taken under optimised conditions (cold) and one taken under poor conditions (hot). The relative peak heights in the spectra indicated the

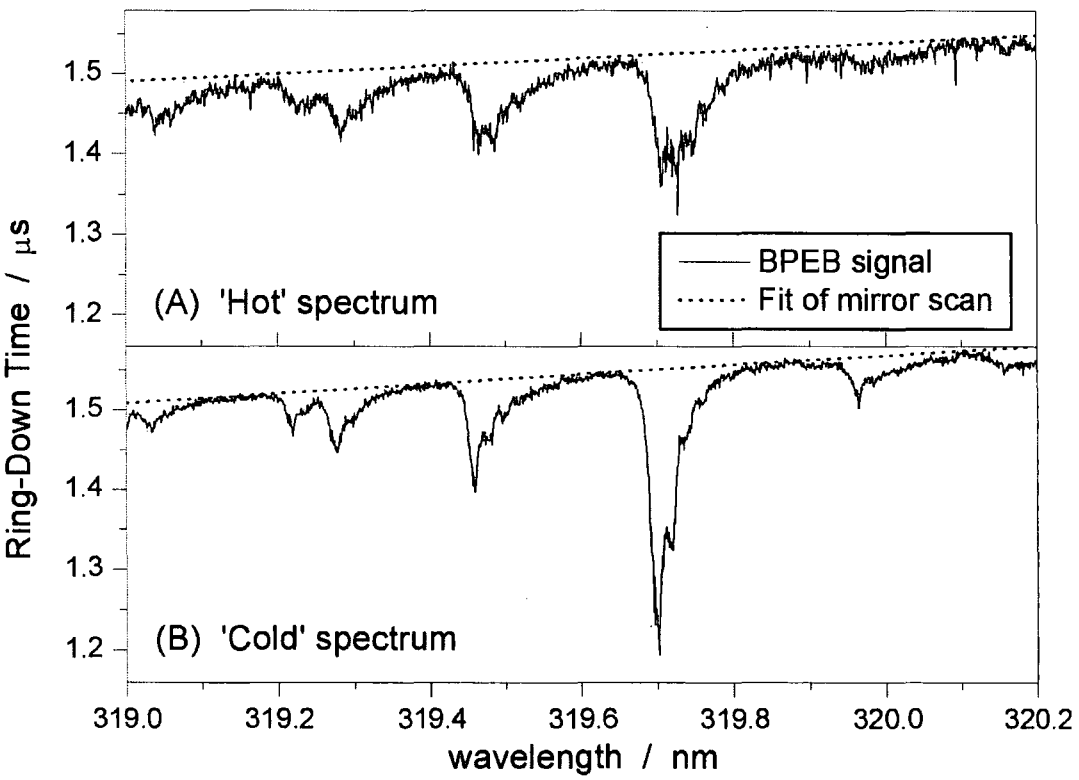

Figure 9.1: BPEB spectrum, RDT against wavelength, the dashed lines show mirror scans taken with the nozzle miss-timed.

torsional temperature, whilst the FWHM of the peaks seemed correlated to the rotational temperature and the temperature of additionally excited vibrations. It was found that the shape of the peaks was repeatable within a spectrum, but not from spectrum to spectrum, due to different beam temperatures used.

A 'cold' run showing a spectrum over the usable spectral range of the experiment

is shown in Fig. 9.2. At higher frequencies the ring-down time became shorter until any further transitions were indistinguishable from the noise floor. At lower frequencies, despite the increase in ring-down time no further transitions were observed.

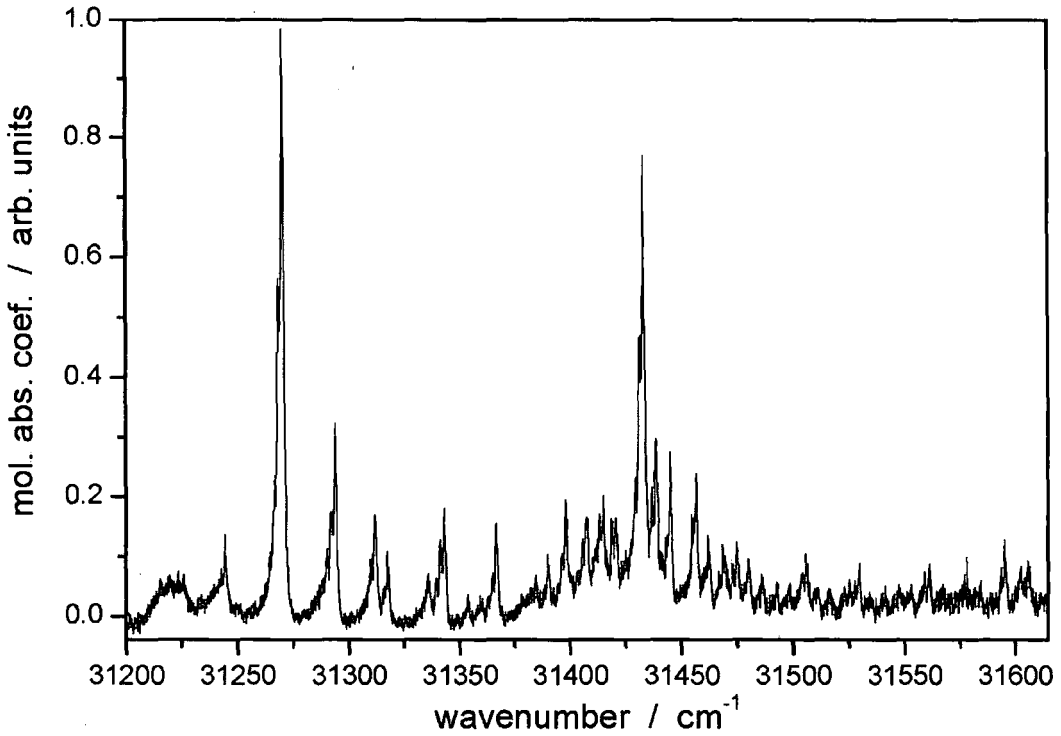

Figure 9.2: BPEB spectrum showing the full range covered by the experiment.

Different samples of BPEB (synthesised by S.R. Rutter and D.P. Lydon, Department of Chemistry, Durham) were used at different times in the experiment, no features attributable to impurities were observed and all spectra were reproducible, within the limits of experimental stability.

Calibration Checks

Due to the discrepancy found when comparing the jet-cooled iodine spectra to the simulation it was thought prudent to investigate the calibration of the laser over the range used for the BPEB spectrum. A room temperature iodine spectrum was used to check the calibration of the laser. The absorbance of iodine is very low at the wavelength range of interest so the laser set-up was altered to use a short (50 cm) cavity ring-down cell containing iodine. Iodine spectra were obtained over the wavelength range 632–641 nm and compared with simulations using the WI2

program [153]. These comparisons showed that the the dye laser calibration gave relative line positions to within ± 0.05 cm^{-1} and absolute line positions to between -0.15 and -0.31 cm^{-1}, well within the stated calibration limits of the laser.

The next section will discuss the interpretation and analysis of these spectra with regards to the torsional twisting of the BPEB molecule.

9.2 Interpreting Spectra

9.2.1 Normal Mode Analysis

Two approaches were considered for analysis of the twisting modes of BPEB. The first, found in many text books [77], uses a force constant matrix (Hessian matrix of the 2nd derivatives of the torsion potential) to describe the normal modes. The second approach follows the technique of Zheng *et al.* [100], a method specifically designed for vibrational analysis of torsional twisting modes of PPE's.

Lumped Inertia Technique

In this section the approach of Zheng *et al.* [100] is used with application to BPEB, a three ringed system. The vibrational analysis of BPEB can be simplified by modelling each phenyl ring as a rigid body with a 'lumped inertia' equal to that of the ring and its attached hydrogens (or other symmetrically located substituents). The twisting modes are described as relative rotations of these 'lumped inertias' about the principle axis of BPEB, with adjacent inertias interacting with force constants, k.

The equations of torsional motion are given in terms of the angular positions of each lumped inertia:

$$I_1\ddot{\theta}_1 = k^{(1)}(\theta_2 - \theta_1) + k^{(2)}(\theta_3 - \theta_1) \tag{9.1a}$$

$$I_2\ddot{\theta}_2 = k^{(1)}(\theta_1 - 2\theta_2 + \theta_3) \tag{9.1b}$$

$$I_3\ddot{\theta}_3 = k^{(1)}(\theta_2 - \theta_3) + k^{(2)}(\theta_1 - \theta_3) \tag{9.1c}$$

Symbolically

$$\ddot{\vec{\theta}} = \mathrm{M}\vec{\theta} \tag{9.2}$$

where θ_j is the angular position of the jth phenyl ring relative to a space fixed plane and I_j its moment of inertia about the twist axis (z axis). $k^{(l)}$ is the torsional force constant between the target ring and its lth-nearest neighbour and $\mathbf{M}$ is a 3×3 matrix (there are three rings under consideration):

$$\mathbf{M} = \begin{bmatrix} -\dfrac{(k^{(1)}+k^{(2)})}{I_1} & \dfrac{k^{(1)}}{I_1} & \dfrac{k^{(2)}}{I_1} \\ \dfrac{k^{(1)}}{I_2} & -\dfrac{2k^{(1)}}{I_2} & \dfrac{k^{(1)}}{I_2} \\ \dfrac{k^{(2)}}{I_3} & \dfrac{k^{(1)}}{I_3} & -\dfrac{(k^{(1)}+k^{(2)})}{I_3} \end{bmatrix} \tag{9.3}$$

The solution to Eqn. 9.2 is

$$\vec{\theta} = \vec{C}e^{i\omega t} \tag{9.4}$$

where $\vec{C}$ is a vector of coefficients (amplitudes of vibrations), t is time and ω is a vibrational angular frequency. It follows that

$$\mathbf{M}\vec{C} = -\omega^2\vec{C} \tag{9.5}$$

By solving the eigenvalue problem (equation 9.5) the eigenvalues, $-\omega^2$, and eigenvectors are obtained in terms of force constants $k^{(1)}$, $k^{(2)}$ and the moment of inertia I_j. $I_1 = I_3 = I_{\text{outer}}$, the moment of inertia of the outermost phenyl rings and $I_2 = I_{\text{inner}}$, the moment of inertia of the central phenyl ring.

Name	Eigenvalues	Eigenvectors		
	$-\omega^2$	C_1	C_2	C_3
Rotation	0	1	1	1
Anti-symmetric (as)	$-\dfrac{k^{(1)}+2k^{(2)}}{I_{\text{outer}}}$	-1	0	1
Symmetric (s)	$-\dfrac{k^{(1)}(2I_{\text{outer}}+I_{\text{inner}})}{I_{\text{inner}}I_{\text{outer}}}$	1	$-\dfrac{2I_{\text{outer}}}{I_{\text{inner}}}$	1

(9.6)

where $k^{(1)}$ is the force constant between a ring and its nearest neighbour. If the force constant between a ring and its second nearest neighbour, $k^{(2)}$, is not included in the eigenvalue calculation (*i.e.* only nearest neighbour interactions are considered) the anti-symmetric eigenvalue becomes $-\omega_{\text{as}}^2 = -k^{(1)}/I_{\text{outer}}$.

The eigenvalue of zero corresponds to the free rotation of the entire molecule around its z axis. The motion of the rings in the anti-symmetric and symmetric modes is shown in Fig. 9.3.

(A)

(B)

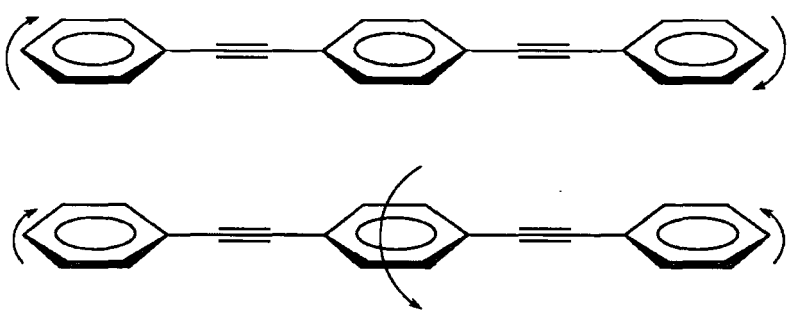

Figure 9.3: (A) Anti-symmetric and (B) Symmetric normal mode twists of BPEB.

It is important to note that the normal mode analysis using the Hessian matrix gives the same eigenvalues as the lumped inertia approach and the same eigenvector for the anti-symmetric mode. However, the eigenvectors for the symmetric mode and the free rotation are $(1, -2\sqrt{I_{\text{inner}}I_{\text{outer}}}/I_{\text{inner}}, 1)$ and $(1, 2\sqrt{I_{\text{inner}}I_{\text{outer}}}/I_{\text{outer}}, 1)$ respectively. As the free rotation eigenvector was not (1,1,1) this approach is deemed to be inferior to the lumped inertia approach.

The torsional spectra of BPEB are more complex than those of tolane [94] because of the two torsional modes. As well as vibrational progressions for each of the independent twisting modes there will also be combination bands in the spectrum.

For the simulation of the spectra (see section 9.2.4) a simple periodic potential of the form

$$V(\theta) = \frac{1}{2}V_{\text{max}}(1 - \cos 2\theta) \tag{9.7}$$

is used, where V_{max} is the torsional barrier and θ is the ring-to-ring angle. The force constant comes from the harmonic potential $V(\theta) = \frac{1}{2}k\theta^2$ and can be related to V_{max} through the 1st coefficient of the Taylor expansion of Eqn. 9.7:

$$V(\theta) = \frac{1}{2}V_{\text{max}}(2\theta^2) = V_{\text{max}}\theta^2. \tag{9.8}$$

Thus, the force constant(s) governing the interaction of the inertias are related to the pseudo-potential barrier height for rotation

$$V_{\text{max}} = \frac{1}{2}k \tag{9.9}$$

for small angular twists.

9.2.2 Simulation

In order to simulate the BPEB spectrum the torsional potentials of the two twisting modes, both in the ground and excited states, are required. The energy levels for these potentials give the line positions of the torsional transitions. The wavefunctions for each energy level are used to calculate the Franck-Condon factors, which, in combination with a Boltzmann population distribution (dependent upon the temperature of the molecular beam) are used to calculate the line strengths of the transitions.

Energy Levels and Wavefunctions

The energy levels and wavefunctions for the BPEB twisting modes are solutions of the one-dimensional Schrödinger equation

$$\left[-\frac{\hbar^2}{2I_{\text{red}}}\frac{d^2}{d\theta^2} + V(\theta)\right]\Psi(\theta) = E\Psi(\theta) \tag{9.10}$$

where V is a periodic potential for the torsional motion. This problem has been well treated by Lewis *et al.* [158], and the following description follows their approach.

The wavefunction, $\Psi(\theta)$ for a given torsional vibrational level, v, with the boundary condition $\Psi(\theta) = \Psi(\theta + 2\pi)$, is described by a linear combination of periodical basis functions $\psi_i(\theta)$

$$\Psi_v(\theta) = \sum_i^N a_{iv}\psi_i(\theta) \tag{9.11}$$

The basis set,

$$\psi_m = (2\pi)^{-\frac{1}{2}}\mathrm{e}^{\mathrm{i}m\theta} \qquad m = 0, \pm1, \pm2, ...$$

may also be expressed as real functions

$$\begin{aligned} \psi_n^{\text{even}} &= \pi^{-\frac{1}{2}}\cos n\theta \qquad n = 1, 2, ... \\ \psi_0^{\text{even}} &= (2\pi)^{-\frac{1}{2}} \\ \psi_n^{\text{odd}} &= \pi^{-\frac{1}{2}}\sin n\theta \qquad n = 1, 2, ... \end{aligned} \tag{9.12}$$

using cos and sin bases to preserve even and odd symmetry, as these functions are periodic they will satisfy the boundary condition of the wavefunction. These basis

functions are used to construct the Hamiltonian matrix

$$H_{kl} = \int_0^{2\pi} \psi_k^* \hat{H} \psi_l d\theta \tag{9.13}$$

for the Schrödinger equation in matrix representation

$$H\vec{a} = E\vec{a} \tag{9.14}$$

the solution of which yields both the eigenvalues, energies E_v, and eigenvectors, $\vec{a}_v$, which are used to express the wavefunctions using equation 9.11.

Near the bottom of the potential well the energy levels are doubly degenerate; near the top of the barrier the levels split apart because of the tunnelling through the barrier, and above the barrier the levels rearrange to form different doubly degenerate pairs [158].

Line Strengths

The energy levels of the torsions allow the calculation of spectral line positions. The intensities of these vibrational lines are determined by two factors, (i) the square of the transition moment integral and (ii) the population of the vibrational levels.

The transition moment integral is the product of the electronic transition dipole moment, $\vec{R}_e$ and the vibrational overlap integral

$$\langle v' \mid v'' \rangle = \int_0^{2\pi} \psi_{v'}^* \psi_{v''} d\theta = \sum_i a_i' a_i''. \tag{9.15}$$

If $\vec{R}_e$ is assumed to be constant (with twist angle θ) then the transition intensity is proportional to $|\langle \nu' \mid \nu'' \rangle|^2$, known as the Franck-Condon factor. These factors are calculated using the eigenvectors derived from the torsional potentials [158]. Due to the symmetry of the wavefunctions only even-even and odd-odd transitions occur.

The populations of the ground state potentials are calculated using a Boltzmann distribution

$$\frac{n_v}{n_0} = \exp\left(-\frac{G(v) - G(0)}{k_B T}\right) \tag{9.16}$$

where n_v and n_0 are the populations of the v-th and $v = 0$ vibrational states which have energies of $G(\nu)$ and $G(0)$ respectively. T is the temperature of the molecular beam.

For transitions within a single twisting mode the relative line strengths are given by the products of the Franck-Condon factors and the populations of the ground state. However, for transitions that are a combination of both twisting modes the product of the separate modes' line strengths is taken; this accounts for the relative populations and wavefunction overlaps of the different modes.

Band Simulation

An initial attempt to simulate the band shape with a prolate top did not reproduce the experimental band shape as it was far too narrow. The band is assumed to be a combination of rotations and a low frequency vibrational mode such as a whole molecule bend. It turned out that the band could be simulated with a pseudo-vibrational progression at each torsional line position, as shown in Fig. 9.4.

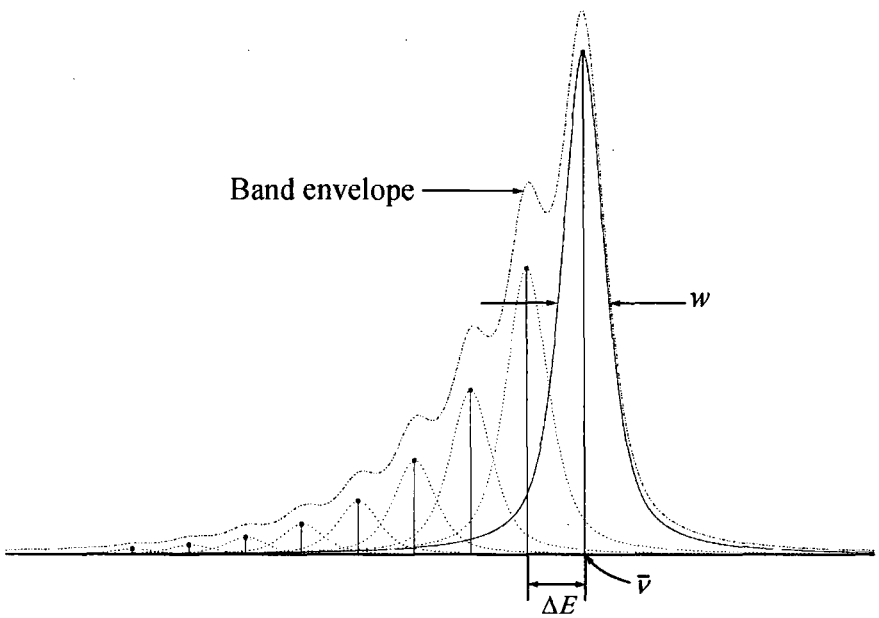

Figure 9.4: Simulation of a spectral band of the BPEB spectrum, showing the constituent peak heights (dots) and their profiles (dotted lines), the profile of the peak at the origin (the torsional line position ν) indicates its FWHM, w. The peaks are separated by the energy difference of the pseudo-vibrational levels, ΔE. The band envelope is shown with a dash-dotted line.

The constituent peak heights are given by a Boltzmann distribution

$$h_p = \exp\left\{-\frac{p\Delta E}{k_B T}\right\} \tag{9.17}$$

where ΔE is the energy separation of the pseudo-vibrational levels, p is the quantum number of the level and T is the temperature of the pseudo-vibration (not the same as the torsional temperature). Each constituent peak is simulated by a Gaussian and Lorentzian profile with a FWHM w:

$$f(\bar{\nu}) = g \cdot \exp\left\{(-4\ln 2)\left(\frac{\bar{\nu} + p\Delta E}{w}\right)^2\right\} + (1-g)\frac{w^2}{4(\bar{\nu} + p\Delta E)^2 + w^2} \qquad (9.18)$$

where $\bar{\nu}$ is the torsional line position and g controls the Gaussian character of the profile. The full band profile is given by

$$B(\bar{\nu}) = \sum_{p=0}^{p(\max)} h_p \cdot f(\bar{\nu}) \qquad (9.19)$$

The Gaussian character of the profiles, temperature, peak FWHM and the energy separation of the levels were altered to give the best fit, by eye, to the bands observed in the spectrum.

In order to interpret and assign the BPEB spectrum, a program to calculate line positions and simulate the spectrum was written by E. Wrede that implemented the procedures described above.

9.2.3 BPEB Theory

The BPEB spectrum shows a large number of transitions whose assignments are not obvious, even with combination differences. Indeed it was uncertain that they were torsional progressions. A first approach was to use computational methods to calculate the torsional potentials.

Density functional theory (DFT) calculations were carried out using the Gaussian 98 package [159] with Pople's 6-31G basis set supplemented by one d-function on heavy atoms and p-polarisation functions on the hydrogens and with (and without) additional diffuse functions on the heavy atoms. The DFT calculations were carried out using Becke's three-parameter hybrid exchange functional [160] with Lee–Yang–Parr gradient-corrected correlation functional (B3LYP)[161].

Ground State

The ground state geometry of BPEB was optimised [162, 163, 164, 165] using B3LYP/6-31G** with no constraints applied to bond lengths, angles or dihedral

angles, *i.e.* a full geometry optimization. The results are shown in comparison with X-ray single crystal data [166] in Table 9.1. The calculations confirm the molecule to be planar with D_{2h} symmetry. The slight differences between the crystal structure and the DFT optimized structure are thought to be due to the effects of packing arrangements in the solid phase. The moments of inertia required for the

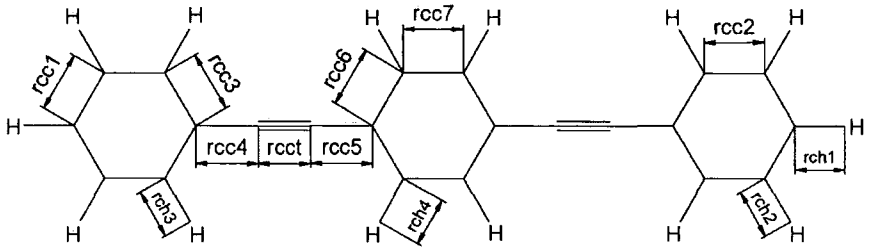

Figure 9.5: Bond length labelling used in DFT calculations and Table 9.1.

Hamiltonian matrix in the Schrödinger equation (Eqn. 9.10) were obtained from the B3LYP/6-31G** optimized geometry of BPEB at 0°.

Torsional Potentials

To obtain the torsional potentials of BPEB in the symmetric and anti-symmetric modes, further calculations at the B3LYP/6-31G** level of theory were used. The geometry was again allowed to fully optimise, apart from the ring-to-ring dihedral angle which was fixed according to a grid of points over the torsional angle, θ. An angular grid with 5° spacing was used up to 70° with additional points at 0.1°, 1°, 3°, 80° and 90°.

The DFT potential points are shown in Fig. 9.6 together with a fit to Eqn. 9.7, where the torsional potential barrier height, $V_{\max}$, was given by the relative energy of the 90° to the 0.1° geometry. The $\theta = 0°$ geometry point was excluded as it had an energy 6.26 cm^{-1} below the energy of the 0.1° geometry, which made no physical sense and is believed to be an artefact of the calculation methodology. The points were also fitted with a Spline function for use in the simulation program.

Allowing all parameters but the torsional angle to optimise shows that the ring-to-ring distance increases by 0.0092 Å (or 0.2%) on twisting from 0° to 90°. No

Bond	X-ray [166]	6-31G**	6-31+G(d,p)	6-311G(2d,p) [167]
rch1	1.14 Å	1.0859 Å	1.086 Å	
rch2	1.14	1.086	1.0861	
rch3	1.14	1.0851	1.0852	
rch4	1.14	1.0849	1.0851	
rcc1	1.3825	1.397	1.3987	1.392 Å
rcc2	1.3805	1.3916	1.3937	1.386
rcc3	1.397	1.4097	1.4108	1.404
rcc4	1.431	1.4242	1.4258	1.423
rcc5	1.428	1.4219	1.4235	1.420
rcct	1.205	1.2171	1.2185	1.208
rcc6	1.401	1.4109	1.4118	1.405
rcc7	1.376	1.3865	1.3886	1.381
twist 1	0°	0°	0°	
twist 2	0	0	0	

Table 9.1: Comparison of X-ray single crystal diffraction structures [166] with Gaussian calculations at the 6-31G**, 6-31+G(d,p) and 6-311G(2d,p) [167] levels. A key to the bond length labels is shown in Fig. 9.5. The twist angles at the bottom of the table are the ring to ring twist angles of the outer rings relative to the middle ring.

evidence was found for a ring breathing mode being coupled with the twisting modes (the largest ring carbon-carbon bond length change was 0.1% from planar to perpendicular geometry), as suggested by Zheng *et al.* [100]. If the molecule is not allowed to optimise at each twist angle then the resultant potential is distorted.

Excited State

The optimised geometries of the ground state at each angle were used to calculate the energies required to excite the molecule to the 1st three singlet excited states. The calculations were carried out using the Time Dependent DFT (TD-DFT) methodology [168, 169, 170] at the B3LYP/6-31G** level of theory.

The excitation energy plus the ground state energy allowed the calculation of torsional potentials for the 1st two Singlet excited states, Figs. 9.7 and 9.8. An inter-

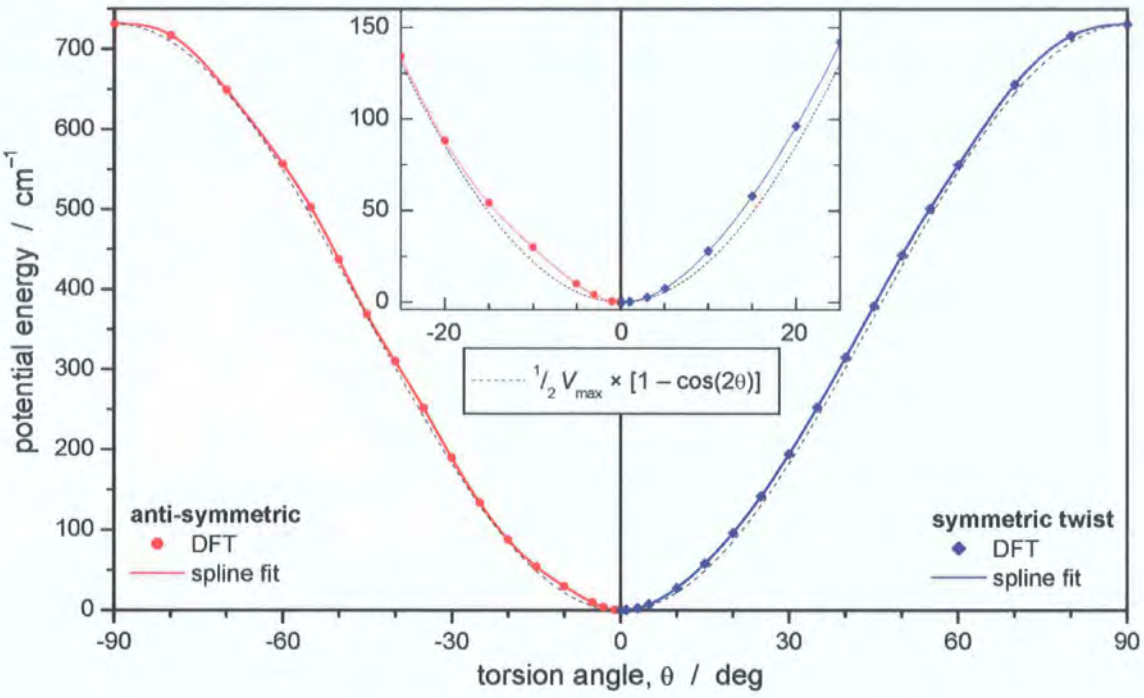

Figure 9.6: Ground state torsional potentials for the anti-symmetric and symmetric twisting modes. Calculated DFT energies are shown as points fitted with a spline function and compared with a fit to Eqn. 9.7. Note that whilst both modes have the same minima and barrier height, they have different shapes especially at low torsion angles, as can be seen in the inset panel.

esting observation was the crossing/avoided crossing of these two states at around 80° which will affect the energy levels at the top of the first excited state. The Gaussian program failed to determine the symmetry of the excited states, thus the nature of the crossing (true or avoided) could not be ascertained. The first excited state appears to be approximately eight times as steep as the ground state, but the relative V_{max} values cannot be accurately compared due to the uncertanty caused by the crossing/avoided crossing. The second excited state has a local maximum at its planar geometry, and minima at 35° and 25° for the symmetric and anti-symmetric twists respectively. The spectroscopy of the second excited state is expected to be markedly different to the current study.

Using DFT Potentials in Simulation

For the first attempt to simulate the BPEB spectrum, spline fits to both the ground and excited state DFT potentials were used. This approach failed to simulate any of the experimental peaks. A second simulation was attempted using only spline fits

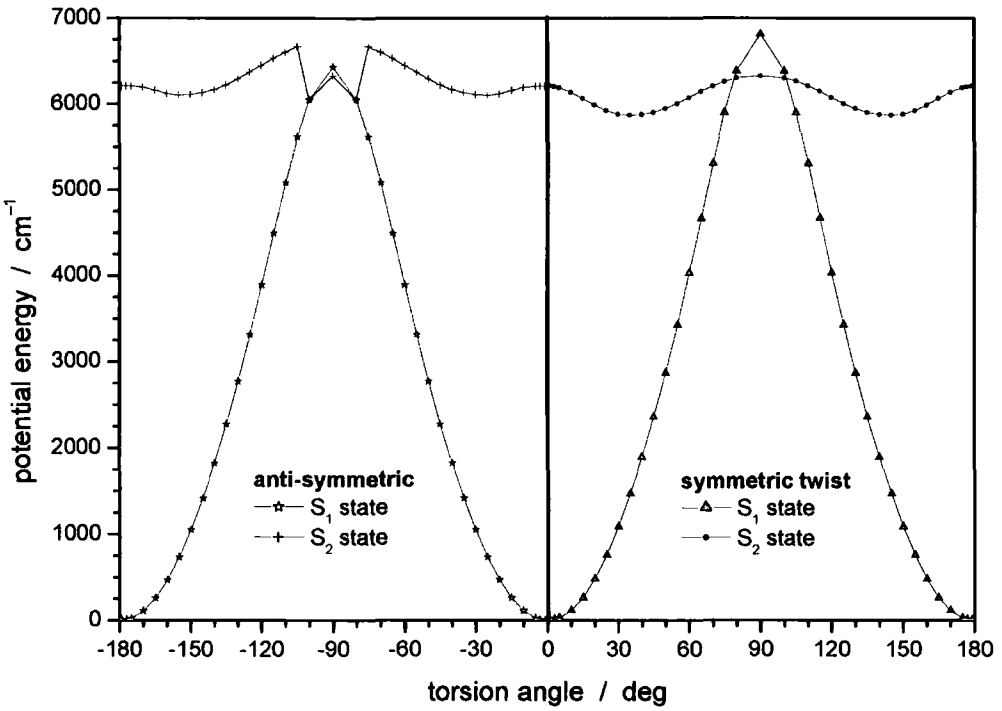

Figure 9.7: The 1st two singlet excited states of BPEB, symmetric and anti-symmetric torsional potentials. Calculated DFT points are connected by straight lines. Note the crossing/avoided crossing of these two states at around 80°.

to the ground state DFT potentials. The excited state potentials were calculated by a user defined scaling of the ground state potentials to achieve the best fit, by eye, to the spectrum. A scaling factor of approximately 2.5 gave the best result, matching the band origin and up to the next three peaks. For tolane a scaling factor of eight between the ground state (which had a barrier height of 202 cm^{-1}) and the excited state was quoted [94]. The ground state DFT barrier (731 cm^{-1}) of BPEB is over three and a half times that of tolane, with only the addition of one extra phenyl ring to increase the strength of the π-conjugation. The extremely poor fit of the spectrum and comparison to tolane led to the conclusion that the DFT derived potentials were of no use in describing the torsional motion of BPEB.

The construction of the DFT potentials involved the calculation of very small differences between the sixth and ninth significant figure of the total energy of the molecule. Such numerical accuracy was of vital importance, and may have had serious implications on the size and shape of the torsional potentials. Also, DFT

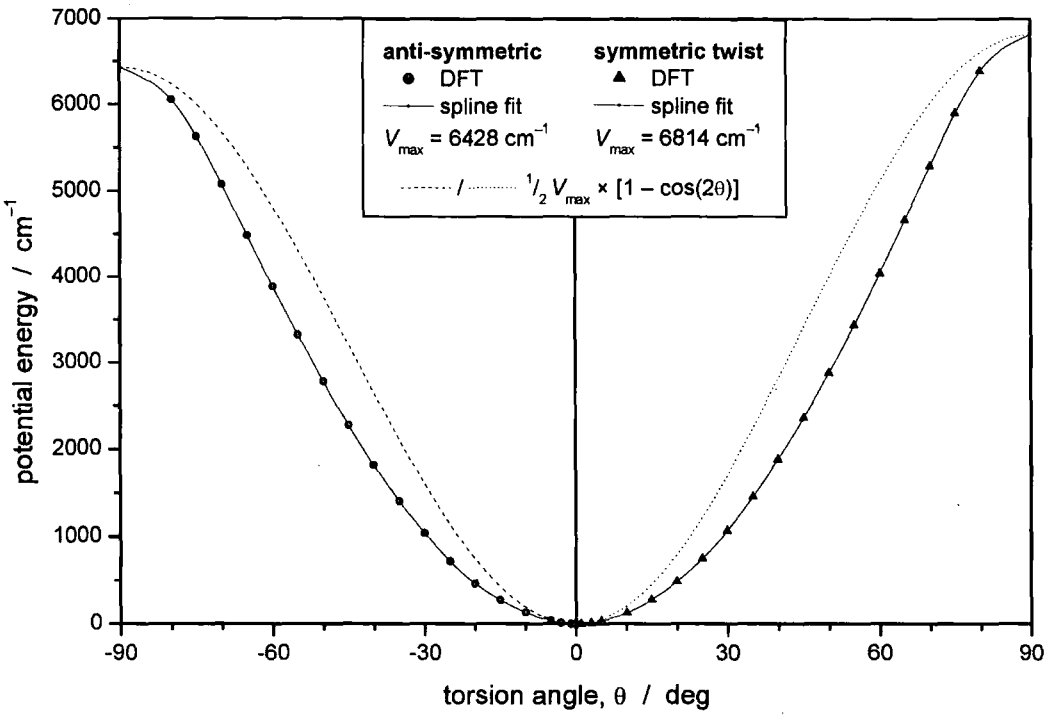

Figure 9.8: 1st singlet excited state torsional potentials for the anti-symmetric and symmetric modes. Calculated DFT points are fitted with a spline function and shown in comparison to the simple periodic function 9.7.

may not be very good at describing the π-bond breaking effects experienced by conjugated molecules undergoing torsional motion [171].

9.2.4 Back to Basics

Whilst the largest peak in the spectrum can be assigned as the ($v'_s v'_{as} \leftarrow v''_s v''_{as}$) 00←00 band (this band would have the highest population and the largest Franck-Condon factor and therefore the greatest line strength), assignment based on combination differences is ambiguous. Clarification of the spectrum is required, in particular knowledge of the assignment of the two different twisting modes.

Middle Ring Deuterated BPEB

Isotopic substitution is a well known technique for the elucidation of complex spectra. The difference between the twisting motion of the symmetric and the anti-symmetric modes is the participation of the central phenyl ring. With the hydrogens

on the central ring replaced with deuteriums (Fig. 9.9), the peaks in the spectrum resulting from the symmetric twisting mode (and any other vibrations that move the middle ring) change their positions. Whereas the peaks resulting exclusively from the anti-symmetric mode remain in the same relative positions.

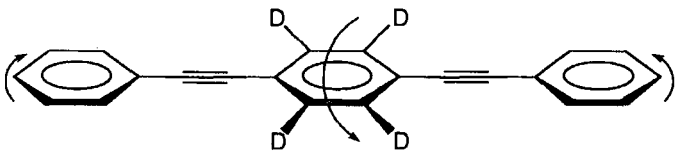

Figure 9.9: D-BPEB symmetric twisting mode.

The spectrum of 1, 4-bis(phenylethynyl)-2,3,5,6-tetradeuterobenzene, from here on known as D-BPEB, was recorded and compared with BPEB, see Fig. 9.10. D. P. Lydon prepared the selectively deuterated compound D-BPEB (Department of Chemistry, Durham).

Experimental Potentials

At this stage it was realised that the two hot bands could be assumed to correspond to the 0←2 transitions of the symmetric and anti-symmetric modes. The hot band's separation from the 00←00 band corresponds to $2\nu_e$ for each twisting mode (where ν_e is the harmonic vibrational constant). ν_e is related to the force constant for a nearest neighbour ring twist through

$$\nu_e = \frac{1}{2\pi}\sqrt{\frac{k}{I_{red}}} \tag{9.20}$$

which gives a value for k. This was used with eqn. 9.9 to give a value of V_{max}, which allowed new ground state potentials to be constructed using eqn. 9.7. Excited state potentials were assumed to be scaled versions of the ground state potentials, with barrier heights $\approx 8 \times V_{\text{max}}$, analogous to tolane [94].

New simulations created using these potentials allowed the values of V_{max} to be optimised so that the simulation matched, by eye, the two hot bands. The values of V_{max} obtained were 222.82 cm^{-1} for the anti-symmetric and 232.7 cm^{-1} for the symmetric twist, which are very similar to the equivalent value of 202 cm^{-1} for tolane [94]. These values made the simulation a good fit of the whole spectrum,

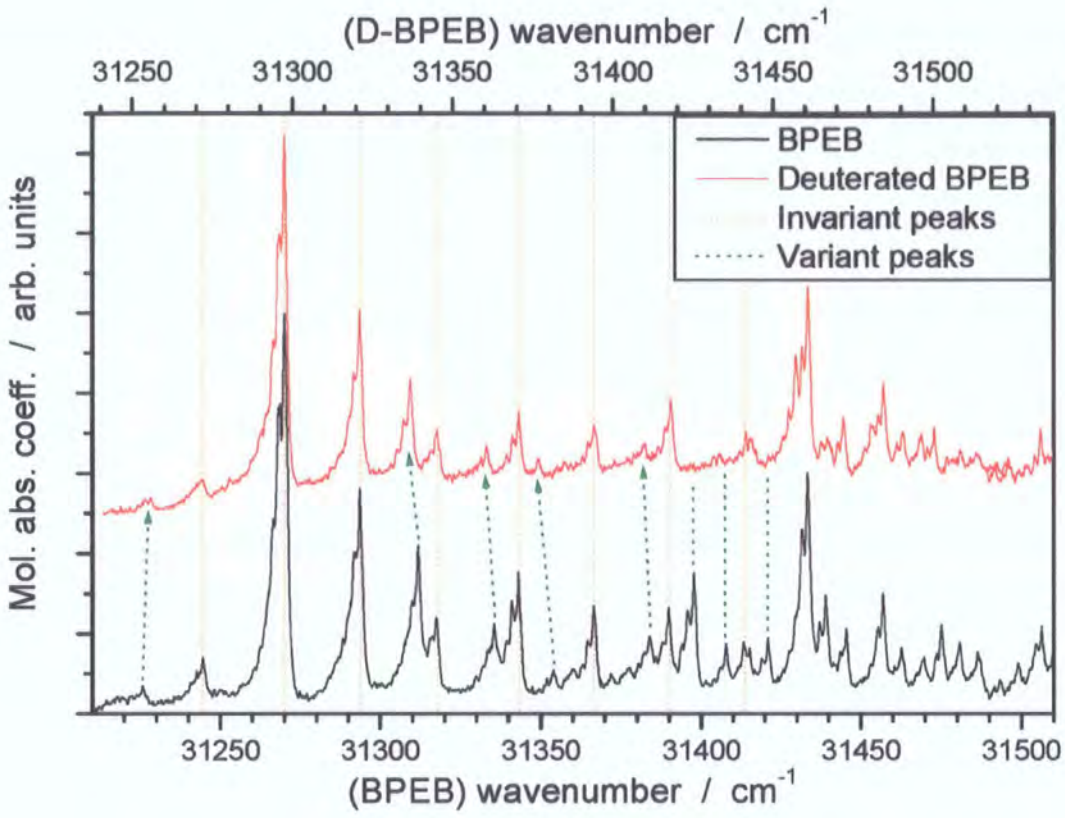

Figure 9.10: Comparison of a BPEB spectrum with a D-BPEB spectrum. The D-BPEB spectrum has been shifted on the x-axis so that the band heads of both spectra line up and shifted up on the y-axis for ease of comparison. The peaks due to the anti-symmetric mode have the same relative spacing, while peaks with a contribution from the symmetric mode have been shifted by the deuteration of the middle ring.

which was optimised by varying the scaling factors of upper states and the torsional temperature.

The barrier heights of the ground state potentials of the two modes should be the same, as the energy of the molecule will be fixed with a rotation angle of 90°. However the spectrum is only sensitive to the bottom third of the potential, so $V_{\max}$ does not represent the true barrier height, but defines the shape of the potential at the bottom. The difference in potential shapes is justified by the normal mode analysis, which shows that the anti-symmetric mode has an additional force constant for next nearest neighbour interaction, see Eqn. 9.6. This can be understood as a difference in the long range π-interactions due to the differing orbital overlaps during the twisting motion of the two modes.

9.2.5 Comparison

It was now possible to assign the BPEB spectrum using the simulation, Fig. 9.11 (A). Furthermore the D-BPEB spectrum was assigned by changing only the inertia of the inner ring in the simulation program, Fig. 9.11 (B). The parameters used to simulate both spectra are shown in Table 9.2.

Simulation parameter	**BPEB**	**D-BPEB**
T_{torsion} / K	40 ± 1	33 ± 1
V_{max}(as) / cm^{-1}	222.82	222.82
V_{max}(s) / cm^{-1}	232.76	232.76
excited state scaling factor (as)	8.0 ± 0.05	8.05 ± 0.05
excited state scaling factor (s)	8.0 ± 0.05	8.0 ± 0.05
band simulation temperature / K	5 ± 0.5	4.5 ± 0.5
additional progressions	**position / cm^{-1}**	**intensity**
BPEB 1	72.9	0.15
BPEB 2	127.6	0.2
BPEB 3	163.2	0.45
D-BPEB 1	72.9	0.07
D-BPEB 2	163.5	0.45

Table 9.2: BPEB spectrum simulation parameters, including the positions, relative to the 00←00 band, and relative intensities of additional torsional progressions.

It can be seen from Fig. 9.11 that a single torsional progression fits the early part of the spectrum very well, but does not fully describe the experimental spectrum. Additional torsional progressions, shown as ladders in the plots, were required to simulate the missing intensity, their properties are shown in Table 9.2. These extra torsional progressions may originate from other low frequency vibrational modes. The extra intensity required in the spectra may not come from extra progressions, but the fit is improved with their inclusion.

A full simulation with all of these additional progressions added on is shown in comparison with the experimental spectrum of BPEB in Fig. 9.12. The peak positions were very well reproduced, and the peak intensities reasonably well. Ex-

perimental intensities may be inaccurate due to an instability of the nozzle which resulted in a change in BPEB density in the beam, and beam temperature, during the scan.

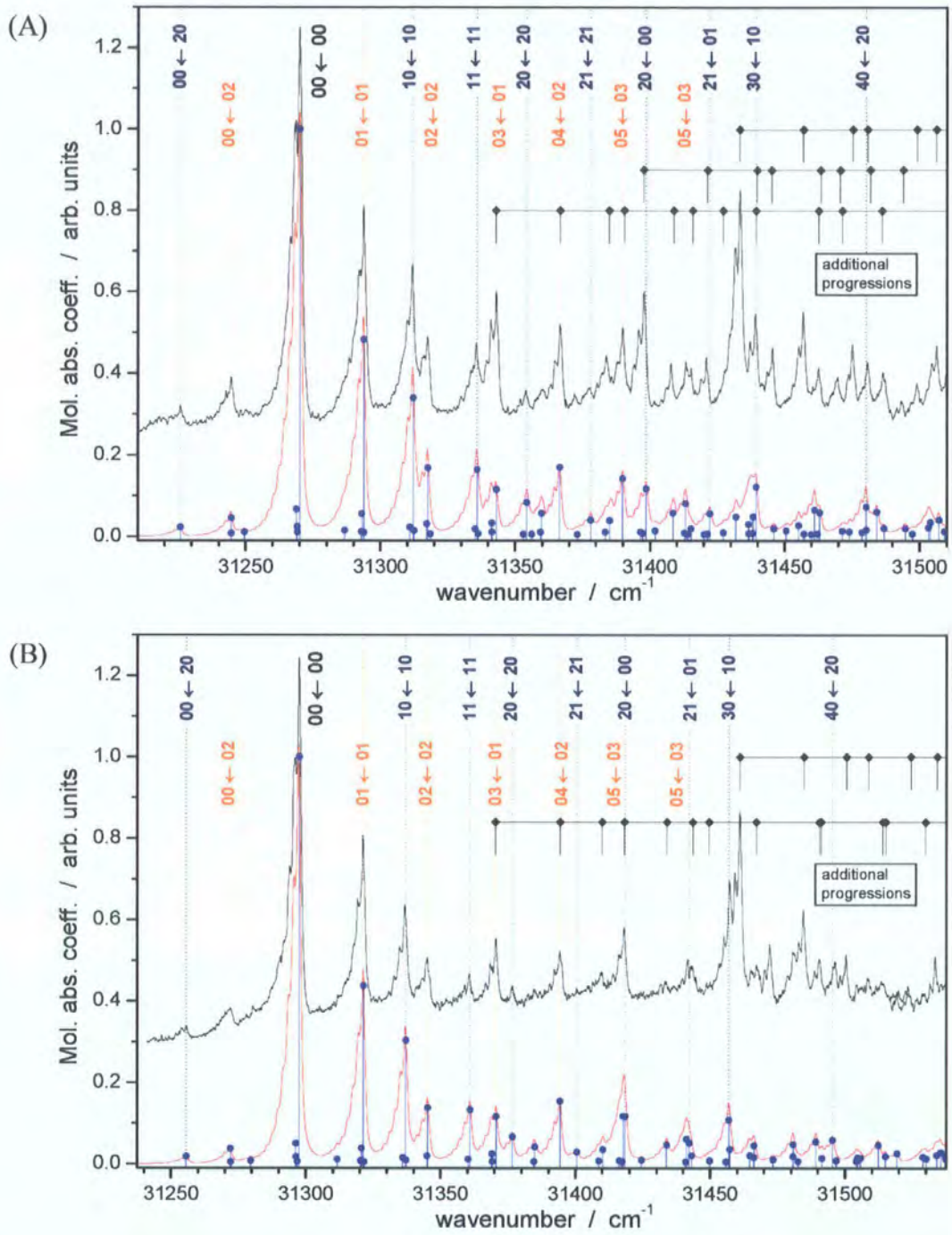

Figure 9.11: Comparison of experimental (black line) and simulated (red line) spectra for (A) BPEB and (B) D-BPEB. An offset has been added to the experimental spectra to ease comparison. The transitions are shown as vertical blue lines with intensities shown by points. The most intense transitions are labelled at the top of the plot, symmetric transitions in blue and anti-symmetric transitions in orange, both with dashed vertical lines to guide the eye. Parameters for both simulations are shown in table 9.2. The locations of additional torsional progressions originating from other vibrational modes are shown with ladders starting at the position of the 00←00 transition (see text). See also Figs. D.1 and D.2 in appendix D.

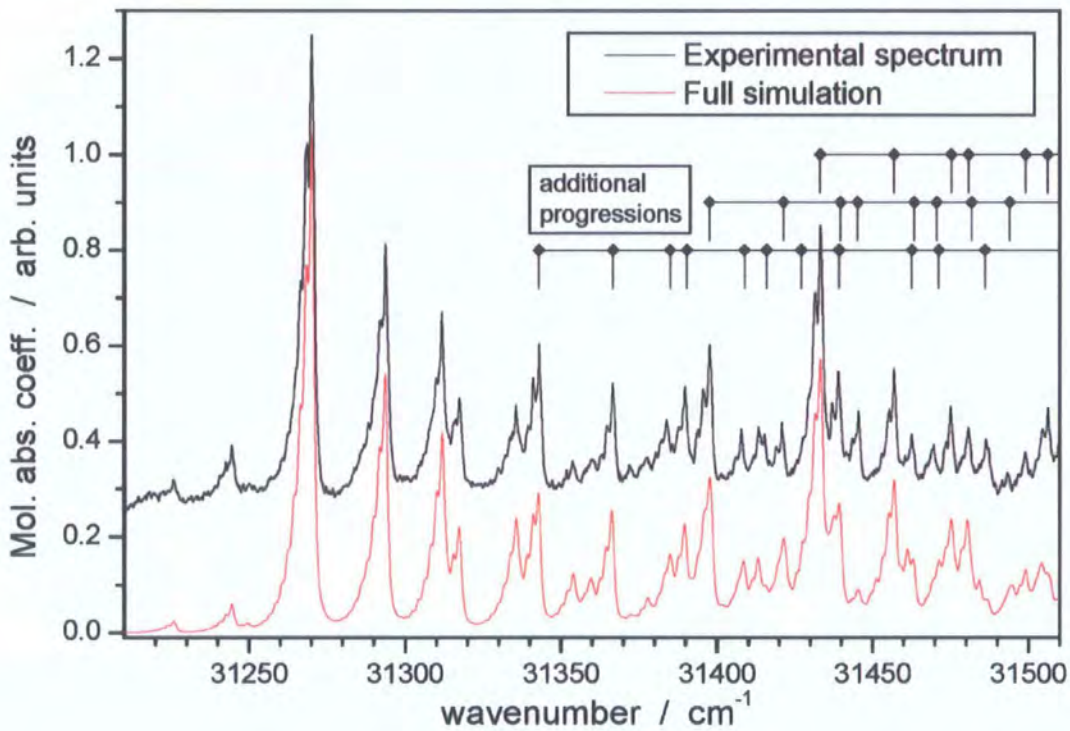

Figure 9.12: Comparison of experimental (black line) and simulated (red line) spectra for BPEB, the simulated spectrum includes the contributions from the additional torsional progressions that are indicated by ladders starting at the position of the 00 transition (see text). An offset has been added to the experimental spectrum to ease comparison.

9.3 Conclusions

A sensitive CRDS apparatus for use with molecular beams has been designed, built and tested. An oven used to seed a molecular beam with a high melting point solid has been adapted and tested. The CRDS experiment has been used to obtain high resolution absorption spectra of jet-cooled BPEB. Individual torsional transitions within the $\pi^* \leftarrow \pi$ electrical transition were resolved. Spectral lines resulting from the symmetric twisting mode were identified by isotopic substitution of the hydrogens on the central ring (D-BPEB).

BPEB and D-BPEB spectra were successfully simulated using a simple periodic potential (eqn. 9.7), as was used for Tolane [94]. The peak positions were very well reproduced, as were the peak intensities for the early part of the spectrum, confirming the spectral assignment as a torsional mode. Additional torsional progressions, possibly originating from other low frequency vibrational modes, were required to simulate the missing intensity.

The spectroscopically derived potential barrier height, V_{max}, was estimated to be 220–235 cm^{-1}. However, the recorded spectra are only sensitive to the bottom third of the potential, so V_{max} does not represent the true barrier height, but defines the shape of the potential at the bottom.

This experimental finding is in stark contrast to the results from DFT calculations which gave a torsional barrier height of 731 cm^{-1}. Numerical inaccuracy, as well as an inability to correctly describe the π-bond breaking effects experienced by conjugated molecules during torsional motion [171], may have prevented DFT from producing an accurate potential. However, the shapes of the DFT ground state potentials show only small deviations from a simple periodic function (Fig. 9.6). The difference between the shapes of the symmetric and anti-symmetric DFT potentials at low angular displacements was rationalised by the different long range π-interactions of the two modes, this was also implied by the different experimental V_{max} values of the two modes. These findings are consistent with the normal mode analysis, which shows that the anti-symmetric mode has an additional force constant for next-nearest-neighbour-interaction (Eqn. 9.6).

The experimentally estimated torsional barrier height is very similar to the equiv-

alent value of 202 cm^{-1} for Tolane, as are the scaling factors between the ground and excited states [94]. The similarity of these values indicate that the additional long range π-conjugation in the three ring system, BPEB, only has a small additional stiffening effect on the torsional motion, as was concluded by a theoretical study of 2–6 ring poly(phenyleneethynylene)s [100].

Furthermore, the DFT calculations suggest a crossing/avoided crossing between the 1^{st} and 2^{nd} singlet excited states near the maximum of the 1^{st} excited state torsion potential (Fig. 9.7). The second excited state has a local maximum at its planar geometry. The spectroscopy of the second excited state is expected to be markedly different to the current study, and may have implications for the development of switching molecules.

9.4 Further Work

Modifications of the experiment and suggestions of new molecules to study are given below, but there is still more that can be achieved using the current experimental set-up. It would be beneficial to study the jet cooled spectrum of BPEB using sets of mirrors spectrally matched to the full range of its near-UV absorption bands, especially as it is proposed that the maximum of the low resolution hot gas phase spectrum of BPEB (Fig. 8.7) near 300 nm is due to transitions to the 2^{nd} singlet excited state of BPEB. Using the estimate for the 1^{st} excited state barrier height ($8\times$(220 or 235) and the $00\leftarrow00$ band position, the 1^{st} and 2^{nd} excited state crossing/avoided crossing should occur at $\approx$300 nm.

As the 2^{nd} excited state has a minimum at 25° and 35° for the anti-symmetric and symmetric modes respectively, as well as a crossing/avoided crossing, the absorption spectrum is expected to be quite different to that recorded here, and may give an insight to possible switching applications. The spectrum would also allow investigation of the state crossing to ascertain its nature.

9.4.1 Experimental Development

A potential improvement of the experimental set-up would be an iterative investigation of the design of the sample oven. To gauge the effect of oven design the Iodine set-up (with the addition of the oven on the underside of the nozzle), discussed in section 8.1.1, could be used to determine the molecular beam temperature. Two modifications should be investigated; (i): the length of the 40° cone in the oven. (ii): the effect of an additional sample holder, which would increase the amount of BPEB seeded into the beam at the current optimum temperature, or allow lower temperatures to be used. Comparison of 0° and 90° polarised light spectra of BPEB would indicate the extent of BPEB alignment in the molecular beam.

The maximum backing pressure, and therefore beam cooling effect, was limited by the pumping speed of the diffusion pump. A greater available pumping speed would allow greater control of the beam conditions.

New Experimental Designs

The previously mentioned LIF technique (section 7.2) is background free, but requires a calibration procedure to make the transition intensities acquired absolute. Hybrid LIF-CRDS experiments have been developed which avoid this calibration procedure; these can also provide more detailed information about the system being studied from comparison of the equivalent spectra.

Two approaches have been reported for this hybrid experiment. The first, demonstrated by Spaanjaars *et al.* [172], used the usual LIF set-up but with a ring-down cavity at a small angle to the LIF pump axis. The input laser was split into a low intensity beam for the CRD measurement and a high intensity beam for the LIF experiment. The comparison of the resultant spectra demonstrated the strong rotational dependence of the predissociation in the $\nu' = 3$ state of OH.

A second approach, using a common CRDS and LIF axis, has been demonstrated with the high intracavity power available in CW-CRDS [125, 117] The LIF signal was accumulated perpendicular to the cavity over the full ring-down time. If a pulsed laser source was used then only a very small percentage ($< 0.1\%$) of the incident light would be coupled into the RDC, but the multiple passes through the

sample could result in a LIF spectrum of comparable quality to that obtained by a single pass of the entire beam through the sample [119]. A potential advantage of using a pulsed source is that the LIF-CRDS spectrum will be much less prone to saturation effects due to the low laser intensity in the cavity.

9.4.2 Target Molecules

There are many molecules for which the torsional motion is important and where study of this motion could provide valuable insight. Generally, it will be easier to study symmetrical molecules as their spectral assignment will be simple, whereas asymmetrical molecules exhibit coupling between torsional and other vibrational modes [100].

BPEB Derivatives

An obvious starting place for new molecules to study are the derivatives of BPEB, such as perdeuterated BPEB. The model used here should apply with only a change in moments of inertia, this would be another test of the validity of the current model. Perfluoronated BPEB could be used to demonstrate the effect of electron withdrawing groups upon the torsional potentials.

Another area of study could be BPEB with (symmetrical) bulky substituents to investigate how steric interactions affect the torsional motions. Several BPEB derivatives of this kind have recently been synthesised and studied by A. Beeby's group (Department of Chemistry, University of Durham). One molecule of particular interest is 1, 4-bis(2,4,6-tri*tert*butylphenylethynyl)-2,3,5,6-tetramethylbenzene (Fig. 9.13) whose ground state geometry has the middle ring twisted at 90° relative to the other rings [173]. The ground and excited state torsional potentials of this molecule

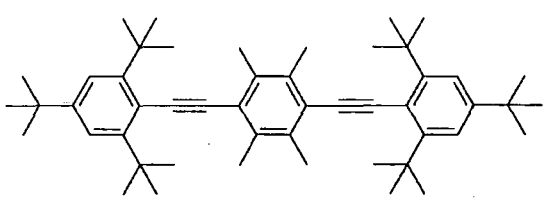

Figure 9.13: 1, 4-bis(2,4,6-tri*tert*butylphenylethynyl)-2,3,5,6-tetramethylbenzene.

are of particular interest as it is thought that the ground state potential minimum corresponds to an excited state maximum which has implications for the design of molecular switches.

Molecular Wire Candidates

There are also many other types of molecule under consideration as potential molecular wires or organic light emitting devices, in which the torsional motion is of importance. Longer PPE's are of interest [92], as are hydrocarbon systems with alternate single and triple bonds between rings [100]. Systems with atoms other than carbon in the rings are also under investigation *e.g.* thiophenes [87, 88, 89], and di(aryleneethynyl)-pyrazine derivatives [167].

Appendix A

Quasi-Classical Trajectory Theory

In QCT calculations, the reactant molecule is prepared with its internal rotational and vibrational energies corresponding to quantum states of the molecule. The time evolution of the system is determined by classical mechanics. The prefix *quasi* arises from the non–classical quantisation of the reagent and product internal energy states.

The main advantage of QCT is that, when compared to exact QM treatments, the computational effort is small [6]. The major drawback is its reliance on classical mechanics, and therefore the inability of QCT to account for quantum effects such as tunnelling, interference phenomena and resonance features [60].

For the A+BC type reaction, the method used is almost the same as that developed by Karplus *et al.* in the 1960s [53]. There have been several reviews on the QCT method, see for example Refs. [53, 174], the description presented here follows that of reference [73].

A.1 Equations of Motion

For the point masses m_A, m_B and m_C, with Cartesian coordinates x_i (i=1,...,9) and conjugate momenta p_{x_i}(i=1,...,9), the classical Hamiltonian is:

$$H(\mathbf{x}, \mathbf{p}_x) = T(\mathbf{p}_x) + V[R_1(\mathbf{x}), R_2(\mathbf{x}), R_3(\mathbf{x})], \tag{A.1a}$$

$$T(\mathbf{p}_x) = \sum_{i=1}^{3}\left(\frac{1}{2m_A}p_{x_i}^2 + \frac{1}{2m_B}p_{x_{i+3}}^2 + \frac{1}{2m_C}p_{x_{i+6}}^2\right), \tag{A.1b}$$

(this expression assumes that the potential energy function, V, is an analytic function of the three internuclear distances, R_i).

Hamilton's equations of motion are:

$$\dot{x}_i \equiv \frac{dx_i}{dt} = \frac{\partial H}{\partial p_{x_i}} = \frac{\partial T}{\partial p_{x_i}} \qquad (i = 1, \ldots, 9), \qquad \text{(A.2a)}$$

$$\dot{p}_{x_i} \equiv \frac{dp_{x_i}}{dt} = -\frac{\partial H}{\partial x_i} = -\frac{\partial V}{\partial x_i} = -\sum_{k=1}^{3} \frac{\partial V}{\partial R_k}\frac{\partial R_k}{\partial x_i} \qquad (i = 1, \ldots, 9), \qquad \text{(A.2b)}$$

where R_k are the internuclear distances, given by:

$$R_1 \equiv R_{AB} = \left[\sum_{i=1}^{3}(x_i - x_{i+3})^2\right]^{\frac{1}{2}}, \qquad \text{(A.3a)}$$

$$R_2 \equiv R_{BC} = \left[\sum_{i=1}^{3}(x_{i+3} - x_{i+6})^2\right]^{\frac{1}{2}}, \qquad \text{(A.3b)}$$

$$R_3 \equiv R_{AC} = \left[\sum_{i=1}^{3}(x_i - x_{i+6})^2\right]^{\frac{1}{2}}. \qquad \text{(A.3c)}$$

Thus, the entire trajectory calculation can be carried out by solving the 18 coupled first-order differential equations (A.2a, A.2b).

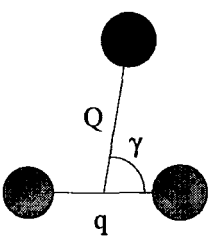

Figure A.1: Jacobi coordinate system. **Q** and **q** are the vectors associated with q_i and Q_i (i=1,2,3).

If the system is defined using Jacobi (figure A.1) rather than Cartesian coordinates, it is possible to reduce the number of differential equations involved in a trajectory calculation. The Jacobi coordinates are defined by:

$$q_i = x_{i+6} - x_{i+3} \qquad (i = 1, 2, 3), \qquad \text{(A.4a)}$$

$$Q_i = x_i - \frac{1}{m_B + m_C}[m_B x_{i+3} + m_C x_{i+6}] \qquad (i = 1, 2, 3), \qquad \text{(A.4b)}$$

$$S_i = \frac{1}{M}[m_A x_i + m_B x_{i+3} + m_C x_{i+6}] \qquad (i = 1, 2, 3), \qquad \text{(A.4c)}$$

where $M = m_A + m_B + m_C$; q_1, q_2, q_3 are the Cartesian coordinates of particle C with particle B defined as the origin; Q_1, Q_2, Q_3 are the Cartesian coordinates of particle A with respect to the centre of mass of the B, C pair; S_1, S_2, S_3 are the Cartesian coordinates of the system's centre of mass [53].

The Hamiltonian can be defined in terms of q_i, p_i, Q_i, P_i, S_i and P_{S_i}, where p_i, P_i and P_{S_i} are the conjugate momenta of q_i, Q_i and S_i respectively.

$$H(\mathbf{q}, \mathbf{Q}, \mathbf{p}, \mathbf{P}, \mathbf{P_S}) = T(\mathbf{p}, \mathbf{P}, \mathbf{P_S}) + V[R_1(\mathbf{q}, \mathbf{Q}), R_2(\mathbf{q}, \mathbf{Q}), R_3(\mathbf{q}, \mathbf{Q})], \tag{A.5a}$$

$$T(\mathbf{p}, \mathbf{P}, \mathbf{P_S}) = \sum_{i=1}^{3} \left(\frac{1}{2\mu_{BC}} p_i^2 + \frac{1}{2\mu_{A,BC}} P_i^2 + \frac{1}{2M} P_{S_i}^2 \right), \tag{A.5b}$$

where μ_{BC} and $\mu_{A,BC}$ are the reduced masses of the BC molecule and the A+BC system:

$$\mu_{BC} = \frac{m_B m_C}{m_B + m_C}, \tag{A.6a}$$

$$\mu_{A,BC} = \frac{m_A(m_B + m_C)}{M}. \tag{A.6b}$$

The internuclear distances, $\mathrm{R}_i(\mathbf{q},\mathbf{Q})$, are given by:

$$R_1 = \left[\sum_{i=1}^{3} \left(\frac{m_C}{m_B + m_C} q_i + Q_i \right)^2 \right]^{\frac{1}{2}}, \tag{A.7a}$$

$$R_2 = \left[\sum_{i=1}^{3} q_i^2 \right]^{\frac{1}{2}}, \tag{A.7b}$$

$$R_3 = \left[\sum_{i=1}^{3} \left(\frac{m_B}{m_B + m_C} q_i - Q_i \right)^2 \right]^{\frac{1}{2}}. \tag{A.7c}$$

The absence of S_i from the above equations for the internuclear distances means that R_i are independent of the system's centre of mass. We may therefore define the motion of the centre of mass as being constant and as a consequence, $\dot{P}_{S_1}$, $\dot{P}_{S_2}$ and $\dot{P}_{S_3}$ are zero and may be removed from the Hamiltonian, giving [53]:

$$H(\mathbf{q}, \mathbf{Q}, \mathbf{p}, \mathbf{P}) = T(\mathbf{p}, \mathbf{P}) + V[R_1(\mathbf{q}, \mathbf{Q}), R_2(\mathbf{q}, \mathbf{Q}), R_3(\mathbf{q}, \mathbf{Q})], \tag{A.8a}$$

$$T(\mathbf{p}, \mathbf{P}) = \sum_{i=1}^{3} \left(\frac{1}{2\mu_{BC}} p_i^2 + \frac{1}{2\mu_{A,BC}} P_i^2 \right). \tag{A.8b}$$

This results in 12 Hamilton's equations:

$$\dot{q}_i = \frac{\partial H}{\partial p_i} = \frac{\partial T}{\partial p_i} \qquad (i = 1, 2, 3), \qquad \text{(A.9a)}$$

$$\dot{Q}_i = \frac{\partial H}{\partial P_i} = \frac{\partial T}{\partial P_i} \qquad (i = 1, 2, 3), \qquad \text{(A.9b)}$$

$$\dot{p}_i = -\frac{\partial H}{\partial q_i} = -\frac{\partial V}{\partial q_i} = -\sum_{k=1}^{3} \frac{\partial V}{\partial R_k} \frac{\partial R_k}{\partial q_i} \qquad (i = 1, 2, 3), \qquad \text{(A.9c)}$$

$$\dot{P}_i = -\frac{\partial H}{\partial Q_i} = -\frac{\partial V}{\partial Q_i} = -\sum_{k=1}^{3} \frac{\partial V}{\partial R_k} \frac{\partial R_k}{\partial Q_i} \qquad (i = 1, 2, 3). \qquad \text{(A.9d)}$$

The number of equations can be reduced to 8 by taking into account the conservation of total energy and total angular momentum (three components). However, this results in more complex equations, and the conservation of energy and total angular momentum over the course of the trajectory calculation can be used to test the accuracy of the numerical integrations.

A.2 Initial Conditions

Before a collision trajectory can be calculated by the integration of the 12 Hamilton's equations, the initial state of the system must be specified. The values given to the initial coordinates and momenta (q_i^0, Q_i^0, p_i^0, P_i^0; i=1,2,3) depend upon the *collision parameters* chosen. These collision parameters define the initial geometry of the system, and make one trajectory different from another. For the collision of atom A with a selected rovibrational (v, j) state of BC at a fixed relative collision energy, E_{rel}, there are five collision parameters.

If we define atom A and the centre of mass of the BC molecule to lie in the yz-plane, with the initial relative velocity vector, $\mathbf{v}_{rel}$, of atom A directed along the $+z$-axis, the collision parameters are:

b The impact parameter, defined as the y component of the initial relative coordinate, Q_2^0.

Θ The polar orientation angle of the BC internuclear axis, *i.e.* the angle between **q** and the $+z$-axis.

ϕ The azimuthal orientation angle of the BC axis, defined as the angle between the projection of **q** on the xy-plane and the $+x$-axis.

η The orientation of BC angular momentum relative to a reference vector normal to the BC internuclear axis.

ξ The phase angle of the BC vibration, defined as zero at the inner turning point and π at the outer turning point.

Some of the collision parameters are shown in figure A.2.

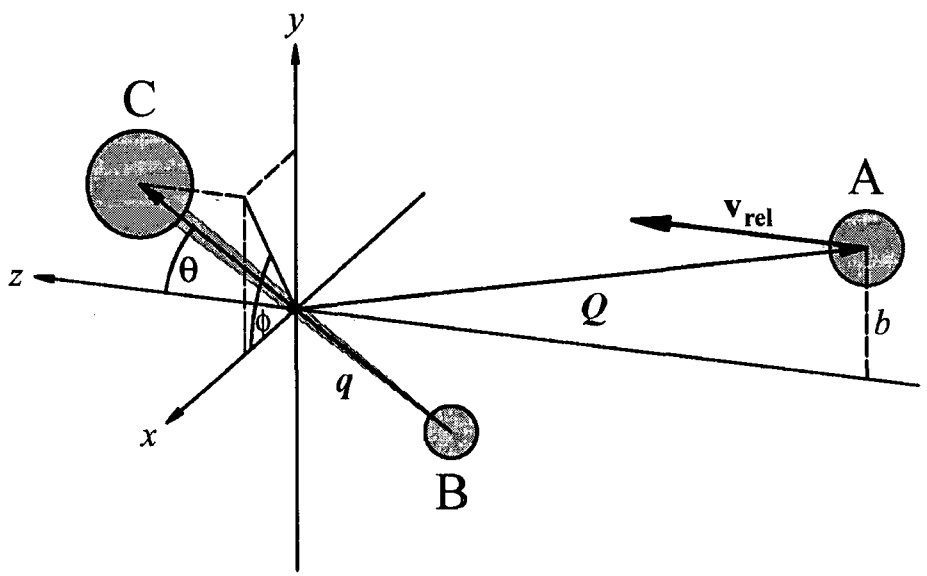

Figure A.2: The collision parameters used to define the initial geometry of a system for QCT calculations.

A.3 Calculation of a Trajectory

The trajectory is calculated by the numerical integration of the equations of motion for the given initial values of q_i, Q_i, p_i and P_i (i=1,2,3). The accuracy of the integrations can be checked via the conservation of energy and total angular momentum.

The integration in time is continued until the collision products have separated beyond the 'collision shell' distance, ρ_0. Analysis of the collision products can then take place.

A.4 Product Analysis

The most convenient method for dealing with the products of a trajectory calculation is to define a new set of coordinates and conjugate momenta, $\mathbf{q}'$, $\mathbf{Q}'$, $\mathbf{p}'$ and $\mathbf{P}'$, where $\mathbf{q}'$ and $\mathbf{p}'$ are the coordinates and momenta of the product molecule, and $\mathbf{Q}'$ and $\mathbf{P}'$ are the same but for the relative motion of the products. If the product molecule is BC, no reaction has taken place and no coordinate transformation is required.

Use of the appropriate expressions for $\mathbf{q}'$, $\mathbf{Q}'$, $\mathbf{p}'$ and $\mathbf{P}'$ gives some of the final properties of the reaction. Several of these properties, such as the various angular momenta and internal energies, are continuous according to classical mechanics, but would have discrete values if quantum mechanics was used.

The rotational angular momentum of the product molecule is given by:

$$\mathbf{J}'_r = \mathbf{q}' \times \mathbf{p}', \tag{A.10a}$$

$$= (q'_2 p'_3 - q'_3 p'_2)\hat{\mathbf{e}}_x + (q'_3 p'_1 - q'_1 p'_3)\hat{\mathbf{e}}_y + (q'_1 p'_2 - q'_2 p'_1)\hat{\mathbf{e}}_z, \tag{A.10b}$$

where $\hat{e}_x$, $\hat{e}_y$, $\hat{e}_z$ are the Cartesian unit vectors.

The rotational quantum state can then be calculated by equating the square of the modulus of the rotational angular momentum to $j'(j'+1)\hbar^2$ [60]. The vibrational quantum state, v', is found by equating the internal energy of the product molecule to a Dunham expansion in $(v'+\frac{1}{2})$ and $j'(j'+1)$ (details of this can be found in reference [60]). The non-integer v' and j' can be rounded to the nearest integer, giving the quasi-classical quantum states.

The other major final state property of interest is the centre-of-mass (CM) scattering angle, defined as:

$$\theta = 180° - \cos^{-1} \frac{\mathbf{v}_{rel} \cdot \mathbf{v}'_{rel}}{v_{rel} v'_{rel}}. \tag{A.11}$$

Where $\mathbf{v}_{rel}$ and $\mathbf{v}'_{rel}$ are the velocity vectors of the reactant and product atoms respectively, and v_{rel}, v'_{rel} are the speeds of the reactant and product atoms respectively. We use the traditional definition of the scattering angle, *i.e.* the angle between the reactant atom and the product molecule.

As alluded to earlier, the major drawback to QCT is its reliance on classical mechanics. The assignment of internal quantum states relies on rounding or truncating the classically continuous values generated, and this can introduce errors into

the final state properties. QCT has other drawbacks, notably at energies near the threshold for reaction. One of the reasons for this failure is how QCT accounts for the zero point energies of the molecules involved. In some instances, quasi-classical trajectories can cross barriers whilst having less than zero point energy, leading to artificially low reaction thresholds [5].

A.5 Reaction Attributes

Once a statistically significant number of trajectories has been calculated using pseudo random collision parameters, quantities such as the opacity function (probability of reaction as a function of impact parameter) and various state-to-state cross sections can be calculated and compared to experimental results.

Appendix B

QCT Quantum State Distributions

This appendix contains quantum state distribution tables for all trajectory batches, unless stated otherwise one million trajectories were calculated.

j'	v'=0	v'=1	v'=2	v'=3	v'=4	v'=5	Total j'
0	7390	3807	1880	793	223	16	14109
1	28272	13392	6143	2273	693	43	50816
2	46340	21224	9010	3451	858	38	80921
3	63993	28453	11607	4090	1034	46	109223
4	81544	34560	13476	4702	1041	41	135364
5	96960	38435	14215	4586	833	15	155044
6	110022	41511	14368	3980	577	2	170460
7	118284	41843	13515	3114	375	0	177131
8	121148	39330	12255	2449	193	0	175375
9	117627	35072	10146	1701	75	0	164621
10	106772	29032	7850	1187	23	0	144864
11	90978	22826	5500	660	4	0	119968
12	71594	16867	3310	253	0	0	92024
13	50498	11212	1738	53	0	0	63501
14	32123	6707	670	1	0	0	39501
15	17921	3560	176	0	0	0	21657
16	8337	1730	41	0	0	0	10108
17	2853	767	1	0	0	0	3621
18	546	226	0	0	0	0	772
19	169	45	0	0	0	0	214
20	60	3	0	0	0	0	63
21	14	0	0	0	0	0	14
22	1	0	0	0	0	0	1
Total v'	1173446	390602	125901	33293	5929	201	1729372

Table B.1: Quantum State Distribution for reactive trajectories at energies between 0.9–2.2 eV, in three dimensions. 8,750,000 trajectories were calculated.

j'	v'=0	v'=1	v'=2	v'=3	v'=4	v'=5	Total j'
0	2324	1818	1060	787	862	135	6986
1	2954	2282	1460	998	1074	179	8947
2	2976	2225	1605	1112	954	114	8986
3	3377	2518	1974	1575	1132	62	10638
4	3658	2970	2428	2413	1466	39	12974
5	4115	3271	3131	3801	1325	5	15648
6	4533	3840	4604	3906	929	0	17812
7	4950	4462	6372	3367	686	0	19837
8	5383	5652	7388	2737	394	0	21554
9	5849	8064	6925	2083	184	0	23105
10	6486	10583	5667	1515	45	0	24296
11	7830	12841	4259	991	1	0	25922
12	9787	13502	2822	445	0	0	26556
13	9766	10962	1726	63	0	0	22517
14	10544	7029	800	2	0	0	18375
15	8329	4123	265	0	0	0	12717
16	4874	2229	57	0	0	0	7160
17	2014	1046	0	0	0	0	3060
18	335	320	0	0	0	0	655
19	73	90	0	0	0	0	163
20	71	0	0	0	0	0	71
21	24	0	0	0	0	0	24
Total v'	100252	99827	52543	25795	9052	534	288003

Table B.2: Quantum State Distribution for the reactive trajectories at $E_{\text{rel}} = 2.1$ eV, in two dimensions.

j'	v'=0	v'=1	v'=2	v'=3	v'=4	Total j'
0	3084	1934	1007	942	505	7472
1	4007	2591	1476	1358	518	9950
2	4018	2847	1785	1593	450	10693
3	4379	3313	2416	2287	370	12765
4	4976	3898	3624	2466	276	15240
5	5531	4588	5107	2442	183	17851
6	6103	5866	5716	2234	46	19965
7	6651	8091	5785	1618	3	22148
8	7532	10055	5317	1117	0	24021
9	9005	11921	4175	714	0	25815
10	11842	11859	2977	396	0	27074
11	16196	9698	1910	56	0	27860
12	18317	7127	881	2	0	26327
13	17323	4612	197	0	0	22132
14	13421	2510	13	0	0	15944
15	7667	1177	2	0	0	8846
16	3314	388	0	0	0	3702
17	735	41	0	0	0	776
18	126	0	0	0	0	126
19	93	0	0	0	0	93
20	15	0	0	0	0	15
Total v'	144335	92516	42388	17225	2351	298815

Table B.3: Quantum State Distribution for the reactive trajectories at E_{rel} = 1.85 eV, in two dimensions.

j'	v'=0	v'=1	v'=2	v'=3	v'=4	Total j'
0	2337	1537	1103	748	269	5994
1	9114	6184	4091	2598	730	22717
2	15422	10135	6690	4015	884	37146
3	20958	14338	9427	5194	751	50668
4	27573	18784	12269	5131	498	64255
5	34077	23165	13993	4886	262	76383
6	40296	27670	14318	4189	65	86538
7	47774	31978	13932	3085	1	96770
8	54889	34365	12329	1992	0	103575
9	63112	33752	10335	1228	0	108427
10	69382	29714	8162	580	0	107838
11	69394	24066	5556	51	0	99067
12	63248	17314	2769	0	0	83331
13	52126	10574	419	0	0	63119
14	36728	5297	23	0	0	42048
15	21042	2244	0	0	0	23286
16	8713	593	0	0	0	9306
17	1834	52	0	0	0	1886
18	421	0	0	0	0	421
19	164	0	0	0	0	164
20	8	0	0	0	0	8
Total v'	638612	291762	115416	33697	3460	1082947

Table B.4: Quantum State Distribution for the reactive trajectories at E_{rel} = 1.85 eV, in three dimensions. 5,000,000 trajectories were calculated.

j'	v'=0	v'=1	v'=2	v'=3	v'=4	Total j'
0	3853	1861	1145	1007	52	7918
1	5262	2705	1776	1259	26	11028
2	5180	3147	2211	1241	9	11788
3	5674	4074	3270	1332	1	14351
4	6436	5081	4129	1304	0	16950
5	7170	6778	4651	1052	0	19651
6	7848	8427	4668	687	0	21630
7	9428	10037	4187	367	0	24019
8	12026	10751	3294	79	0	26150
9	15642	10049	2372	4	0	28067
10	20242	7859	1361	0	0	29462
11	23010	5471	409	0	0	28890
12	22243	2978	12	0	0	25233
13	17650	1392	2	0	0	19044
14	10253	430	0	0	0	10683
15	4259	20	0	0	0	4279
16	788	1	0	0	0	789
17	136	0	0	0	0	136
18	57	0	0	0	0	57
Total v'	177157	81061	33487	8332	88	300125

Table B.5: Quantum State Distribution for the reactive trajectories at E_{rel} = 1.64 eV, in two dimensions.

j'	v'=0	v'=1	v'=2	v'=3	v'=4	Total j'
0	593	382	250	144	9	1378
1	2461	1546	910	367	7	5291
2	4153	2400	1432	515	3	8503
3	5806	3497	1887	495	0	11685
4	7522	4432	2205	514	0	14673
5	9112	5233	2233	385	0	16963
6	10714	5939	2113	228	0	18994
7	12578	6291	1851	102	0	20822
8	14247	6007	1578	14	0	21846
9	15709	5317	1134	2	0	22162
10	15744	4231	698	0	0	20673
11	14850	2838	218	0	0	17906
12	12294	1379	2	0	0	13675
13	8642	581	0	0	0	9223
14	4756	138	0	0	0	4894
15	1946	5	0	0	0	1951
16	286	0	0	0	0	286
17	51	0	0	0	0	51
18	16	0	0	0	0	16
Total v'	141480	50216	16511	2766	19	210992

Table B.6: Quantum State Distribution for the reactive trajectories at 1.64 eV, in three dimensions.

j'	v'=0	v'=1	v'=2	v'=3	Total j'
0	722	449	279	87	1537
1	3173	1714	878	192	5957
2	5151	2739	1269	256	9415
3	7137	3760	1533	230	12660
4	9280	4644	1769	177	15870
5	11197	5227	1792	57	18273
6	13063	5626	1497	4	20190
7	15142	5674	1072	0	21888
8	16511	5196	841	0	22548
9	17110	4178	450	0	21738
10	16339	2617	49	0	19005
11	14200	1117	1	0	15318
12	10292	381	0	0	10673
13	5827	55	0	0	5882
14	2408	1	0	0	2409
15	429	0	0	0	429
16	35	0	0	0	35
17	7	0	0	0	7
Total v'	148023	43378	11430	1003	203834

Table B.7: Quantum State Distribution for the reactive trajectories at $E_{\text{rel}} = 1.49$ eV, in three dimensions.

Appendix C

Coupling Light into a Ring-Down Cavity

Transverse mode beatings in a ring-down cavity are minimized by spatially matching the input laser beam to the TEM_{00} mode of the cavity, this is achieved using a telescope and pinhole arrangement to form a Gaussian beam [146]. This Gaussian beam can then be coupled into the TEM_{00} mode of the cavity. A ring-down cavity is an optical resonator, and as such it supports an electromagnetic field whose spherical wavefront matches the curvature of the mirrors.

To efficiently couple into a transverse mode of the cavity the focus of the input light has to match the waist of the cavity with the correct spot size [149]. A measure of the spot size at the cavity waist is ω_0, defined as the radius of the beam at the centre of the cavity, where the light intensity drops to $1/e$ of its value on the axis. In practice this can be achieved by the addition of a 'coupling' lens before the cavity, as shown in Fig. C.1.

For a symmetric mirror resonator the beam waist, ω_0, is defined by:

$$\omega_0 = \left(\frac{\lambda z_0}{\pi n}\right)^{1/2} \tag{C.1}$$

where λ is the wavelength of light, n is the refractive index of the medium in the cavity and z_0, the characteristic length of the cavity, which is given by:

$$z_0 = \frac{(2R - l)l}{4} \tag{C.2}$$

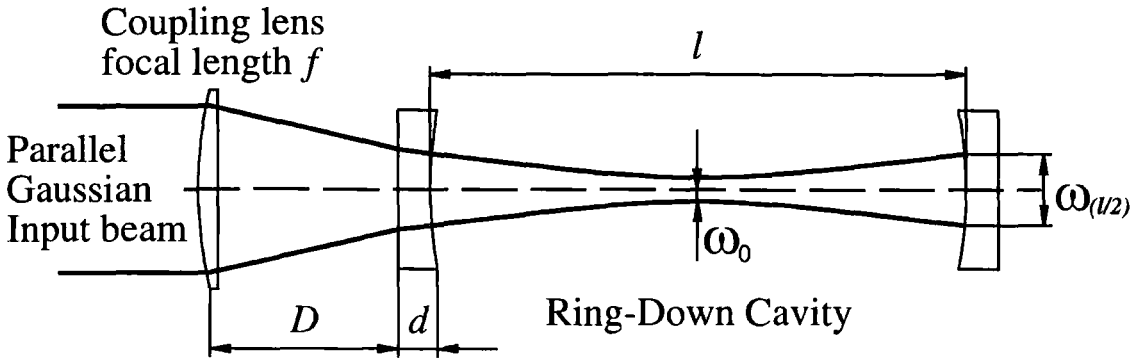

Figure C.1: A theoretical RDC with coupling lens, showing the light path into the cavity, the beam waist ω_0, the size of the beam at the output mirror $\omega_{(l/2)}$, and all relevant dimensions, the radius of curvature of the mirrors is denoted R.

This allows the calculation of the beam spot size at the mirror,

$$\omega_{(l/2)} = \omega_0 \left(1 + \frac{l}{2z_0}\right)^{1/2} \tag{C.3}$$

the gradient of the beam at the mirror is given by $[\omega'_{(l/2)} = \omega_{(l/2)}/R]$.

C.1 Ray Matrices

Here we follow the methodology of Yariv [150], using matrices to describe the propagation of optical rays.

Consider a paraxial ray passing through a thin lens of focal length, f. Taking the cylindrical axis of symmetry as z, denoting the ray distance from the axis by r and its slope dr/dz as r', we can relate the output ray $(r_{\text{out}}, r'_{\text{out}})$ to the input ray $(r_{\text{in}}, r'_{\text{in}})$ by means of

$$\begin{aligned} r_{\text{out}} &= r_{\text{in}} \\ r'_{\text{out}} &= r'_{\text{in}} - \frac{r_{\text{in}}}{f} \end{aligned} \tag{C.4}$$

Representing a ray at any position z as a column matrix,

$$\mathbf{r}(z) = \begin{bmatrix} r(z) \\ r'(z) \end{bmatrix} \tag{C.5}$$

The ray matrices for other optical elements can be found in Ref. [150].

For the specific problem we are considering here, coupling a parallel Gaussian beam into a stable optical cavity, we have defined matrices appropriate to the optical

set-up shown in Fig. C.1. To couple the beam into the cavity we must ensure that it has the correct spot size and gradient when it enters the cavity and hence will have the correct beam waist at the centre of the cavity. If the starting point is just inside the cavity at the interface of the spherical mirror then

$$\mathbf{r}(\text{at mirror}) = \begin{bmatrix} \omega_{(l/2)} \\ \dfrac{\omega_{(l/2)}}{R} \end{bmatrix} \tag{C.6}$$

where R is the radius of curvature of the mirrors. Working from the cavity (vacuum) to the coupling lens we first have to go into the mirror substrate (UV silica) which is a spherical dielectric interface:

$$\mathbf{r}(\text{into mirror}) = \begin{bmatrix} \omega_{(l/2)} \\ \dfrac{\omega_{(l/2)}}{R} \end{bmatrix} = \begin{bmatrix} 1 & 0 \\ \dfrac{n_1 - n_0}{n_1 R} & \dfrac{n_0}{n_1} \end{bmatrix} \begin{bmatrix} \omega_{(l/2)} \\ \dfrac{\omega_{(l/2)}}{R} \end{bmatrix} \tag{C.7}$$

where n_0 is the refractive index of the medium in the cavity and n_1 is the refractive index of the mirror substrate. Note that the spherical dielectric interface has no effect on the spot size or gradient, so the multiple coatings on the mirrors do not have to be considered.

The beam now travels within the mirror, thickness d, which has the matrix:

$$\text{through mirror} = \begin{bmatrix} 1 & d \\ 0 & 1 \end{bmatrix} \tag{C.8}$$

The beam then goes from the mirror to the air outside the cavity through a dielectric interface:

$$\text{mirror to air} = \begin{bmatrix} 1 & 0 \\ 0 & \dfrac{n_1}{n_2} \end{bmatrix} \tag{C.9}$$

where n_2 is the refractive index of the air outside the cavity. From the mirror to the lens the beam travels a distance D according to:

$$\text{mirror to lens} = \begin{bmatrix} 1 & D \\ 0 & 1 \end{bmatrix} \tag{C.10}$$

The lens, of focal length f, is now used to make the beam parallel, as it would arrive

from the laser:

$$\text{lens to parallel} = \begin{bmatrix} 1 & 0 \\ -\frac{1}{f} & 1 \end{bmatrix} \tag{C.11}$$

The product of these matrices and $\mathbf{r}(\text{at mirror})$ gives the spot size, r_{lens}, and gradient, r'_{lens}, at the lens:

$$\begin{aligned} r_{\text{lens}} &= \frac{\omega_{(l/2)}(n_2 R + dn_2 + Dn_1)}{n_2 R} \\ r'_{\text{lens}} &= \frac{\omega_{(l/2)}(-n_2 R - dn_2 - Dn_1 + n_1 f)}{f n_2 R} \end{aligned} \tag{C.12}$$

For a parallel beam at the lens the gradient r'_{lens} must equal zero, thus Eqn. C.12 can be solved to give a distance D for a lens with a given focal length f.

Our cavity had a length, l, of 770 mm with mirrors of radius of curvature, R, of 1000 mm, thus under vacuum, $n_0 = 0$, at 320 nm eqn. C.3 gives us:

$$\begin{aligned} \omega_{(l/2)} &= 0.284 \text{ mm} \\ \omega'_{(l/2)} &= 0.000284 \end{aligned}$$

Using a lens with a focal length of 750 mm at $\approx$ 320 nm our f was 714 mm (found by interpolating the value of refractive index of UV silica between 302.2 and 330.3 nm [175]), and $r'_{\text{lens}} = 0$, $n_1 = 1.482978$, $n_2 = 1.000277$ and $d = 4$ mm then D, the distance between the mirror and lens, is calculated to have a value of 37.24 mm.

N.B. The measurement of d comes from the mirror manufacturer, and could not be accurately determined at the centre of the mirror.

Appendix D

Experimental and Theoretical Comparison Plots

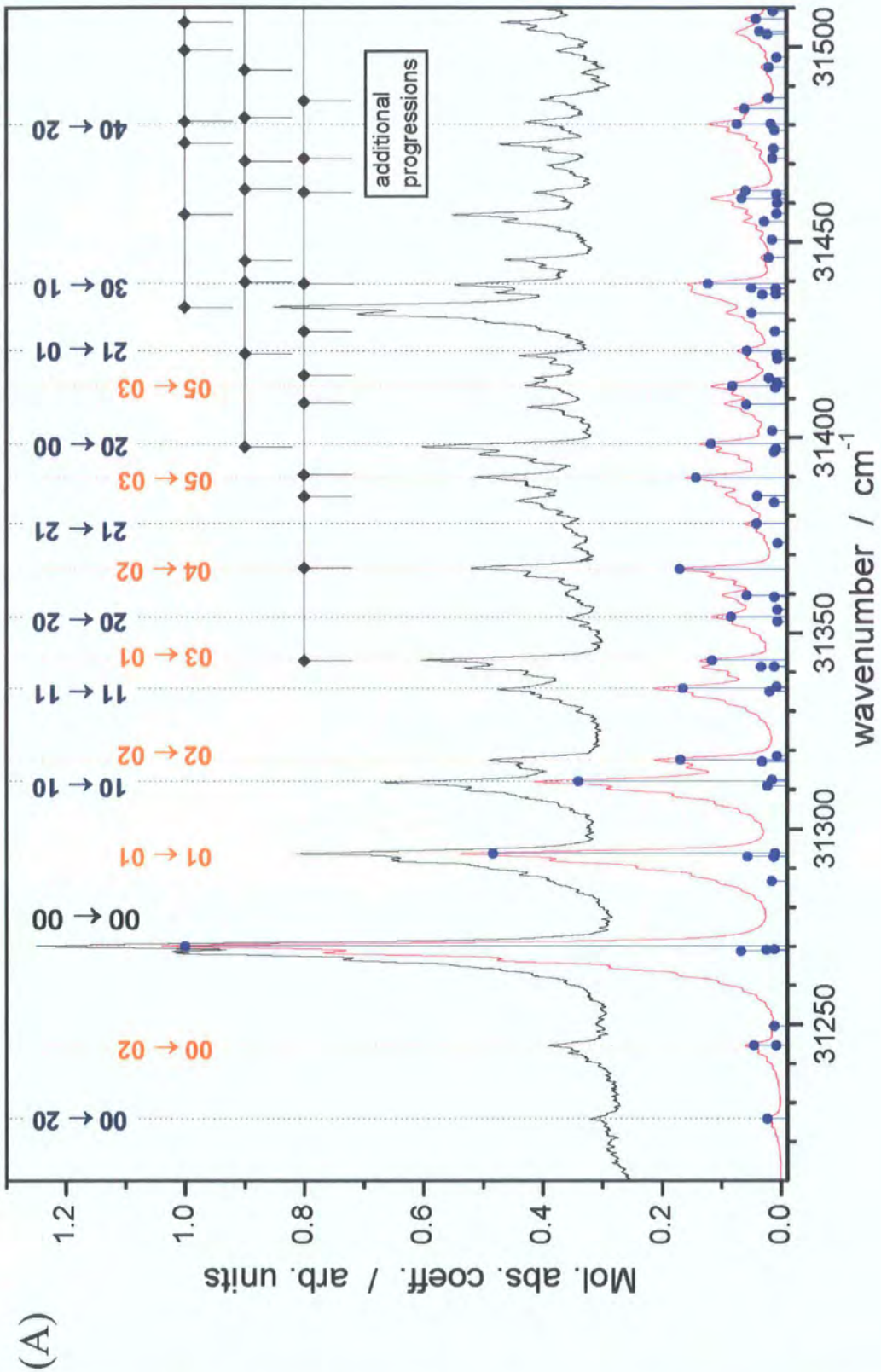

Figure D.1: Comparison of experimental (black line) and simulated (red line) spectra for (A) BPEB, see Fig. 9.11 for details.

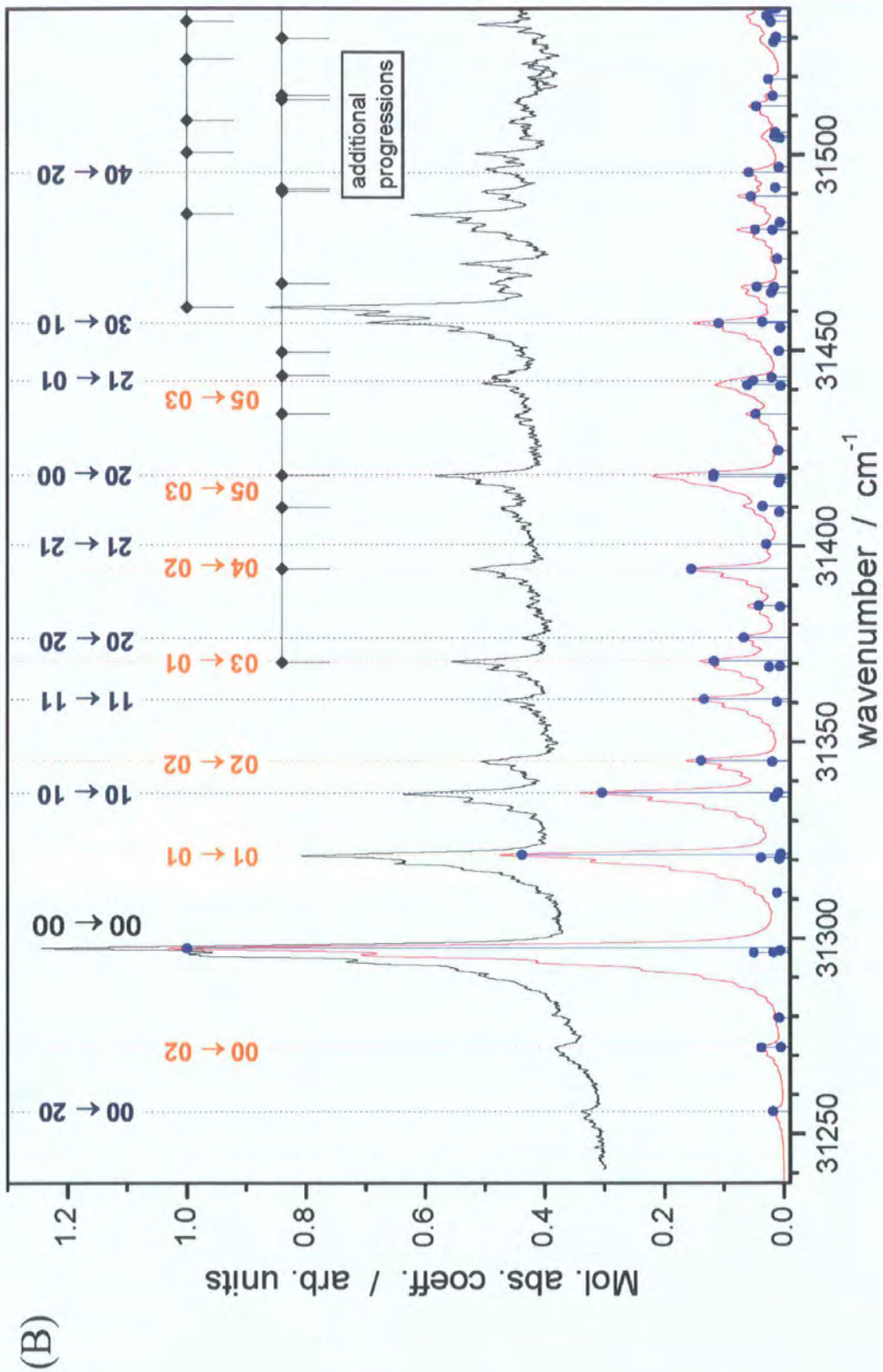

Figure D.2: Comparison of experimental (black line) and simulated (red line) spectra for (B) D-BPEB, see Fig. 9.11 for details.

Bibliography

[1] S. C. Althorpe, F. Fernández-Alonso, B. D. Bean, J. D. Ayers, A. E. Pomerantz, R. N. Zare, and E. Wrede, *Nature*, 2002, **416**(6876), 67–70.

[2] F. London, *Z. Electrochem*, 1929, **35**, 552.

[3] D. G. Truhlar and R. E. Wyatt, *Ann. Rev. Phys. Chem.*, 1976, **27**, 1–43.

[4] D. G. Truhlar and R. E. Wyatt, *Adv. Chem. Phys.*, 1977, **36**, 141–204.

[5] G. C. Schatz, *Ann. Rev. Phys. Chem.*, 1988, **39**, 317–340.

[6] H. Buchenau, J. P. Toennies, J. Arnold, and J. Wolfrum, *Ber. Bunsenges. Phys. Chem.*, 1990, **94**, 1231–1248.

[7] W. H. Miller, *Ann. Rev. Phys. Chem.*, 1990, **41**, 245–281.

[8] R. D. Levine and R. B. Bernstein, *Molecular Reaction Dynamics and Chemical Reactivity*, Oxford University, Oxford, 1987.

[9] F. Hund, *Z. Phys.*, 1927, **13**, 93.

[10] K. F. Bonhoffer and P. Harteek, *Naturwissenschaften*, 1929, **17**, 182.

[11] A. Farkas and L. Farkas, *Proc. R. Soc. (London) A*, 1935, **152**, 124–157.

[12] A. Farkas, *Z. Phys. Chem*, 1930, **B10**, 419.

[13] A. A. Westenberg and N. deHaas, *J. Chem. Phys.*, 1967, **47**, 1393–1405.

[14] W. Meier, G. Ahlers, and H. Zacharias, *J. Chem. Phys.*, 1986, **85**(5), 2599–2608.

[15] J. Arnold, T. Dreier, and D. W. Chandler, *Chem. Phys.*, 1989, **133**(1), 123–136.

[16] W. H. Miller, *J. Chem. Phys.*, 1969, **50**, 407–418.

[17] A. Kupperman and J. M. White, *J. Chem. Phys.*, 1966, **44**, 4352–4354.

[18] D. A. V. Kliner, D. E. Adelman, and R. N. Zare, *J. Chem. Phys.*, 1991, **94**(2), 1069–1080.

[19] J.-C. Nieh and J. J. Valentini, *J. Chem. Phys.*, 1990, **92**, 1083–1097.

[20] N. E. Shafer, W. R. Simpson, H. Xu, and R. N. Zare, *Chem. Phys. Lett.*, 1993, **212**(1-2), 155–162.

[21] F. Fernández-Alonso, B. D. Bean, and R. N. Zare, *J. Chem. Phys.*, 1999, **111**(3), 1022–1034.

[22] F. Fernández-Alonso, B. D. Bean, and R. N. Zare, *J. Chem. Phys.*, 1999, **111**(3), 1035–1042.

[23] F. Fernández-Alonso, B. D. Bean, and R. N. Zare, *J. Chem. Phys.*, 1999, **111**(6), 2490–2498.

[24] J. D. Ayers, A. E. Pomerantz, F. Fernández-Alonso, F. Ausfelder, B. D. Bean, and R. N. Zare, *J. Chem. Phys.*, 2003, **119**(9), 4662–4670.

[25] A. E. Pomerantz, F. Ausfelder, R. N. Zare, S. C. Althorpe, F. J. Aoiz, L. Bañares, and J. F. Castillo, *J. Chem. Phys.*, 2004, **120**(7), 3244–3254.

[26] F. Ausfelder, A. E. Pomerantz, R. N. Zare, S. C. Althorpe, F. J. Aoiz, L. Bañares, and J. F. Castillo, *J. Chem. Phys.*, 2004, **120**(7), 3255–3264.

[27] J. Geddes, H. F. Krause, and W. L. Fite, *J. Chem. Phys.*, 1972, **56**, 3298–3307.

[28] R. Götting, H. R. Mayne, and J. P. Toennies, *J. Chem. Phys.*, 1986, **85**, 6396–6419.

[29] S. A. Buntin, C. F. Giese, and W. R. Gentry, *J. Chem. Phys.*, 1987, **87**, 1443–1445.

[30] E. Wrede and L. Schnieder, *J. Chem. Phys.*, 1997, **107**(3), 786–790.

[31] L. Schnieder, K. Seekamp-Rahn, E. Wrede, and K. H. Welge, *J. Chem. Phys.*, 1997, **107**(16), 6175–6195.

[32] E. Wrede, L. Schnieder, K. H. Welge, F. J. Aoiz, L. Bañares, J. F. Castillo, B. Martínez-Haya, and V. J. Herrero, *J. Chem. Phys.*, 1999, **110**(20), 9971–9981.

[33] L. Schnieder, K. Seekamp-Rahn, J. Borkowski, E. Wrede, K. H. Welge, F. J. Aoiz, L. Bañares, M. J. D'Mello, V. J. Herrero, V. S. Rábanos, and R. E. Wyatt, *Science*, 1995, **269**(5221), 207–210.

[34] L. Schnieder, W. Meier, K. H. Welge, M. N. R. Ashfold, and C. M. Western, *J. Chem. Phys.*, 1990, **92**(12), 7027–7037.

[35] L. Bañares, F. J. Aoiz, V. J. Herrero, M. J. D'Mello, B. Niederjohann, K. Seekamp-Rahn, E. Wrede, and L. Schnieder, *J. Chem. Phys.*, 1998, **108**(15), 6160–6169.

[36] S. A. Harich, D. X. Dai, C. C. Wang, X. M. Yang, S. D. Chao, and R. T. Skodje, *Nature*, 2002, **419**, 281–284.

[37] S. D. Chao, S. A. Harich, D. X. Dai, C. C. Wang, X. M. Yang, and R. T. Skodje, *J. Chem. Phys.*, 2002, **117**, 8341–8361.

[38] D. X. Dai, C. C. Wang, S. A. Harich, X. Y. Wang, X. M. Yang, S. D. Chao, and R. T. Skodje, *Science*, 2003, **300**(5626), 1730–1734.

[39] R. T. Skodje and X. M. Yang, *Int. Rev. Phys. Chem.*, 2004, **23**(2), 253–287.

[40] S. L. Mielke, B. C. Garrett, and K. A. Peterson, *J. Chem. Phys.*, 2002, **116**(10), 4142–4161.

[41] R. N. Porter and M. Karplus, *J. Chem. Phys.*, 1964, **40**, 1105–1115.

[42] B. Liu, *J. Chem. Phys.*, 1973, **58**, 1925–1937.

[43] P. Siegbahn and B. Liu, *J. Chem. Phys.*, 1978, **68**, 2457.

[44] D. G. Truhlar and C. J. Horowitz, *J. Chem. Phys.*, 1978, **68**, 2466.

[45] A. J. C. Varandas, F. B. Brown, C. A. Mead, D. G. Truhlar, and N. C. Blais, *J. Chem. Phys.*, 1987, **86**, 6258–6269.

[46] A. I. Boothroyd, W. J. Keogh, P. G. Martin, and M. R. Peterson, *J. Chem. Phys.*, 1991, **95**(6), 4343–4359.

[47] A. I. Boothroyd, W. J. Keogh, P. G. Martin, and M. R. Peterson, *J. Chem. Phys.*, 1996, **104**(18), 7139–7152.

[48] S. L. Mielke, B. C. Garrett, and K. A. Peterson, *J. Chem. Phys.*, 1999, **111**(9), 3806–3811.

[49] S. L. Mielke, K. A. Peterson, D. W. Schwenke, B. C. Garrett, D. G. Truhlar, J. V. Michael, M. C. Su, and J. W. Sutherland, *Phys. Rev. Lett.*, 2003, **91**(6), 063201.

[50] J. V. Michael, M. C. Su, and J. W. Sutherland, *J. Phys. Chem. A*, 2004, **108**(3), 432–437.

[51] J. Hirschfelder, H. Eyring, and B. Topley, *J. Chem. Phys.*, 1936, **4**, 170–177.

[52] F. T. Wall, L. A. Hiller, and J. Mazur, *J. Chem. Phys.*, 1958, **29**, 255–263.

[53] M. Karplus, R. N. Porter, and R. D. Sharma, *J. Chem. Phys.*, 1965, **43**, 3259–3287.

[54] F. Fernández-Alonso, B. D. Bean, J. D. Ayers, A. E. Pomerantz, R. N. Zare, L. Bañares, and F. J. Aoiz, *Angew. Chem. Int. Ed.*, 2000, **39**(15), 2748–2752.

[55] F. J. Aoiz, L. Banares, M. J. D'Mello, V. J. Herrero, V. S. Rábanos, L. Schnieder, and R. E. Wyatt, *J. Chem. Phys.*, 1994, **101**(7), 5781–5791.

[56] F. J. Aoiz, V. J. Herrero, and V. S. Rábanos, *J. Chem. Phys.*, 1992, **97**(10), 7423–7436.

[57] J. G. Muga and R. D. Levine, *Chem. Phys. Lett.*, 1989, **162**, 7–13.

[58] F. J. Aoiz, V. J. Herrero, and V. S. Rábanos, *J. Chem. Phys.*, 1991, **95**, 7767–7768.

[59] F. J. Aoiz, V. J. Herrero, and V. S. Rábanos, *J. Chem. Phys.*, 1991, **94**(12), 7991–8007.

[60] F. J. Aoiz, L. Bañares, and V. J. Herrero, *J. Chem. Soc. Faraday Trans.*, 1998, **94**, 2483–2500.

[61] B. K. Kendrick, *J. Chem. Phys.*, 2001, **114**(20), 8796–8819.

[62] S. C. Althorpe, *J. Chem. Phys.*, 2001, **114**(4), 1601–1616.

[63] S. C. Althorpe, *Int. Rev. Phys. Chem.*, 2004, **23**(2), 219–251.

[64] W. Zhu, T. Peng, and J. Z. H. Zhang, *J. Chem. Phys.*, 1997, **106**(5), 1742–1748.

[65] S. C. Althorpe, *J. Chem. Phys.*, 2004, **121**(3), 1175–1186.

[66] D. E. Manolopoulos, *Nature*, 2002, **419**, 266–267.

[67] T. C. Allison, R. S. Friedman, D. J. Kaufman, and D. G. Truhlar, *Chem. Phys. Lett.*, 2000, **327**, 439–445.

[68] R. T. Skodje, D. Skouteris, D. E. Manolopoulos, S.-H. Lee, F. Dong, and K. Liu, *Phys. Rev. Lett.*, 2000, **185**(6), 1206–1209.

[69] R. Sadeghi and R. T. Skodje, *J. Chem. Phys.*, 1995, **102**, 193–213.

[70] B. K. Kendrick, L. Jayasinghe, S. Moser, M. Auzinsh, and N. Shafer-Ray, *Phys. Rev. Lett.*, 2000, **84**, 4325–4328.

[71] F. J. Aoiz, L. Bañares, and J. F. Castillo, *J. Chem. Phys.*, 2001, **114**(19), 8237–8239.

[72] S. C. Althorpe, *J. Chem. Phys.*, 2002, **117**(10), 4623–4627.

[73] D. G. Truhlar and J. T. Muckerman In ed. R. B. Bernstein, *Atom-Molecule Collision Therory: A Guide for the Experimentalists*, pp. 505–566, New York, 1979. Plenum Press.

[74] F. J. Aoiz and L. Bañares, QCT program Priv. Comm.

[75] E. Wrede, QCT program.

[76] A. Ralston and H. Wilf, *Mathematical methods for digital computers*, John Wiley & Sons, Inc., London, 1960.

[77] P. F. Bernath, *Spectra of Atoms and Molecules*, Oxford University Press, Oxford, 1995.

[78] B. K. Kendrick, *J. Chem. Phys.*, 2003, **118**(23), 10502–10521.

[79] J. C. Juanes-Marcos and S. C. Althorpe, *Chem. Phys. Lett.*, 2003, **381**(5-6), 743–750.

[80] G. E. Moore, *Electronics*, 1965, **38**(8), 1–4.

[81] J. Chen, M. A. Reed, A. M. Rawlett, and J. M. Tour, *Science*, 1999, **286**, 1550–1552.

[82] M. A. Reed and J. M. Tour, *Sci. Am.*, 2000, **June**, 86–93.

[83] M. A. Reed, C. Zhou, C. J. Muller, T. P. Burgin, and J. M. Tour, *Science*, 1997, **278**, 252–254.

[84] J. M. Seminario, A. G. Zacarias, and J. M. Tour, *J. Am. Chem. Soc.*, 1998, **120**(16), 3970–3974.

[85] J. Chen, W. Wang, M. A. Reed, R. A. M., D. W. Price, and J. M. Tour, *Appl. Phys. Lett.*, 2000, **77**(8), 1224–1226.

[86] Z. J. Donhauser, B. A. Mantooth, K. F. Kelly, L. A. Bumm, J. D. Monnell, J. J. Stapleton, D. W. P. Jr., A. M. Rawlett, D. L. Allara, J. M. Tour, and P. S. Weiss, *Science*, 2001, **292**, 2303–2307.

[87] J. Casado, R. G. Hicks, V. Hernández, D. J. T. Myles, M. C. R. Delgado, and J. T. L. Navarrete, *J. Chem. Phys.*, 2003, **118**(4), 1912–1920.

[88] J. L. Bredas, G. B. Street, B. Thémans, and J. M. André, *J. Chem. Phys.*, 1985, **83**(3), 1323–1329.

[89] C. Kergueris, J.-P. Bourgoin, S. Palacin, D. Esteve, C. Urbina, M. Magoga, and C. Joachim, *Phys. Rev. B*, 1999, **59**, 12505–12513.

[90] D. Kruger, H. Fuchs, R. Rousseau, D. Marx, and M. Parrinello, *Phys. Rev. Lett.*, 2002, **89**(18), 186402.

[91] J. M. Seminario, A. G. Zacarias, and J. M. Tour, *J. Am. Chem. Soc.*, 2000, **122**(13), 3015–3020.

[92] J. Tomfohr and O. F. Sankey, *J. Chem. Phys.*, 2004, **120**(3), 1542–1554.

[93] A. Beeby, K. Findlay, P. J. Low, and T. B. Marder, *J. Am. Chem. Soc.*, 2002, **124**(28), 8280–8284.

[94] K. Okuyama, T. Hasegawa, M. Ito, and N. Mikami, *J. Phys. Chem.*, 1984, **88**, 1711–1716.

[95] K. Okuyama, M. C. R. Cockett, and K. Kimura, *J. Chem. Phys.*, 1992, **97**(3), 1649–1654.

[96] T. Ishibashi and H. Hamaguchi, *J. Phys. Chem. A*, 1998, **102**(13), 2263–2269.

[97] Y. Karzazi, J. Cornil, and J. L. Brédas, *Nanotechnology*, 2003, **14**, 165–171.

[98] M. Levitus, K. Schmieder, H. Ricks, K. D. Shimizu, U. H. F. Bunz, and M. A. Garcia-Garibay, *J. Am. Chem. Soc.*, 2001, **123**(18), 4259–4265.

[99] J. Q. Lu, J. Wu, H. Chen, W. Duan, B. L. Gu, and Y. Kawazoe, *Phys. Lett. A*, 2004, **323**, 154–158.

[100] X. Zheng, N. Vedova-Brook, and K. Sohlberg, *J. Phys. Chem. A*, 2004, **108**(13), 2499–2507.

[101] Z. Chernia, T. Livneh, I. Pri-Bar, and J. E. Koresh, *Vib. Spectrosc.*, 2001, **25**, 119–131.

[102] A. Beeby, K. Findlay, P. J. Low, T. B. Marder, P. Matousek, A. W. Parker, S. R. Rutter, and M. Towrie, *Chem. Comm.*, 2003, pp. 2406–2407.

[103] ed. G. Scoles, *Atomic and molecular beam methods*, Vol. 1, Oxford University Press, New York, 1988.

[104] P. G. Lethbridge and A. J. Stace, *Rev. Sci. Instrum.*, 1987, **58**(12), 2238–22243.

[105] T. E. Gough and D. Gravel, *Rev. Sci. Instrum.*, 1981, **52**(6), 802–803.

[106] A. O'Keefe, J. J. Scherer, A. L. Cooksy, R. Sheeks, J. Heath, and R. J. Saykally, *Chem. Phys. Lett.*, 1990, **172**(3-4), 214–218.

[107] A. O'Keefe and D. A. G. Deacon, *Rev. Sci. Instrum.*, 1988, **59**(12), 2544–2551.

[108] J. M. Herbelin, J. A. McKay, M. A. Kwok, R. H. Ueunten, D. S. Urevig, D. J. Spencer, and D. J. Benard, *Appl. Opt.*, 1980, **19**(1), 144–147.

[109] J. M. Herbelin and J. A. McKay, *Appl. Opt.*, 1981, **20**(19), 3341–3344.

[110] M. A. Kwok, J. M. Herbelin, and R. H. Ueunten, *Opt. Eng.*, 1982, **21**(6), 979–982.

[111] D. Z. Anderson, J. C. Frisch, and C. S. Masser, *Appl. Opt.*, 1984, **23**(8), 1238–1245.

[112] D. Romanini, A. A. Kachanov, N. Sadeghi, and F. Stoeckel, *Chem. Phys. Lett.*, 1997, **264**(3-4), 316–322.

[113] R. Engeln, G. von Helden, G. Berden, and G. Meijer, *Chem. Phys. Lett.*, 1996, **262**(1-2), 105–109.

[114] J. J. Scherer, J. B. Paul, A. O'Keefe, and R. J. Saykally, *Chem. Rev.*, 1997, **97**(1), 25–51.

[115] J. B. Paul and R. J. Saykally, *Anal. Chem.*, 1997, **69**(9), A287–A292.

[116] G. Berden, R. Peeters, and G. Meijer, *Int. Rev. Phys. Chem.*, 2000, **19**(4), 565–607.

[117] P. Dupre, *C. R. Acad. Sci. Ser. IV*, 2001, **2**(7), 929–964.

[118] Y. B. He and B. J. Orr, *J. Chin. Chem. Soc.*, 2001, **48**(3), 591–601.

[119] M. D. Wheeler, S. M. Newman, A. J. Orr-Ewing, and M. N. R. Ashfold, *J. Chem. Soc. Faraday Trans.*, 1998, **94**(3), 337–351.

[120] H. Naus, S. J. van der Wiel, and W. Ubachs, *J. Mol. Spectrosc.*, 1998, **192**(1), 162–168.

[121] A. A. Ruth, E. K. Kim, and A. Hese, *Phys. Chem. Chem. Phys.*, 1999, **1**(22), 5121–5128.

[122] D. Romanini, A. A. Kachanov, and F. Stoeckel, *Chem. Phys. Lett.*, 1997, **270**(5-6), 538–545.

[123] D. Romanini, A. A. Kachanov, and F. Stoeckel, *Chem. Phys. Lett.*, 1997, **270**(5-6), 546–550.

[124] D. A. Kirkwood, H. Linnartz, M. Grutter, O. Dopfer, T. Motylewski, M. Pachkov, M. Tulej, M. Wyss, and J. P. Maier, *Faraday Discuss.*, 1998, **109**, 109–119.

[125] D. Romanini, P. Dupre, and R. Jost, *Vib. Spectrosc.*, 1999, **19**(1), 93–106.

[126] B. L. Fawcett, A. M. Parkes, D. E. Shallcross, and A. J. Orr-Ewing, *Phys. Chem. Chem. Phys.*, 2002, **4**(24), 5960–5965.

[127] J. E. Thompson, B. W. Smith, and J. D. Winefordner, *Anal. Chem.*, 2002, **74**, 1962–1967.

[128] M. I. Mazurenka, B. L. Fawcett, J. M. F. Elks, D. E. Shallcross, and A. J. Orr-Ewing, *Chem. Phys. Lett.*, 2003, **367**(1-2), 1–9.

[129] T. Stacewicz, S. Chudzynski, A. Czyzewski, K. Ernst, G. Karasinski, A. Pietruczuk, W. Skubiszak, and K. Stelmaszczyk, *Radiat. Phys. Chem.*, 2003, **68**(1-2), 57–63.

[130] S. Cheskis, *Prog. Energ. Combust. Sci.*, 1999, **25**(3), 233–252.

[131] X. Mercier, E. Therssen, J. F. Pauwels, and P. Desgroux, *Chem. Phys. Lett.*, 1999, **299**(1), 75–83.

[132] X. Mercier, P. Jamette, J. F. Pauwels, and P. Desgroux, *Chem. Phys. Lett.*, 1999, **305**(1), 334–342.

[133] J. Luque, J. B. Jeffries, G. P. Smith, and D. R. Crosley, *Appl. Phys. B*, 2001, **73**, 731–738.

[134] P. Zalicki, Y. Ma, R. N. Zare, E. H. Wahl, T. G. Owano, and C. H. Kruger, *Appl. Phys. Lett.*, 1995, **67**(1), 144–146.

[135] M. N. R. Ashfold, P. W. May, J. R. Petherbridge, K. N. Rosser, J. A. Smith, Y. A. Mankelevich, and N. V. Suetin, *Phys. Chem. Chem. Phys.*, 2001, **3**(17), 3471–3485.

[136] J. B. Wills, M. N. R. Ashfold, A. J. Orr-Ewing, Y. A. Mankelevich, and N. V. Suetin, *Diam. Relat. Mater.*, 2003, **12**(8), 1346–1356.

[137] W. M. M. Kessels, J. P. M. Hoefnagels, M. G. H. Boogaarts, D. C. Schram, and M. C. M. van de Sanden, *J. Appl. Phys.*, 2001, **89**(4), 2065–2073.

[138] J. P. M. Hoefnagels, A. A. E. Stevens, M. G. H. Boogaarts, W. M. M. Kessels, and M. C. M. van de Sanden, *Chem. Phys. Lett.*, 2002, **360**(1-2), 189–193.

[139] T. Yu and M. C. Lin, *J. Am. Chem. Soc.*, 1993, **115**(10), 4371–4372.

[140] D. B. Atkinson and J. L. Spillman, *J. Phys. Chem. A*, 2002, **106**(38), 8891–8902.

[141] M. D. Crisp, *Phys. Rev. A*, 1970, **1**(1), 1604–1611.

[142] P. Zalicki and R. N. Zare, *J. Chem. Phys.*, 1995, **102**(7), 2708–2717.

[143] K. K. Lehmann and D. Romanini, *J. Chem. Phys.*, 1996, **105**(23), 10263–10277.

[144] J. T. Hodges, J. P. Looney, and R. D. vanZee, *J. Chem. Phys.*, 1996, **105**(23), 10278–10288.

[145] J. Martin, B. A. Paldus, P. Zalicki, E. H. Wahl, T. G. Owano, J. S. Harris, C. H. Kruger, and R. N. Zare, *Chem. Phys. Lett.*, 1996, **258**(1-2), 63–70.

[146] D. H. Lee, Y. Yoon, B. Kim, J. Y. Lee, Y. S. Yoo, and J. W. Hahn, *Appl. Phys. B*, 2002, **74**(4-5), 435–440.

[147] J. J. Scherer, D. Voelkel, D. J. Rakestraw, J. B. Paul, C. P. Collier, R. J. Saykally, and A. O'Keefe, *Chem. Phys. Lett.*, 1995, **245**(2-3), 273–280.

[148] H. Kogelnik and W. W. Rigrod, *Proc. IRE*, 1962, **50**(2), 220–22.

[149] G. Brooker, *Modern Classical Optics*, Oxford University Press, Oxford, first ed., 2003.

[150] A. Yariv, *Optical Electronics in Modern Communications*, Oxford University Press, Oxford, fifth ed., 1997.

[151] A. J. Orr-Ewing and C. J. Rennick, CRDS labview program Priv. Comm.

[152] N. Elliott, *Cavity ring-down spectroscopy of cold molecules* Master's thesis, Department of Chemistry, University of Durham, 2003.

[153] C. M. Western, WI2 Priv. Comm.

[154] F. Martin, R. Bacis, S. Churassy, and J. Vergs, *J. Mol. Spectrosc.*, 1986, **116**(1), 71–100.

[155] M. Levitus, K. Schmieder, H. Ricks, K. D. Shimizu, U. H. F. Bunz, and M. A. Garcia-Garibay, *J. Am. Chem. Soc.*, 2002, **124**(28), 8181–8181.

[156] J. Simons and L. Snoek, Sample oven design. Priv. Comm.

[157] M. Hillenkamp, S. Keinan, and U. Even, *J. Chem. Phys.*, 2003, **118**(19), 8699–8705.

[158] J. D. Lewis, T. B. Malloy, T. H. Chao, and J. Laane, *J. Mol. Struct.*, 1971, **12**(3), 427–449.

[159] M. J. Frisch, G. W. Trucks, H. B. Schlegel, G. E. Scuseria, M. A. Robb, J. R. Cheeseman, V. G. Zakrzewski, J. A. Montgomery, Jr., R. E. Stratmann, J. C. Burant, S. Dapprich, J. M. Millam, A. D. Daniels, K. N. Kudin, M. C. Strain, O. Farkas, J. Tomasi, V. Barone, M. Cossi, R. Cammi, B. Mennucci,

C. Pomelli, C. Adamo, S. Clifford, J. Ochterski, G. A. Petersson, P. Y. Ayala, Q. Cui, K. Morokuma, D. K. Malick, A. D. Rabuck, K. Raghavachari, J. B. Foresman, J. Cioslowski, J. V. Ortiz, A. G. Baboul, B. B. Stefanov, G. Liu, A. Liashenko, P. Piskorz, I. Komaromi, R. Gomperts, R. L. Martin, D. J. Fox, T. Keith, M. A. Al-Laham, C. Y. Peng, A. Nanayakkara, M. Challacombe, P. M. W. Gill, B. Johnson, W. Chen, M. W. Wong, J. L. Andres, C. Gonzalez, M. Head-Gordon, E. S. Replogle, J. A. Pople, and Gaussian, Inc., Pittsburgh PA, Gaussian 98, revision a.9, 1998.

[160] A. D. Becke, *J. Chem. Phys.*, 1993, **98**, 5648–5652.

[161] C. Lee, W. Yang, and R. G. Parr, *Phys. Rev. B*, 1988, **37**, 785–786.

[162] J. B. Foresman, M. H.-G. amd J. A. Pople, and M. J. Frisch, *J. Phys. Chem.*, 1992, **96**, 135–149.

[163] H. B. Schegel, *J. Comp. Chem.*, 1982, **3**, 214–218.

[164] H. B. Schlegel, *New Theoretical Concepts for Understanding Organic Reactions*, Kluwer Academic, The Netherlands, 1989.

[165] H. B. Schlegel, *Modern Electronic Structure Theory*, World Scientific Publishing, Singapore, 1995.

[166] O. F. Koentjoro *Synthetic and computational studies of conjugated acetylenic systems* PhD thesis, Department of Chemistry, University of Durham, 2003.

[167] L. Zhao, I. F. Perepichka, F. Türksoy, A. S. Batsanov, A. Beeby, K. Findlay, and M. R. Bryce, *New. J. Chem.*, 2004, **28**, 912–918.

[168] R. E. Stratmann, G. E. Scuseria, and M. J. Frisch, *J. Chem. Phys.*, 1998, **109**, 8218–8224.

[169] R. Bauernschmitt and R. Ahlrichs, *Chem. Phys. Lett.*, 1996, **256**, 454–460.

[170] M. E. Casida, C. Jamorski, K. C. Casida, and D. R. Salahub, *J. Chem. Phys.*, 1998, **108**, 4439–4449.

[171] J. C. Sancho-Garcia and J. Cornil, *J. Chem. Phys.*, 2004, **121**, 3096–3101.

[172] J. J. L. Spaanjaars, J. J. ter Meulen, and G. Meijer, *J. Chem. Phys.*, 1997, **107**(7), 2242–2248.

[173] A. Beeby and S. R. Rutter, 1, 4-bis(2,4,6-tri*tert*butylphenylethynyl)-2,3,5,6-tetramethylbenzene, synthesis structure and spectra. Unpublished results.

[174] R. N. Porter, *Ann. Rev. Phys. Chem.*, 1974, **25**, 317.

[175] Melles Griot product catalogue, 1999.